instituto IMdea nanociencia

SPIN ORBI TRONICS

EXCELENCIA SEVERO OCHOA

Spin Orbit driven effects and Thermal Activation of Ferromagnet Intercalated Graphene-Heavy Metal Interfaces

Adrián Gudín*[1,2], José Manuel Diez[1,2], Pablo Olleros-Rodríguez[1], Alberto Anadón[1], Fernando Ajejas[1,2], Leticia de Melo Costa[1,2], Rubén Guerrero[1], Julio Camarero[1,2], Rodolfo Miranda[1,2] and Paolo Perna[1]

[1]IMDEA-Nanoscience, Campus de Cantoblanco, 28049 Madrid, Spain

[2]Dpto. Física de la Materia Condensada, IFIMAC, and Instituto "Nicolás Cabrera", Universidad Autónoma de Madrid, 28049 Madrid, Spain

E-mail: adrian.gudin@imdea.org

Introduction

Graphene (Gr) has a negligible intrinsic Spin- Orbit Coupling (SOC) in its pristine state. However, by intercalating adequate metal (such as Co underneath Gr/HM(111) (Pt or Ir)). it is possible to transfer to graphene a giant SOC. The incorporation of active properties to Gr can enable its use in spintronics technology, exploiting further more the long spin diffusion and lifetime.

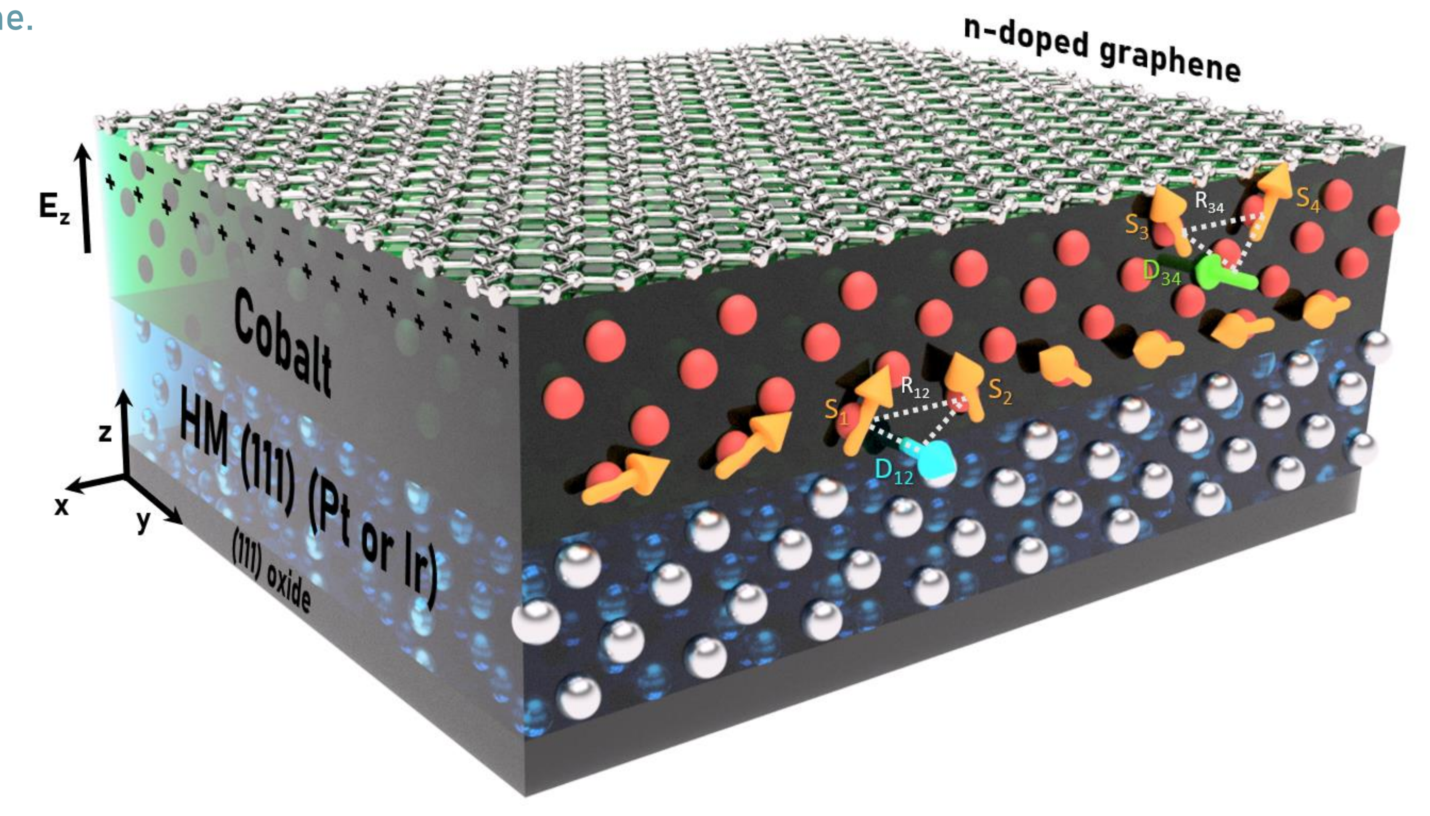

Interplay between SOC-induced DMI at the Co/HM(111) and opposite Rashba-type DMI at the Gr/Co interfaces.

Enhancement of PMA

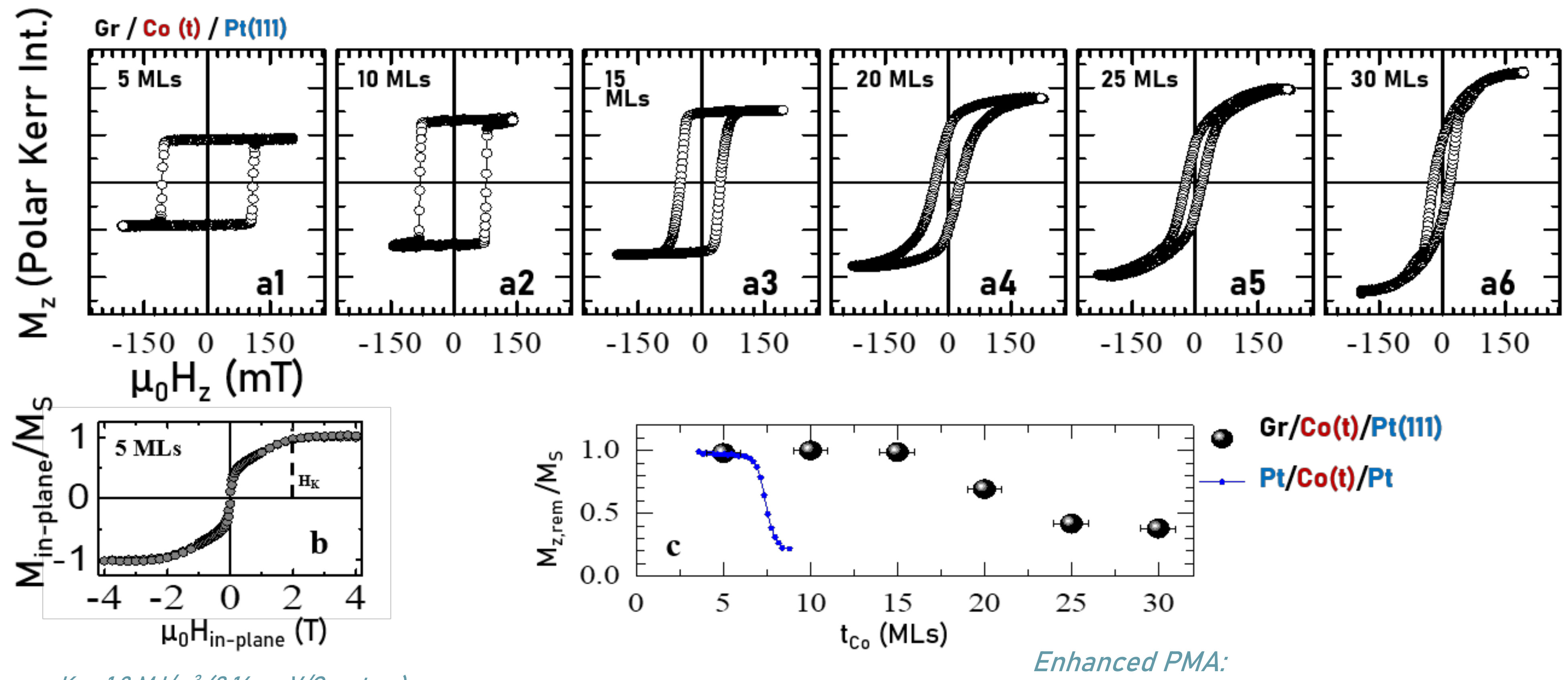

- K_0 = 1.3 MJ/m³ (0.16 meV/Co-atom)
- M_S = 1.3 MA/m; H_K = 2 T

- On Pt(111) single crystal spin-reorientation at 12MLs
- On Ir(111) single crystal spin-reorientation at 13MLs

Enhanced PMA:

- Extended up to 20MLs Co (non-epitaxial samples spin-reorientation at 7 MLs)
- On oxide substrates (avoid leakage current in devices)

XAS-XMCD @ Co-$L_{2,3}$

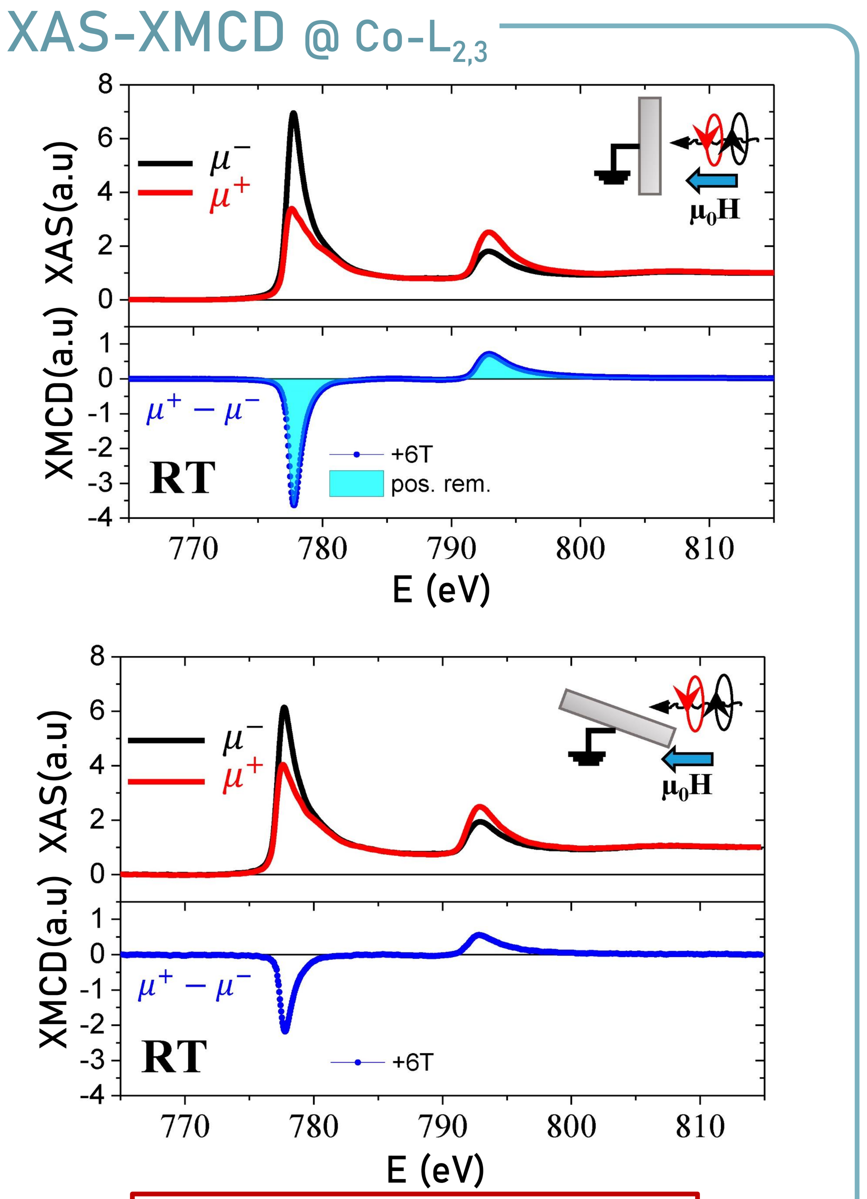

$m^{\perp}_L/m^{\perp}_S$ = 0.15 >> $m^{\parallel}_L/m^{\parallel}_S$ = 0.11

hcp Co bulk m^{bulk}_L/m^{bulk}_S = 0.10

SO anisotropy: $\Delta m_L/n_h = (m^{\parallel}_L - m^{\perp}_L)/n_h$

If n_h = 2.49 → $\Delta m_L/n_h$ = 0.11 μ_B/atom (~0.16 meV/Co-atom)

The orbital moment is strongly confined in the sample normal direction

Mechanisms for FM intercalation in Gr

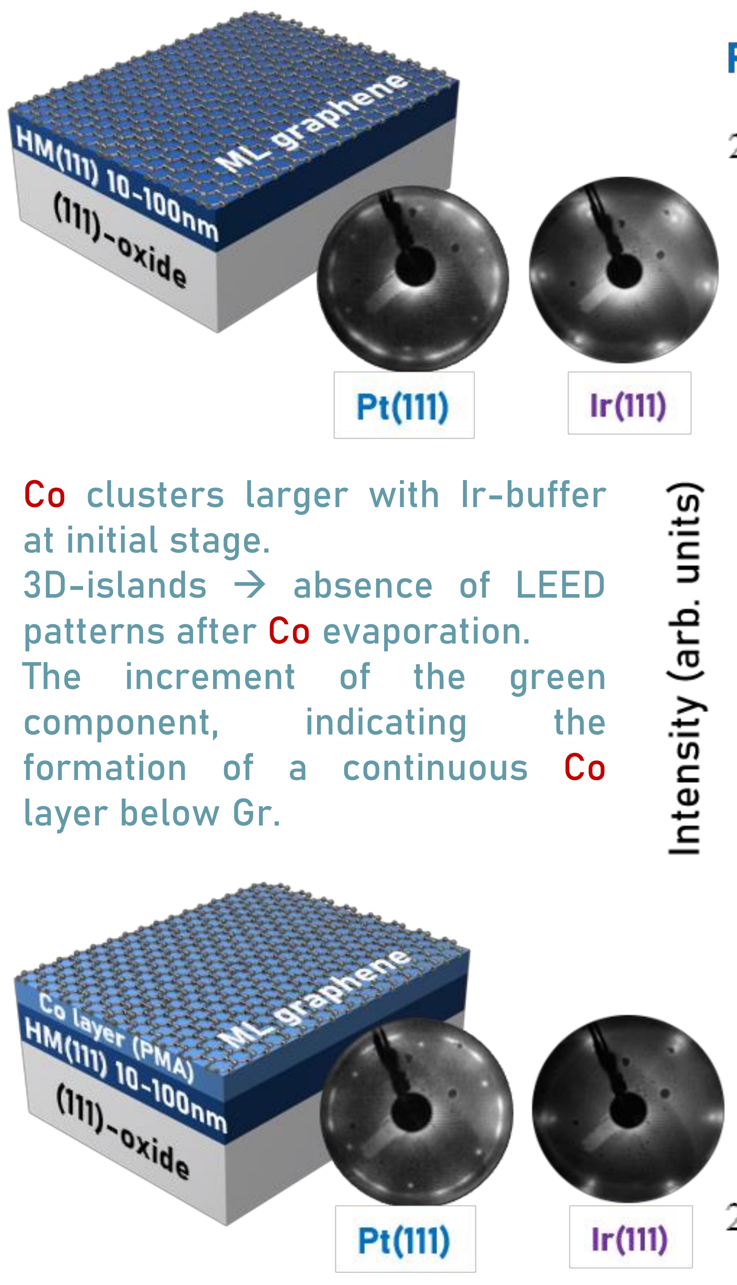

- Co clusters larger with Ir-buffer at initial stage.
- 3D-islands → absence of LEED patterns after Co evaporation.
- The increment of the green component, indicating the formation of a continuous Co layer below Gr.

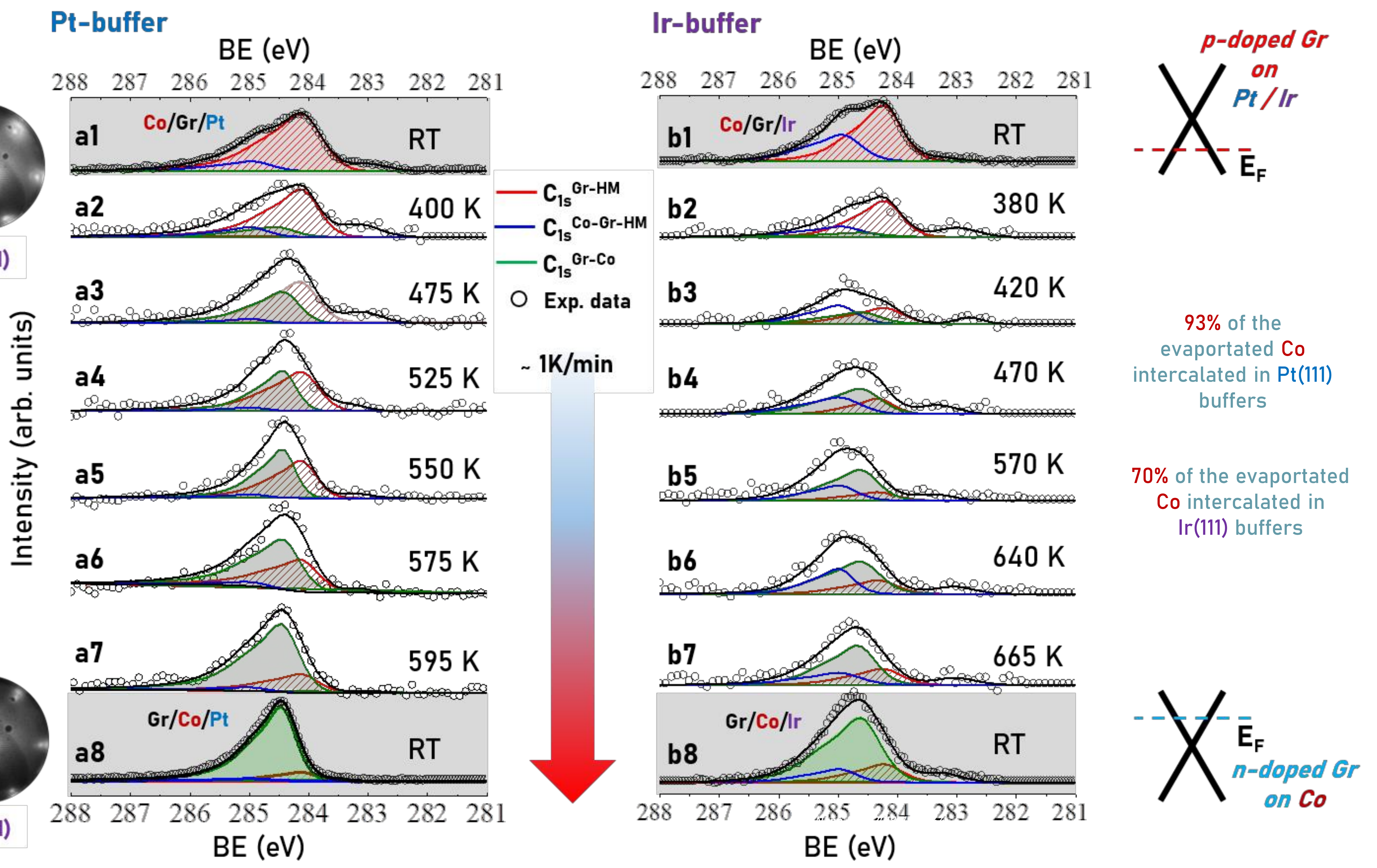

93% of the evaporated Co intercalated in Pt(111) buffers

70% of the evaportated Co intercalated in Ir(111) buffers

Thermal activated FM intercalation in Gr

$$A = \frac{A^{comp}_{C_{1s}}}{A^{conv}_{C_{1s}}} \qquad A(T) \propto e^{-\frac{E_a}{K_B T}} \qquad E_a = \frac{1}{K_B T}$$

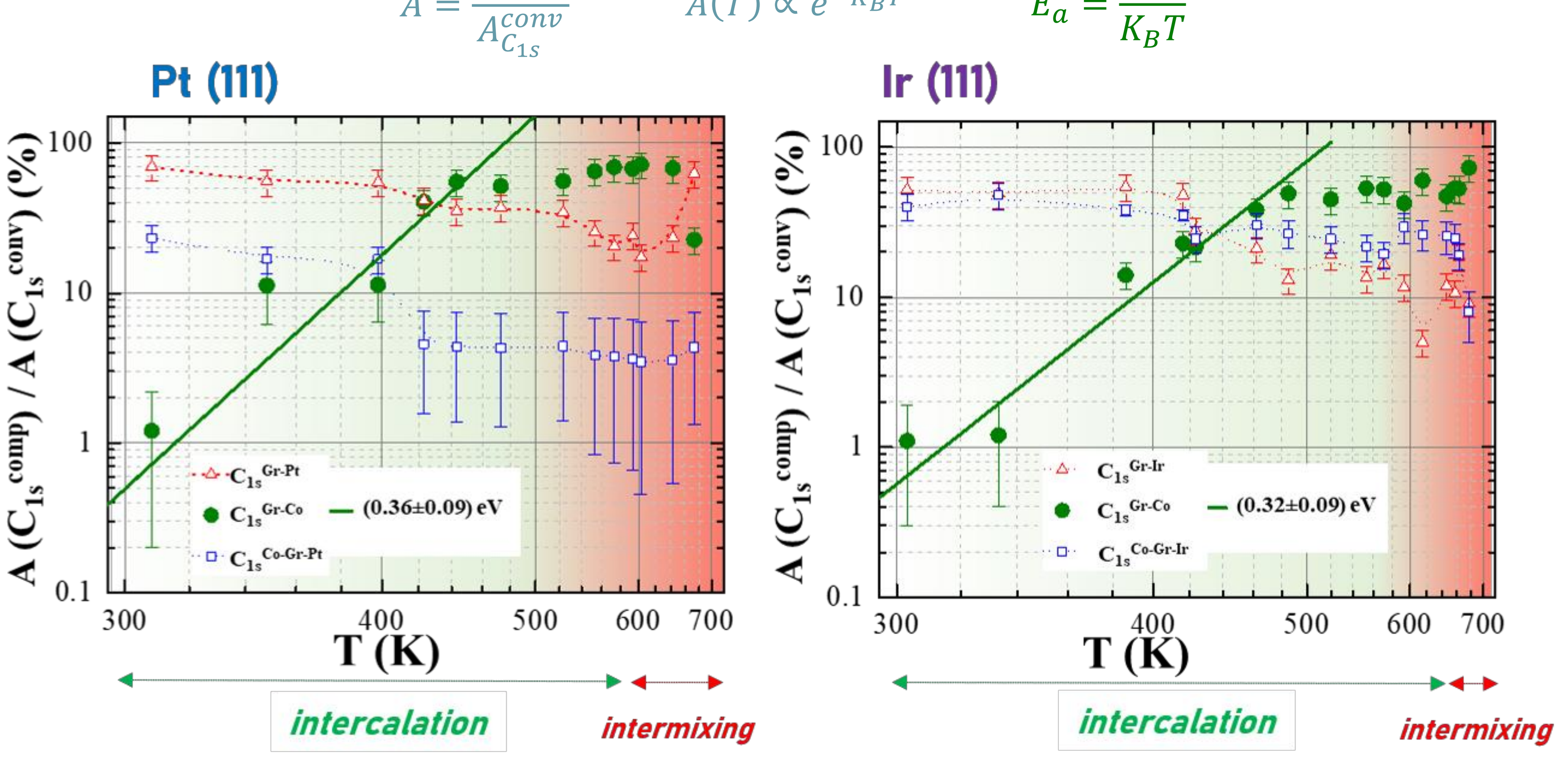

- Intercalation requires a slightly higher temperature for Gr/Ir.
- Less efficient intercalation mechanism through Gr/Ir surface than Gr/Pt.

Polar Kerr Microscopy

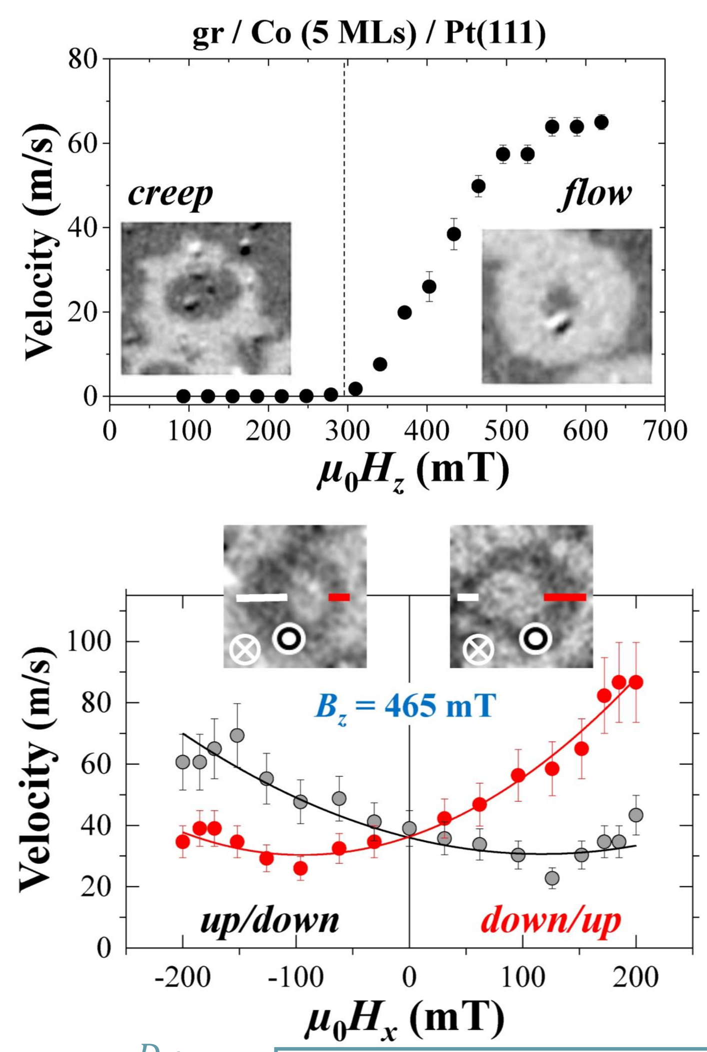

$\mu_0 H_{DMI} = D/M_S\Delta$

$D^{Co/Pt}$ = 1.4 ± 0.2 mJ / m²

$D^{gr/Co}$ = -0.8 ± 0.2 mJ / m²

$\Delta = \sqrt{A/K_0}$

A = 24pJ/m

D_{eff} = 0.6 ± 0.2 mJ / m²

Sign of H_{DMI}: left-handed DW chirality

STEM-EELS analysis

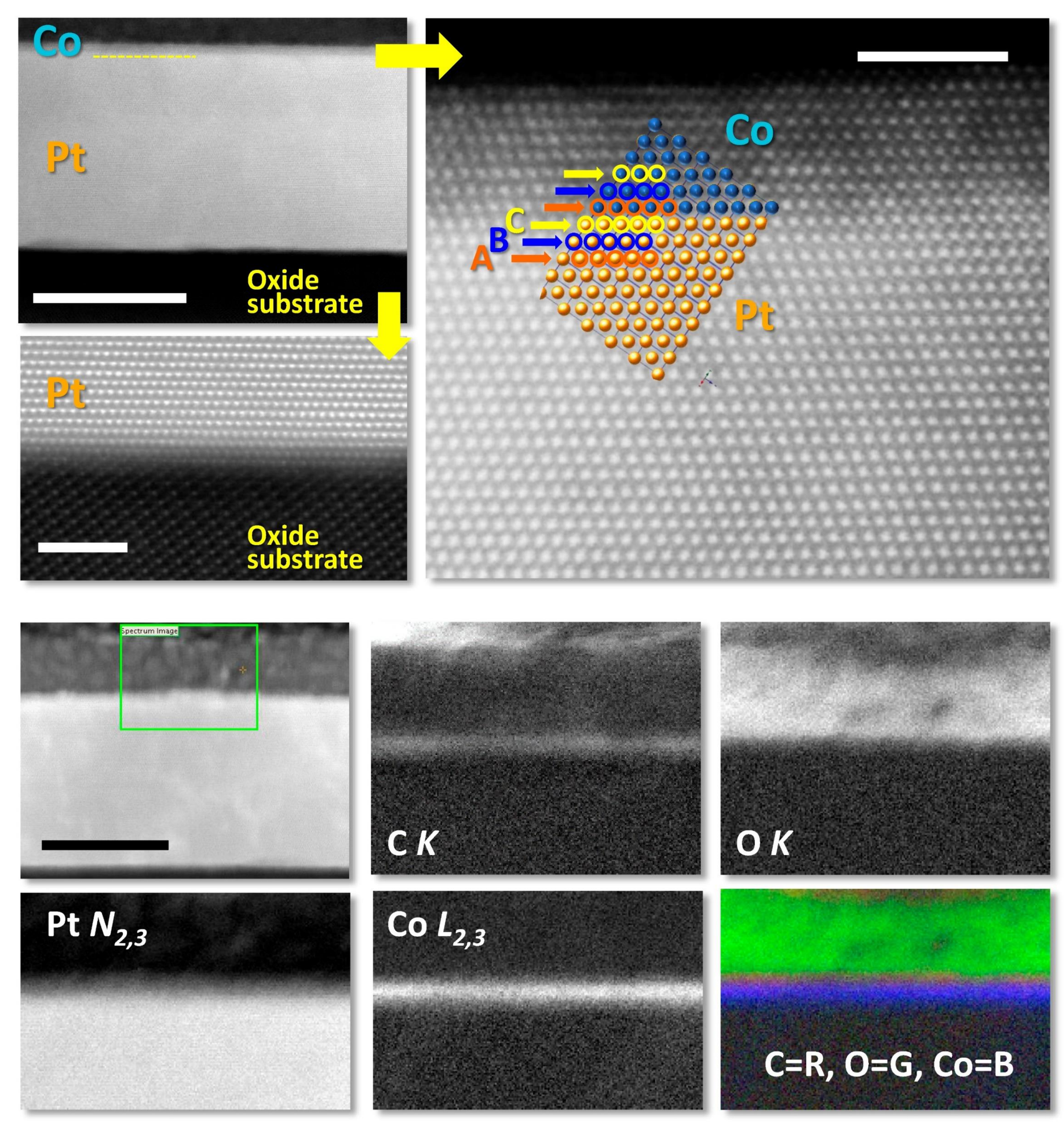

Gr provides: *i)* surfactant action for the Co growth, producing an intercalated, flat, highly perfect *fcc* film, pseudomorphic with Pt; *ii)* an efficient protection from oxidation.

Conclusions

- High quality Gr-based epitaxial stacks on oxides (resembling single crystals)
- Enhanced PMA, extended up to 20MLs of Co
- *FCC* structure of Co, pseudomorphic with Pt
- Rashba-DMI@Gr/Co OPPOSITE to SOC-DMI@Co/Pt
- Existence of chiral left-handed Néel-type domain walls stable at RT and protected by Gr

Nano Lett. 2018, 18, 5364

ACS Appl. Mater. Interfaces 2020, 12, 3, 4088-4096

IFIMAC · UNIVERSIDAD AUTONOMA DE MADRID · excelencia UAM CSIC · GOBIERNO DE ESPAÑA · MINISTERIO DE ECONOMÍA Y COMPETITIVIDAD · La Suma de Todos Comunidad de Madrid · UNIÓN EUROPEA FONDOS ESTRUCTURALES · GRAPHENE FLAGSHIP · FLAG-ERA

PCI2019-111867-2

RTI2018-097895-B-C43 (FUN-SOC)

NANOFRONTMAG-CM,

NANOMAGCOST-CM

EVALUATING THE HEATING EFFICIENCY OF IRON OXIDE NANOPARTICLES FOR PHOTOTHERMAL THERAPIES

DANIEL ARRANZ[1,3*], IRENE MORALES[1], ROSA WEIGAND[2], PATRICIA DE LA PRESA[1,3]

[1] Instituto de Magnetismo Aplicado (UCM-ADIF-CSIC), Madrid, Spain.
[2] Dpt. de Óptica, [3] Dpt. de Física de Materiales, Facultad de Ciencias Físicas, Universidad Complutense de Madrid, Avda. Complutense s/n, 28040 Madrid, Spain.

daniarra@ucm.es

UNIVERSIDAD COMPLUTENSE MADRID

INSTITUTO DE MAGNETISMO APLICADO
LABORATORIO SALVADOR VELAYOS UCM ADIF

Introduction

Hyperthermia is a promising emergent therapy against cancer. The aim of this work is to learn about the heating mechanism of iron oxide nanoparticles (NPs) under a near infrared laser irradiation. Maghemite (γ-Fe_2O_3) and hematite (α-Fe_2O_3) have the same oxidation state, similar band gaps and different magnetic properties. Both nanoparticles have been used to investigate if the magnetization plays any role on the heating mechanism.

What? To study the heating of iron oxide nanoparticles

From (Fe_2O_3) Hematite and Maghemite, different phases of Fe_2O_3

How? Irradiating the NPs with a near infrared laser

Synthesis and Characterization

Synthesis of γ-Fe_2O_3 NPs

Massart modified method (Co-precipitation)

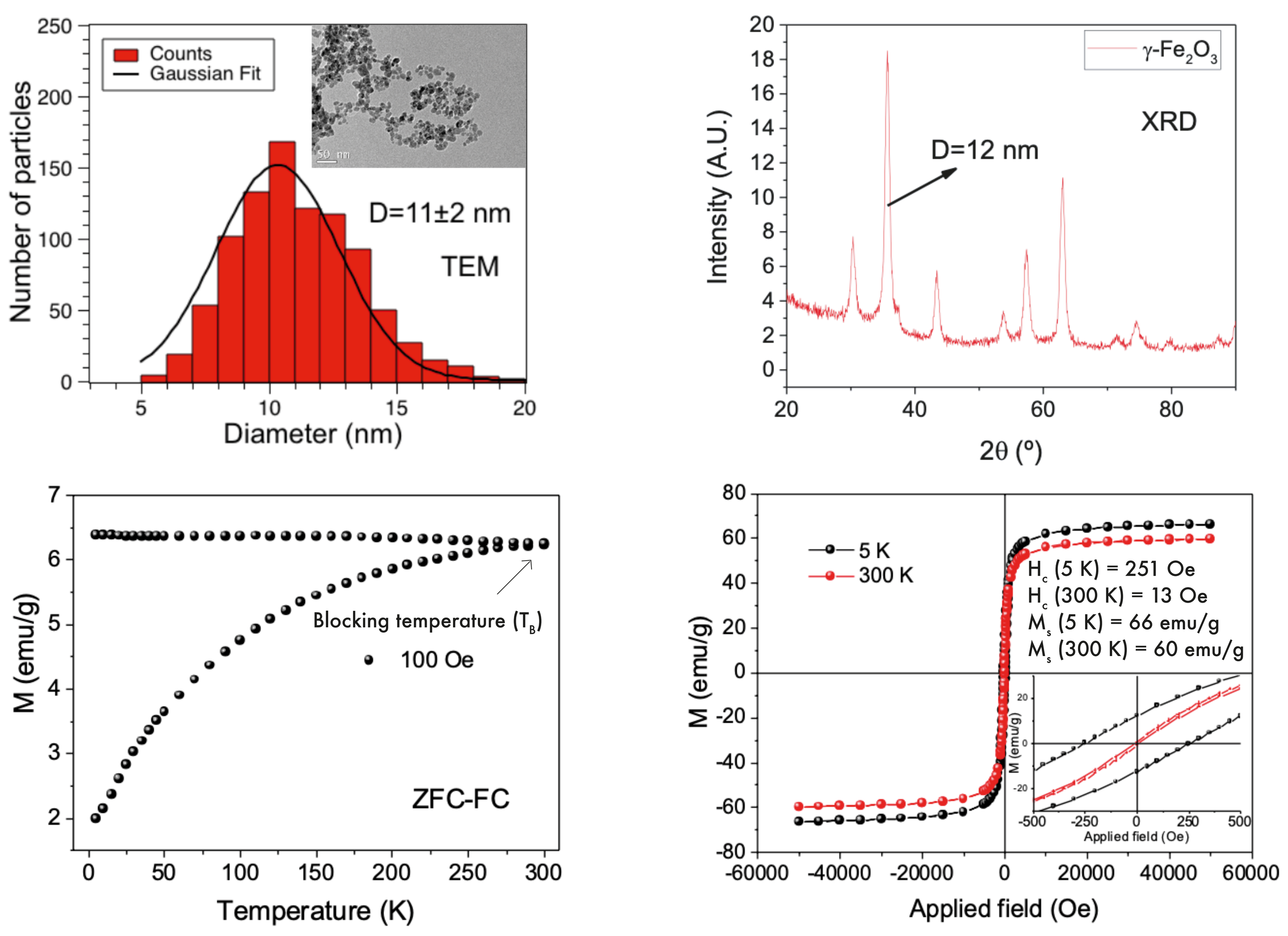

Dextran Coating
- ↑ Coloidal stability
- ↑ Biocompatibility
- ↓ Toxicity

Crystallite size measured with Scherrer equation: $D = K\lambda/\beta\cos\theta$

Synthesis of α-Fe_2O_3 NPs

Sol - Gel process

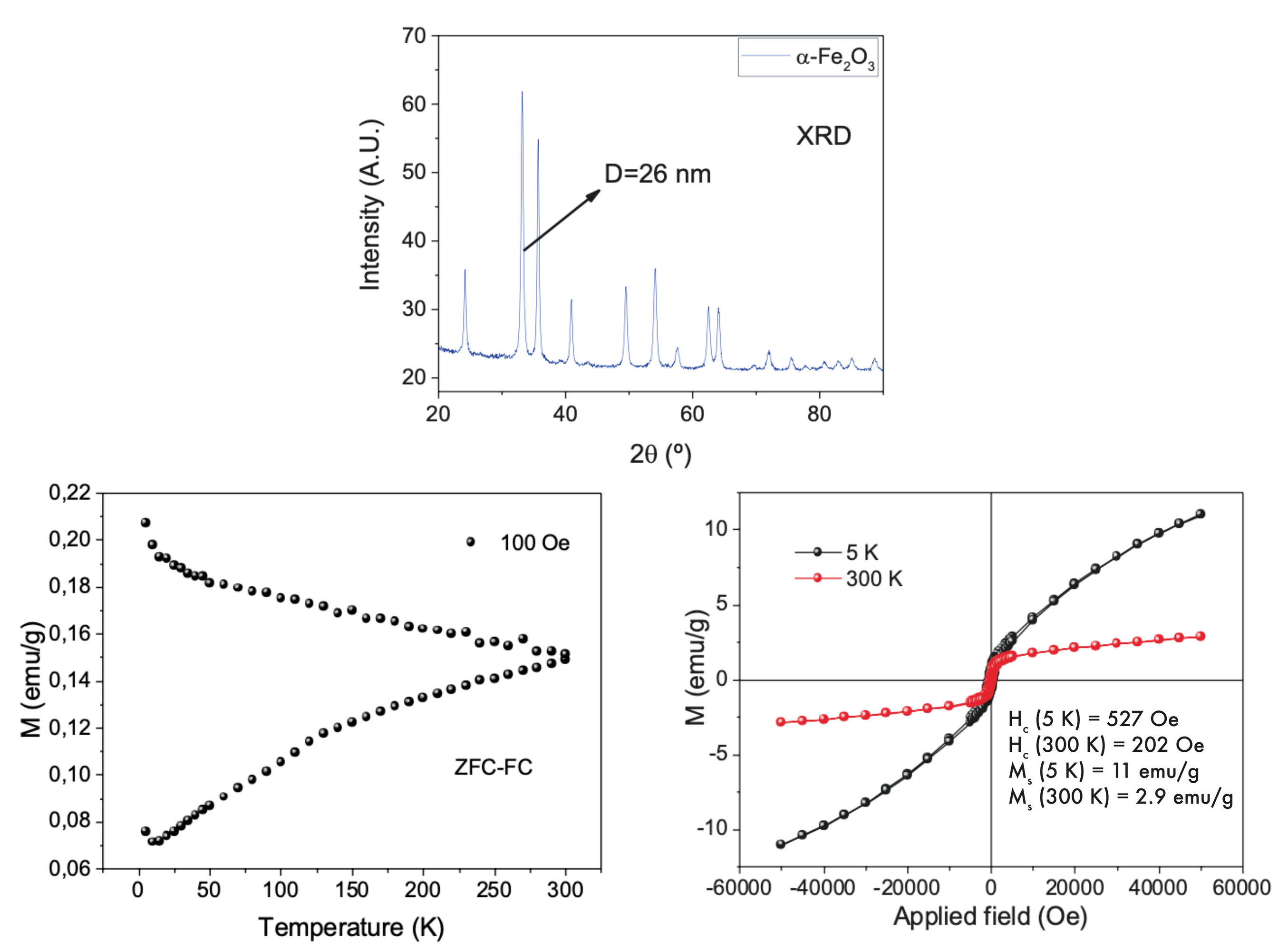

Photothermal Results

20 µL of NPs are introduced in a thin capilar. The NPs are irradiated during 120 s with a Titanium:Saphire laser operating at λ=773 nm in continuous wave with 50 mW average power. The heating and the cooling curve (laser off), are registered with an infrared camera. The SAR (Specific Absorption Rate) value is calculated using the first instants of heating where the relation ΔT/Δt is linear (adiabatic aproximation).

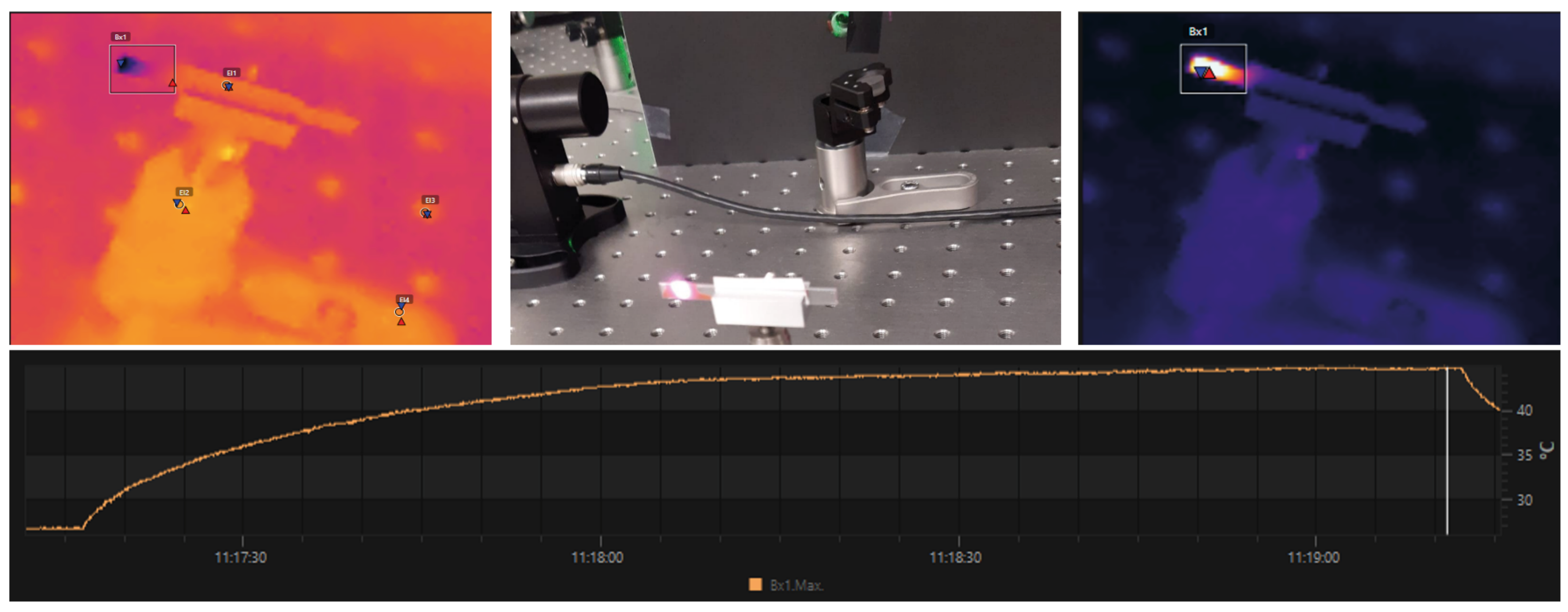

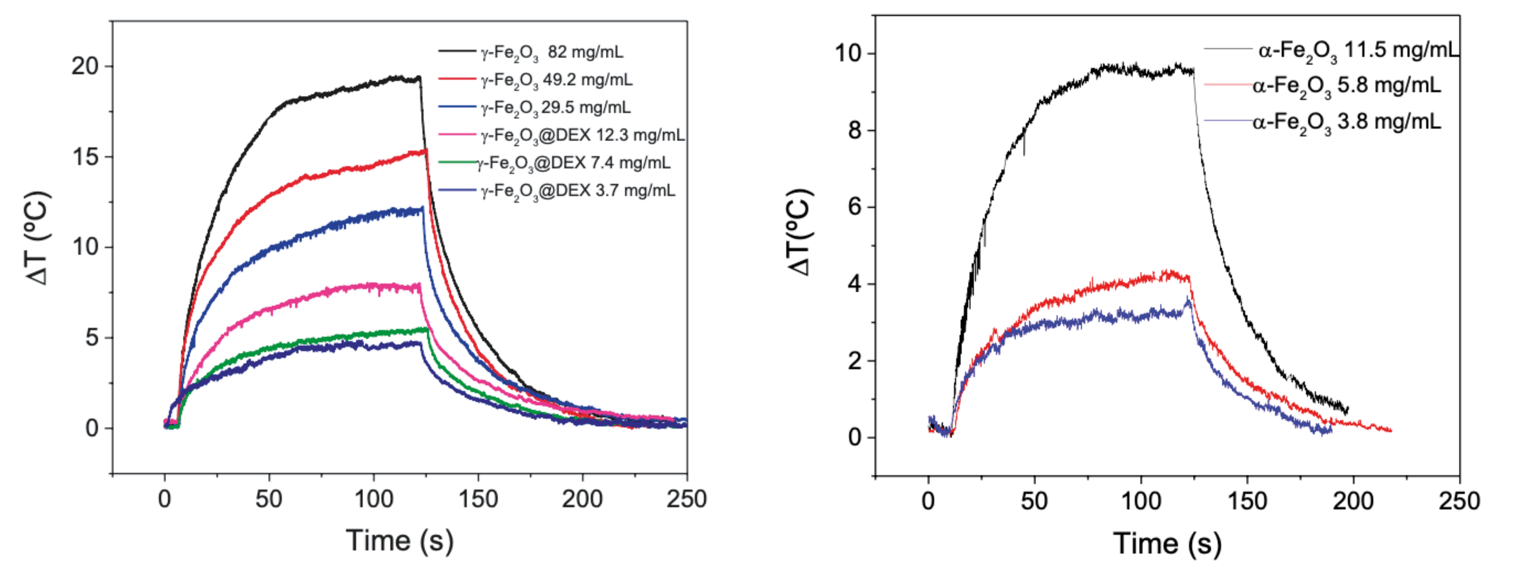

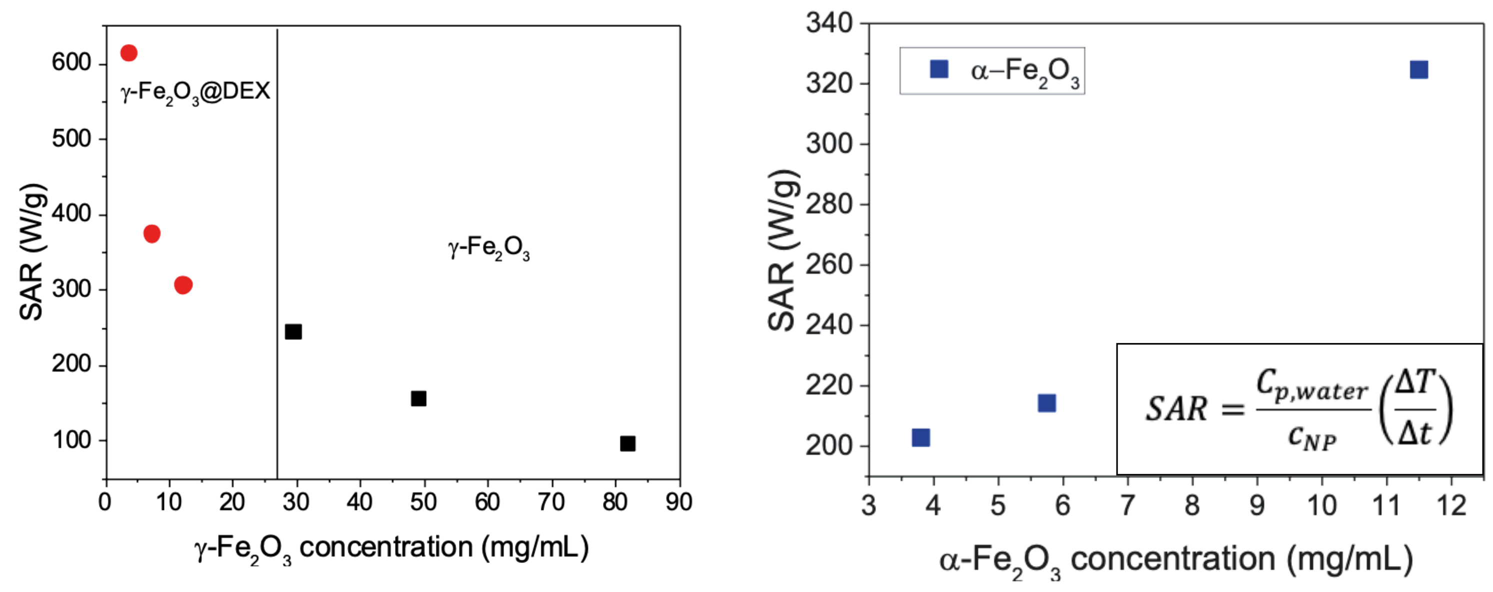

Sample	Transmittance	Concentration (mg/mL)	SAR (W/g)	ΔT_{max} (°C)	D (nm)
γ-Fe_2O_3	0.11	82	95	18.46	11
	0.44	49.2	156	14.09	
	0.69	29.5	244	11.69	
γ-Fe_2O_3@DEX	0.41	12.3	305	7.76	11
	0.57	7.4	373	5.21	
	0.65	3.7	613	4.49	
α-Fe_2O_3@DEX	0.17	11.5	324	9.79	26
	0.42	5.8	214	4.39	
	0.55	3.8	202	3.70	

SUMMARY
- Both types of NPs (with ΔE_{gap}~2 eV) release heat when irradiated with an IR laser (1.6 eV).
- The are no significant changes in the ΔT with similar concentrations in both phases.
- The SAR vs concentration increases or decreases depending on the magnetic phase.
- The dextran coating seems not to play a major roll on the heating process.
- For further investigation, measurements at similar particle sizes and a study of the heating release of other oxidation states such as magnetite (Fe_3O_4) should be done.

YRinM 2020

Improved Averaging of Hysteresis Loops from Micromagnetic Simulations of Non-Interacting Uniaxial Nanoparticles

Rafael Delgado-Garcia[1], Gabriel Rodriguez-Rodriguez[1], Jose M. Colino[1]
[1] INAMOL - UCLM, Av. Carlos III, s/n, 45071 Toledo (Toledo) Spain,
e-mail: gabriel.rrodriguez@uclm.es

Macroscopic ensembles of non-interacting single-domain Magnetic Nanoparticles (MNPs) have been modelled with micromagnetic simulations. At first, hysteresis loops of randomly-oriented nanoparticles have been averaged, with the withdrawal of high computational cost and slow convergency. To reduce computational cost in such systems we have developed an optimized method of hysteresis loop averaging based on the high rotational symmetry found in uniaxial anisotropic systems.

This improved method reduces the number of simulations required to generate macroscopic-like ensembles of randomly oriented and non-interacting magnetic nanoparticles (i.e. a dilute powder), obtaining a fast convergency to predicted Stoner-Wohlfarth behaviour of single-domain uniaxial particles and matching magnetic properties such as coercivity, remanence and energetic product with a low count of simulations.

Motivation: Distributing directions on the sphere

Figure 1 **(a)** shows how uniformly distributed directions on the θ-φ plane are not uniformly distributed on the sphere, with higher density towards the poles. An option to get true spherical symmetry can be restricting randomly generated 3D coordinates to a sphere [Figure 1 **(b)**], which representation on the θ-φ plane shows less dense regions at $\theta\sim 0$ and $\theta\sim\pi$.

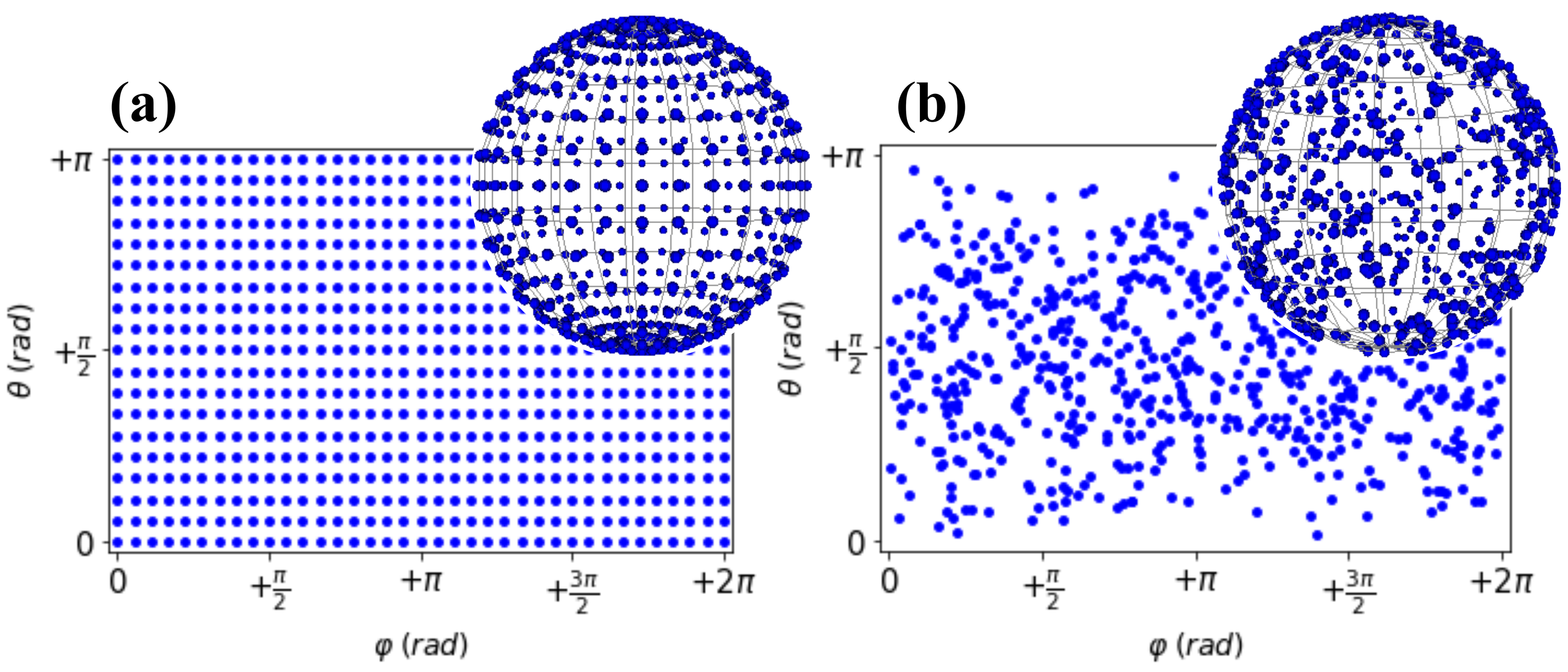

Figure 1. Angular and spheroidal plots of 703 directions distributed uniformly in **(a)** the θ-φ plane and **(b)** over a spheric surface.

Random distributions of non-interacting MNPs

Hysteresis loops of quasi-spheroidal 8nm randomly-oriented MNPs have been averaged uniformly over the sphere from micromagnetic simulations. Different anisotropic materials have been simulated with good agreement with theoretical and experimental data [Figure 2].

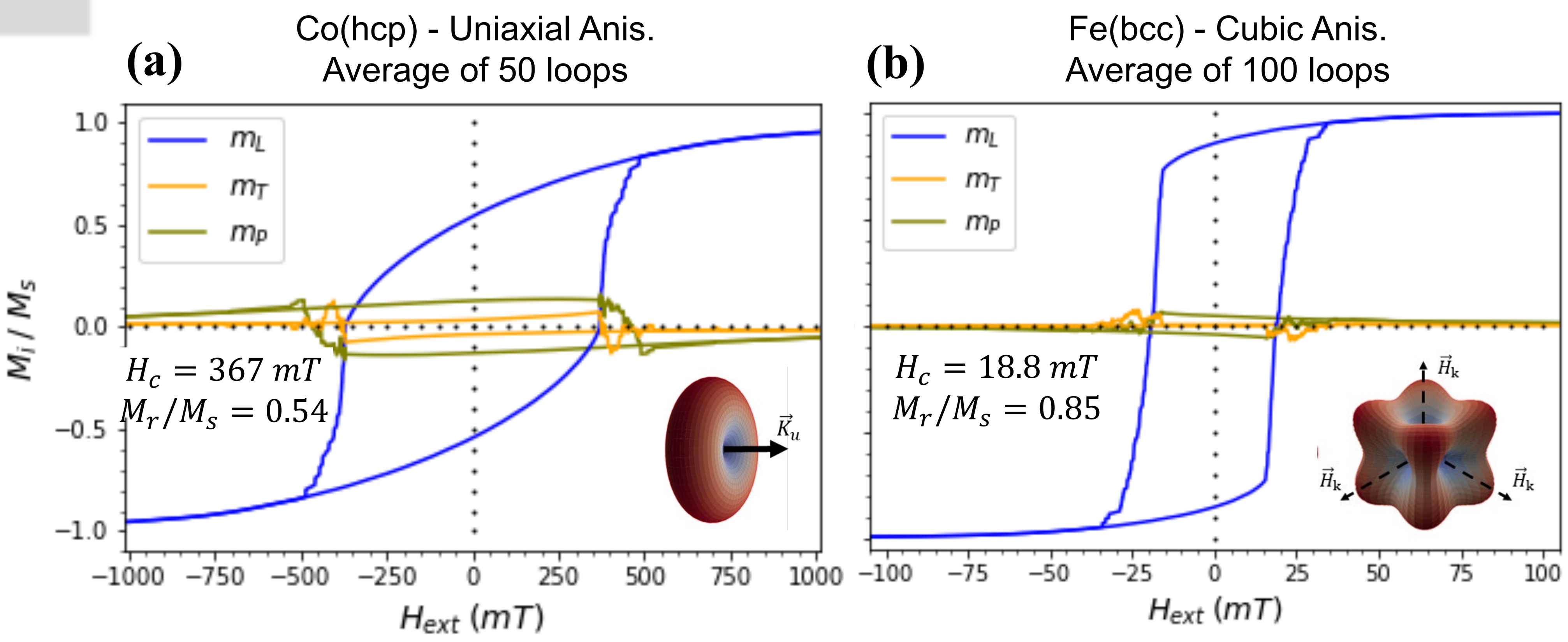

Figure 2. Hysteresis loops of **(a)** Co(hcp) and **(b)** Fe(bcc) non-interacting randomly-oriented MNPs. Results of Co(hcp) uniaxial MNPs follow Stoner-Wohlfarth behavior, while Fe(bcc) cubic MNPs' hysteresis loops agree with experimental data (Farrel et. al., 2005).

Polar averaging of hysteresis loops in highly rotational symmetry systems

Hysteresis loops have been simulated in the XY plane every 5 degrees from the easy (100) to the hard (010) in plane magnetization axes. Due to symmetric anisotropy in spheroidal uniaxial systems, it is possible to propose simplified $\vec{M}$ averaging methods based on in-plane single hysteresis loops, mimicking the randomly oriented ensemble of macroscopic quantities of nanoparticles, such in powder-like systems, using two methods:

(A): Arithmetic averaging [Figure 3 **(a)**], which hardly follows predicted Stoner-Wohlfarth behaviour, overestimating coercivity, remanence and thus magnetic energy of the non-interacting ensemble. This is due to the higher density of loops in the region of $\theta\sim 0$ for an uniform θ-φ distribution [Figure 1 **(a)**]–, where easy axis lies and thus remanence and coercivity achieve its maximum values ($M_r\sim M_s$ and $H_c\sim H_k$).

(S): Improved spheroidal averaging [Figure 3 **(b)**], that reproduces much more efficiently S-W, smoothing step-like events in averaged magnetization curve with a fast convergence of magnetic parameters [Figure 3 **(c), (d)**]. This improved method matches M_r (error < 1%) using only 7 ($\Delta\varphi$=15°) hysteresis loops, H_c (error < 0.1%) with 4 ($\Delta\varphi$=30°) loops, and magnetic energy (error < 2%) with 19 ($\Delta\varphi$=5°) loops.

$$M(H)_{system} = \sum_{N} \frac{M(H)_{single\ NP}}{N} \qquad \text{(A)}$$

$$M(H)_{system} = \sum_{\theta=0}^{\pi/2} 2\pi \left[\cos\left(\theta - \frac{\Delta\theta}{2}\right) - \cos\left(\theta + \frac{\Delta\theta}{2}\right)\right] M(H)_{single\ NP} \qquad \text{(S)}$$

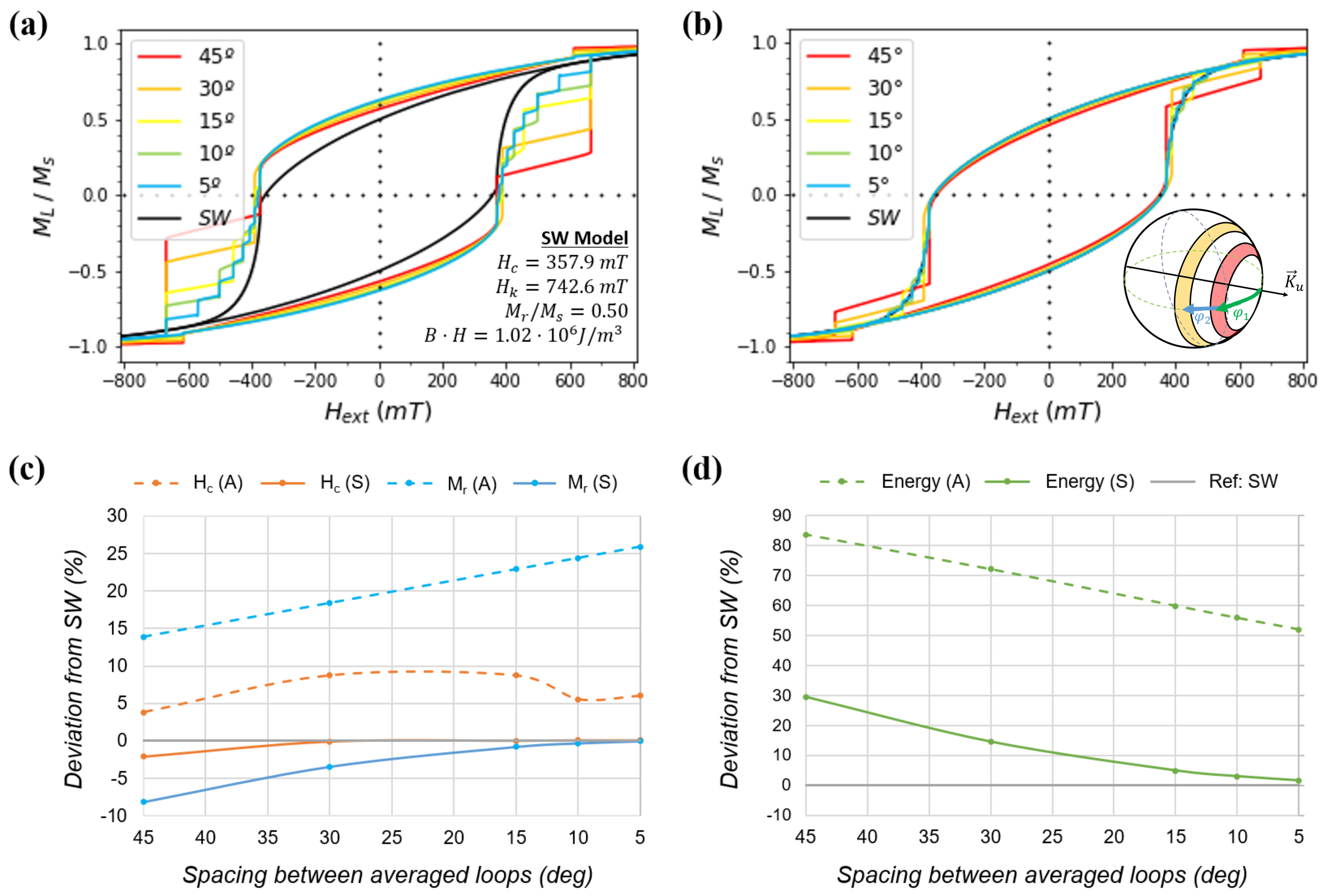

Figure 3. Low count hysteresis loops for rotational symmetry systems (uniaxial-like) obtained with: **(a)** Arithmetic (A) and **(b)** Spherical (S) averaging methods using 19, 10, 7, 4 and 3 hysteresis loops spaced every 5, 10, 15, 30 and 45 degrees, respectively. Schematic of Spheroidal averaging is shown as insert in graph **(b)**. Notice the step-like behaviour in more spaced averages.
Panels **(c)** and **(d)** show the relative differences between remanence M_r, coercivity H_c and magnetic energy of averaged loops in absolute deviation respect to SW model.

Conclusions

An improved averaging method for hysteresis loops of MNPs has been developed, drastically reducing the number of micromagnetic calculations of hysteresis loops needed to get macroscopic behaviour of uniaxial-like non-interacting ensembles.
This method has been tested against the Stoner-Wohlfarth model obtaining excellent results in terms of optimization of computational costs reproducing not only H_c and M_r values with just a few angular hysteresis loops, but the shape of the entire cycle.

Finally, the exact energy involved during the magnetization reversal process has been extracted with excel agreement of improved Spheroidal method in comparison with Arithmetic method (error < 2% vs > 50%, respectively) using only 19 ($\Delta\varphi$=5°) hysteresis loops.

Acknowledgements

This work has been possible thanks to the MICINN, as a part of the Project MAT2015-65295-R: "Nanocomposites magnéticos para aplicaciones en energía y sensores". Rafael Delgado-Garcia thanks UCLM and Banco Santander for the scholarship for research initiation during his Master studies.

GOBIERNO DE ESPAÑA
MINISTERIO DE ECONOMÍA Y COMPETITIVIDAD
Santander

References

E. H. Sánchez et al., Chemistry of Materials, Vol. 32, p.969-981 (2020)
D. Kim et al., Journal of Magnetism and Magnetic Materials, Vol. 320(19), p.2390-2396 (2008)
Q. Li et al., Scientific Reports, Vol. 7, p.9894 (2017)
D. Peddis et al., Chemistry of Materials, Vol. 25(10), p.2005-2013 (2013)
A. Vansteenkiste et al., AIP Advances, Vol. 4, p.107133 (2014)
J. A. Osborn, Physical Reviews, Vol. 67, p.351 (1945)
D. Farrell et al., Journal of Physical Chemistry B, Vol. 109(28), p.13409-13419 (2005)
C. Tannous and J. Gleraltowski, European Journal of Physics, Vol. 29, p.475-487 (2008)

instituto imdea nanociencia

Rare earth-free MnAlC permanent magnets produced by hot-pressing from ε-phase gas-atomized and milled powder

C. Muñoz-Rodríguez[1], E.M. Palmero[1], J. Rial[1], L. Feng[2], T. Mix[2], T.G. Woodcock[2], A. Bollero[1]

[1] Group of Permanent Magnets and Applications, IMDEA Nanoscience, Madrid, Spain
[2] Leibniz IFW Dresden, Institute of Metallic Materials, Dresden, Germany

Motivation

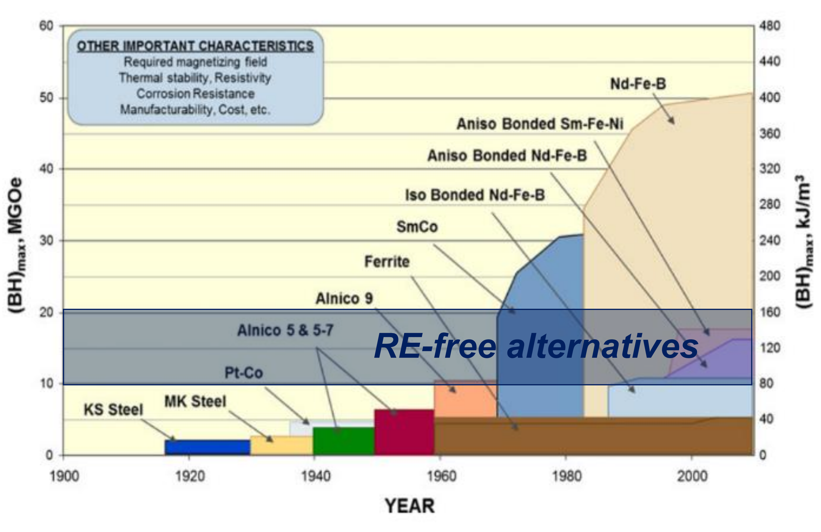

M.J. Kramer *et al.*, JOM 64, 752 (2012)

Permanent magnets (PMs) are widely used in energy, transport and electronic applications. Alternative PMs with no rare-earths (REs) content are being investigated in order to plug the gap between ferrites and NdFeB magnets, which should be done under the premise of looking at feasible candidates [1]. MnAl alloy has shown up as a promising RE-free PM candidate provided development of the ferromagnetic $L1_0$ or τ-phase [2]. Studies on this alloy usually focus on obtaining a maximum content of τ-phase for an enhanced magnetization, however with a low coercive field. We have recently shown the possibility of increasing coercivity by nanostructuring and controlled phase transformation [3].

In this study, hot-pressing experiments have been done at 600 ºC using as starting material both gas-atomized and milled (60 s) MnAlC powder and, importantly, starting from pure ε-phase. For the aim of comparison, we have used the combination of adequate temperature and pressure attained in the hot-pressing process to manage simultaneously the ε-to-τ transformation and end with a bulk MnAlC magnet [4].

Morphological and microstructural characterization

Höganäs — Gas-atomized powders provided by Höganäs AB in the frame of the project ECNanoManga.

Compaction of gas-atomized powders

Compacted magnets obtained by hot-pressing being the ε-to-τ transformation managed simultaneously.

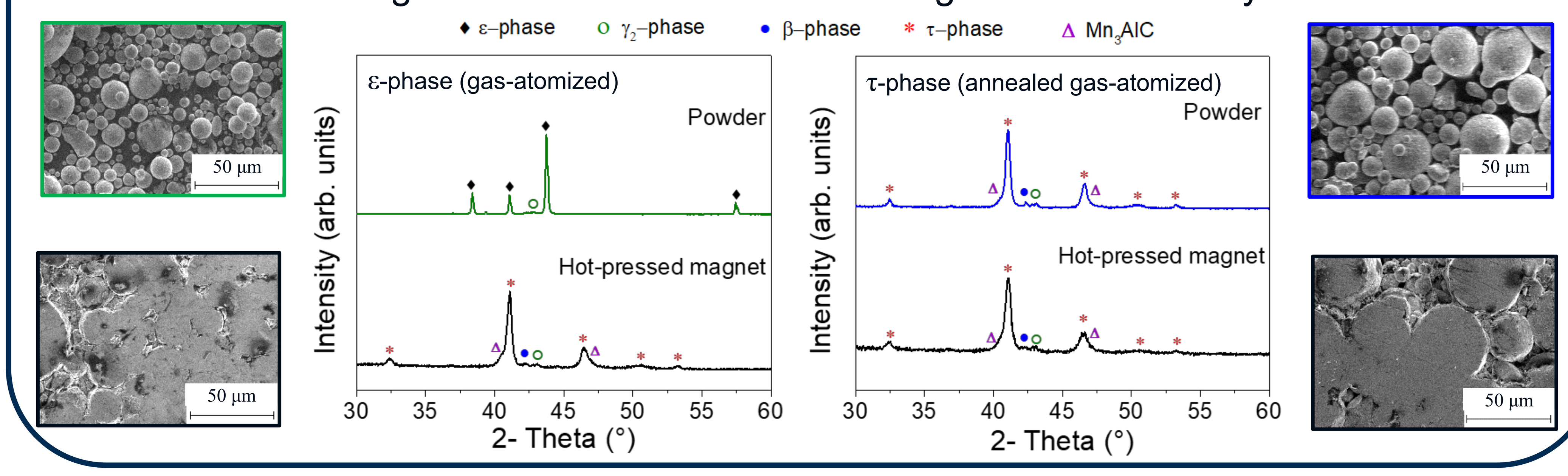

Compaction of milled powders

Combination of τ- and β- phases after hot-pressing of milled powders.

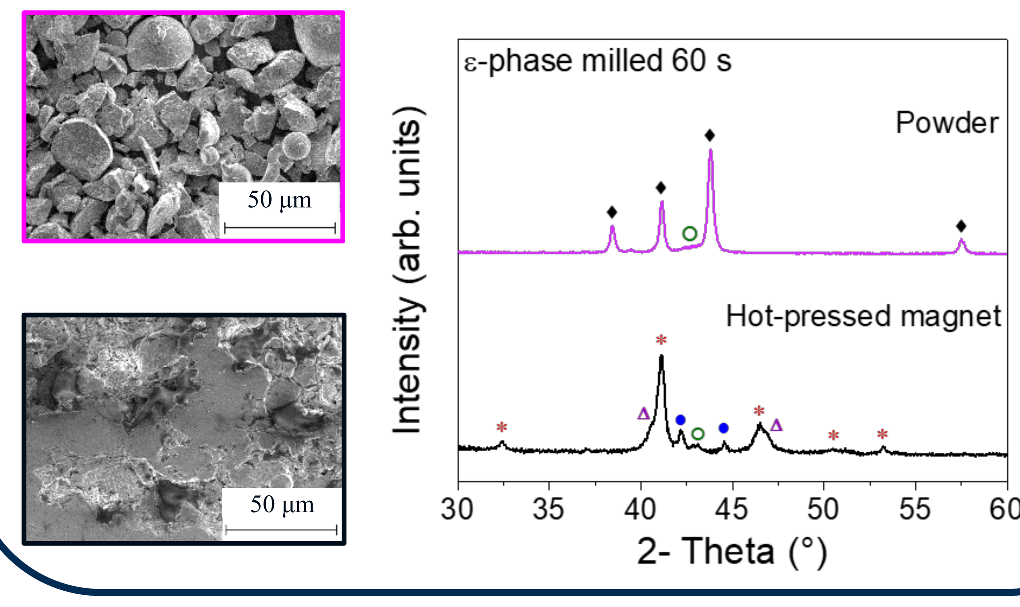

Magnetic properties

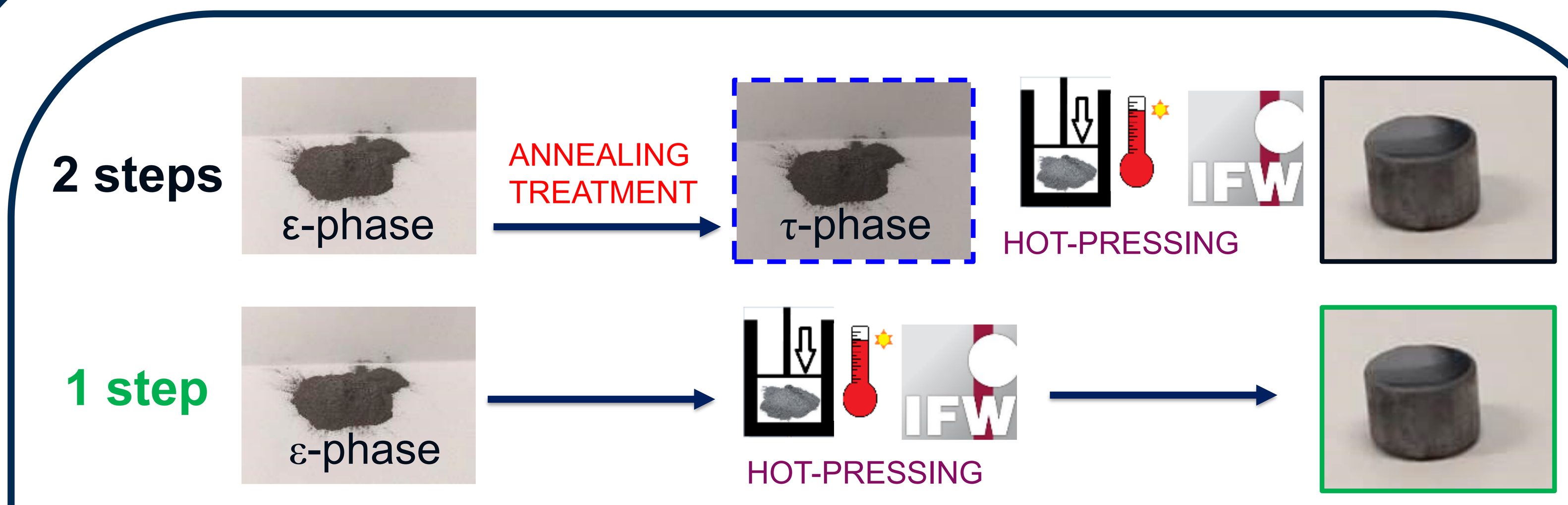

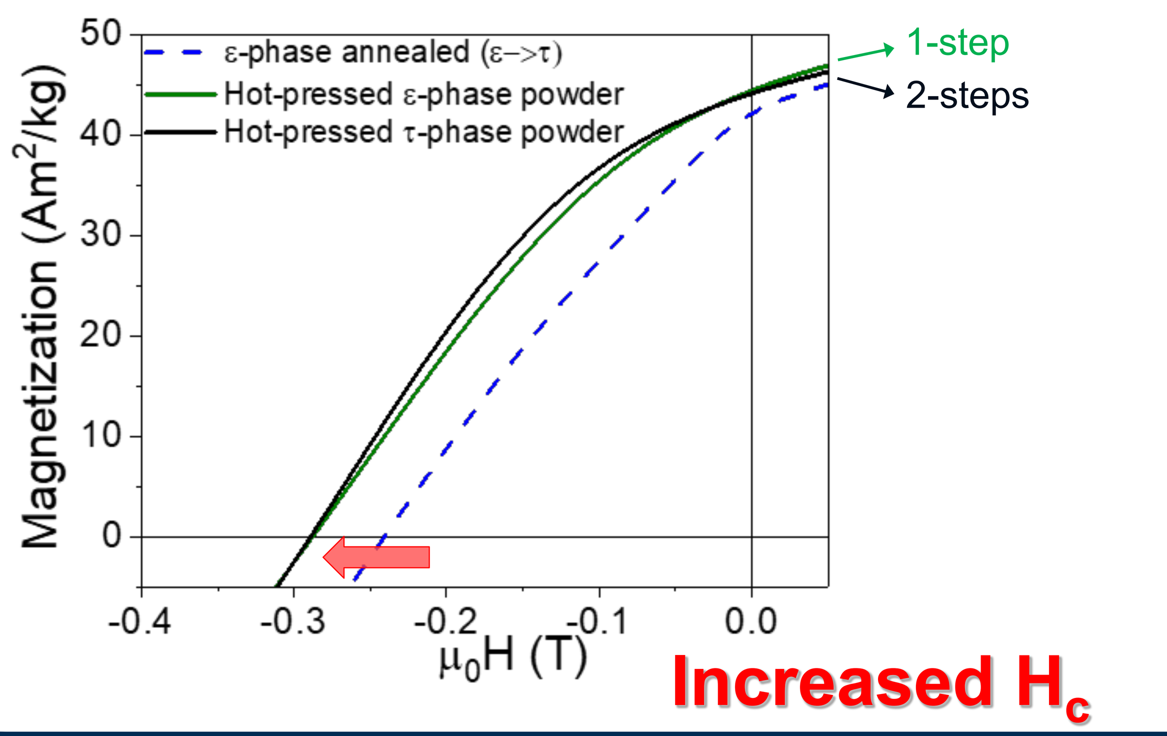

Increased H_c

Crystallite size (nm)	Strain (%)
32	0.33
27	0.39
28	0.36
24	0.42

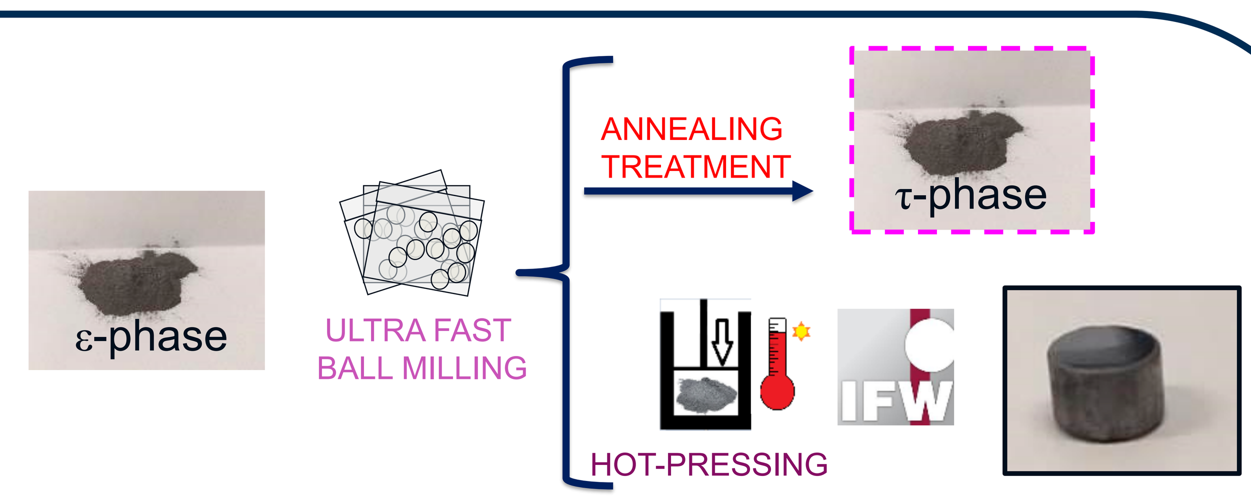

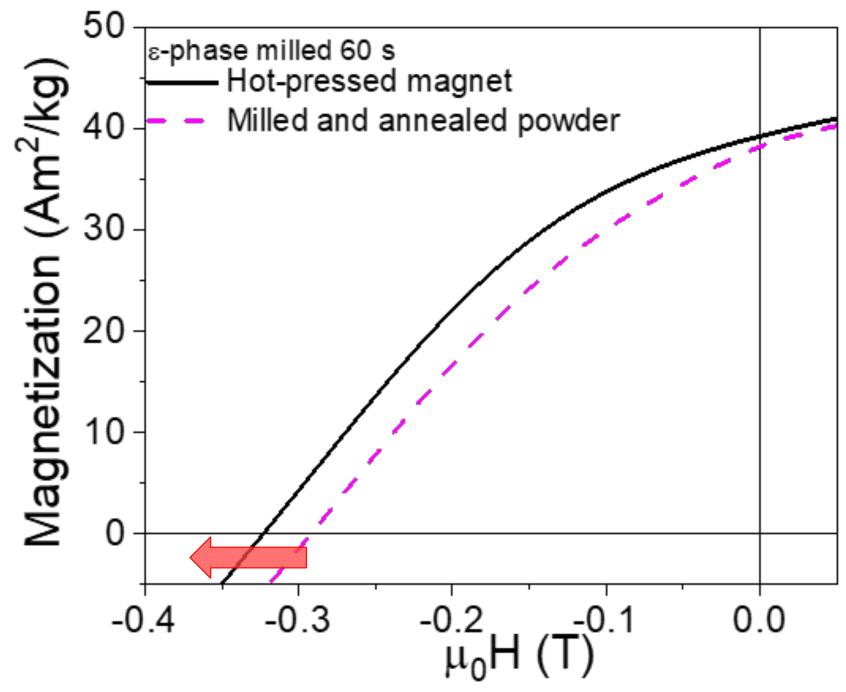

Conclusions

- **Simultaneous ε-to-τ phase transformation** ending with a bulk magnet in a **single step** by hot-pressing.
- Magnets with an **enhanced coercivity** have been obtained by compacting milled powders.
- **After compaction coercivity increases** due to:
  - Induced microstrain
  - Refined grain size
  - Precipitation of fine carbides

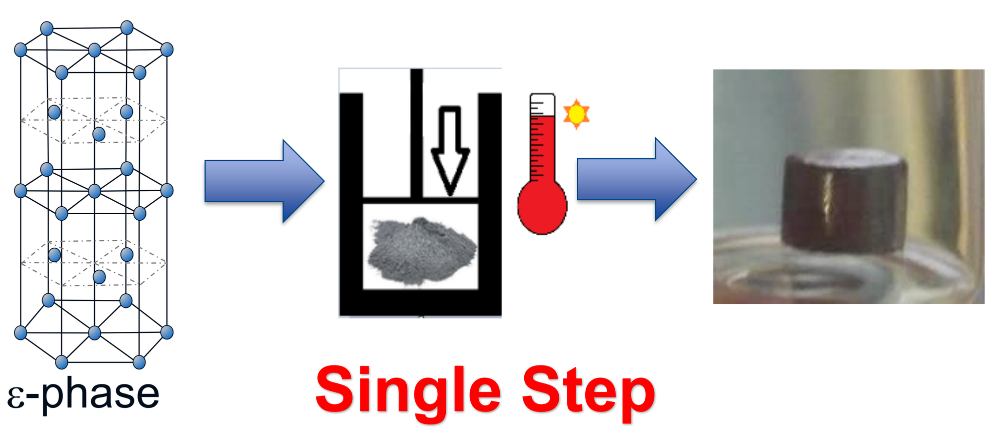

Single Step and Increased H_c

Future work

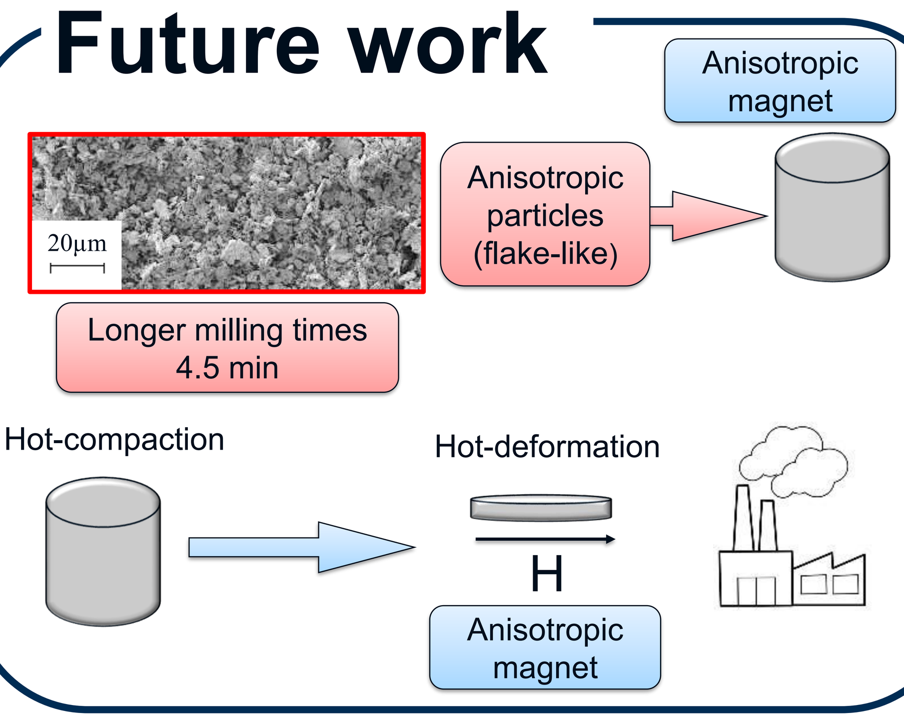

References:
[1] J.M.D. Coey, *IEEE Trans. Magn.* 47, 4671 (2011).
[2] H. Kono, *J. Phys. Soc. Japan* 13, 1444 (1958).
[3] J. Rial *et al.*, *Acta Mater.* 157, 42 (2018).
[4] C.Muñoz-Rodriguez *et al.*, *J. Alloys Compd.* 847, 156361 (2020).

EUROPEAN UNION STRUCTURAL FUNDS
GOBIERNO DE ESPAÑA — MINISTERIO DE CIENCIA, INNOVACIÓN Y UNIVERSIDADES
EXCELENCIA SEVERO OCHOA 2017 - 2021
Comunidad de Madrid
NexMag — M-era.Net — M.era-Net Success case — PCIN- 2015-126
ECNanoManga — Industrial Project & PhD Sponsorship — Höganäs
3DMAGNETOH — MAT2017-89960-R
nano mag COST — magnetism solutions for societal challenges — P2018/NMT-4321

Spin waves in cylindrical nanowires in the vortex state

Diego Caso[1], Cristina Bran[2], Manuel Vázquez[2], Konstantin Guslienko[3,4] and Farkhad G. Aliev[1]

[1]Departamento de Física de la Materia Condensada C03, Universidad Autónoma de Madrid, Spain. [2]Instituto de Ciencia de Materiales de Madrid, ICMM-CSIC, Madrid, Spain. [3]Departamento Física de Materiales, Universidad del País Vasco, UPV/EHU, 20018, San Sebastián, Spain. [4]IKERBASQUE, the Basque Foundation for Science, 48013, Bilbao, Spain.

Magnetic nanowires (NWs) have recently received considerable attention due to their potential applications in magnetic storage technology. While their static magnetic properties have been well investigated, their magnetization dynamics have received less attention **[1,2]**. Due to their reduced dimensions, the possibility to control spin wave (SW) confinement in the direction perpendicular to the NW´s axis and the possibility to couple electromagnetic waves to the magnetization textures with non-trivial topologies (e.g. the vortex state), designates these patterned structures as good candidates to next generation SW based information processing technologies.

Here we present experimental results of dynamic stimulation of hexagonally ordered arrays of Fe28Co63Cu10 NWs with 120 and 150 nm diameter, 300 nm lattice constant and few tens of microns in length. Microwave permeability investigated with DC and microwave magnetic fields perpendicular to the nanowire axis shows enhanced losses in the low frequency range range for magnetic field below 2 kOe.

In order to understand this behavior, we have simulated spin waves in 1-5 micron long range. We observed the formation of a vortex state on the NW ends for a field close to the one with experimental losses. We have also carried out a detailed investigation of how the excited SW modes depend on the NW length, as well as its evolution as a function of the distance from the NW end and the product of vortex polarity and vortex chirality. Our simulations are able to distinguish between two different types of the SW modes: lower frequency modes localized close to the NW ends and higher frequency delocalized modes, which are described as plane waves with a finite pinning at the NW ends.. The simulation results are in qualitative agreement with the analytical model based on the generalized Thiele equation for the vortex core string. The model accounts for the exchange and non-local magnetostatic interactions.

http://webs.fmc.uam.es/magnetrans.group/

Sample Growth and Characterization

Substrate: Highly ordered Anodized Aluminium Oxide (AAO) templates

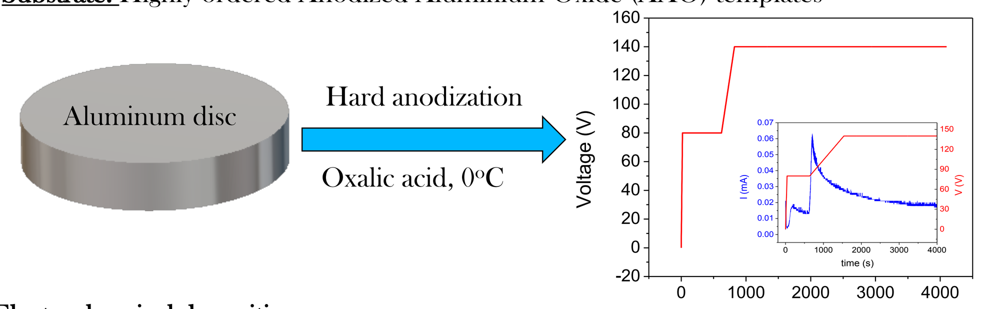

- Anodic Aluminum Oxide (AAO) templates
- Rapid growth ≈ 50 μm/hr
- Ordered pores with D=100-200 nm
- Inter-distance (center to center): D_i=300-320nm

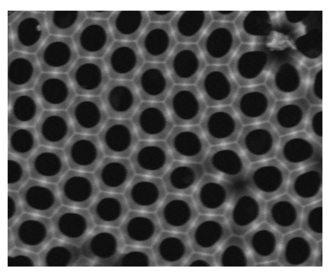

SEM top-view image of alumina template with highly hexagonal order

Electrochemical deposition:

Three-electrode cell using a single Watts-type bath, containing the different element sulfates:

$CoSO_4{\cdot}7H_2O$ (35g/l), $CuSO_4{\cdot}5H_2O$ (2g/l), $FeSO_4{\cdot}7H_2O$ (15g/l), H_3BO_3 (10g/l), and ascorbic acid (10g/l)

Electrodeposition potential: −1.5 V for FeCoCu, pH=3

Structural, morphologic and magnetic characterization:

- **X-ray diffraction (XRD) :** Crystallographic structure- *bcc*
- **Scanning Electron Microscopy (SEM):** sample geometrical parameters+composition
- **Vibrating sample magnetometer (VSM):** magnetic properties of NWs

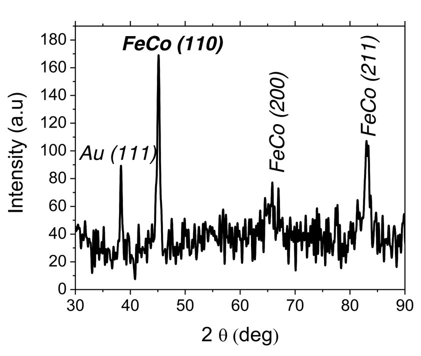

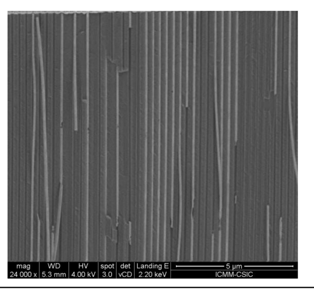

FeCoCu NWs embedded into alumina template

Sample Description and Experimental Results

$Fe_{28}Co_{63}Cu_{10}$

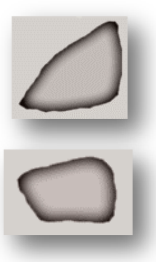

Thickness (NW length is 25 - 30 μm)

Separation between nanowires - 300 nm

Diameter of the NWs - 120 nm

Co NW, Au substrate

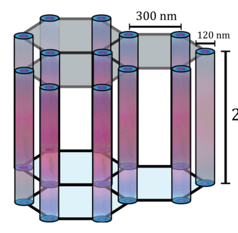

Hexagonal order

FMR experimental results

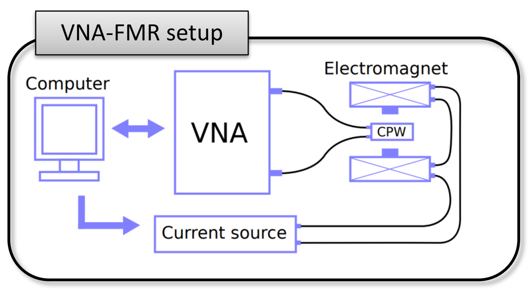

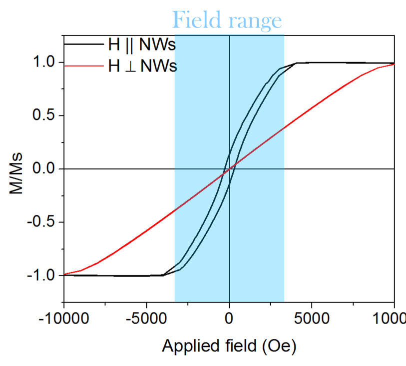

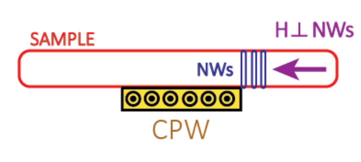

Field is applied perpendicularly to the NWs

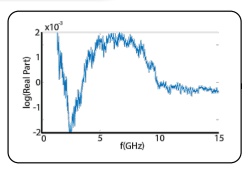

FMR results show losses in the low frequency range

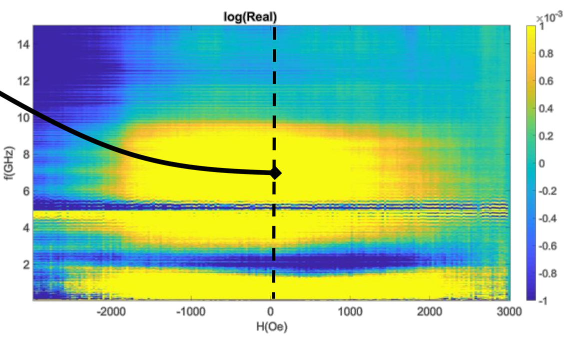

$$\mu \propto U(f,P,H) = \frac{S_{21}(f,P,H)}{S_{21}(f,P,H_{ref})}$$

Static Simulations

Magnetization distribution

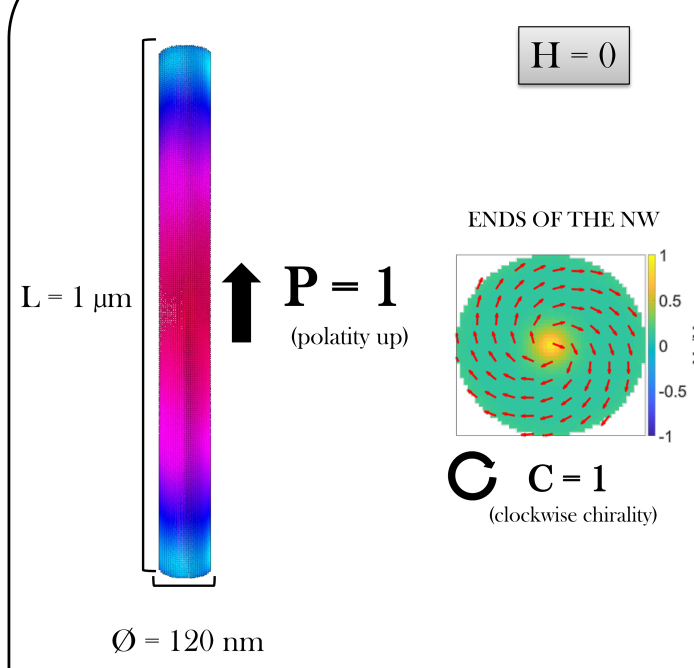

The 0 field magnetization distribution presents a clearly polarized NW in the middle section and two vortex states in the ends of the system.

Exchange energy distribution

Perpendicular field displaces the vortex core

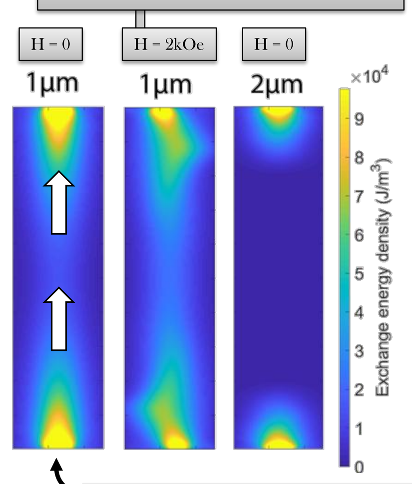

Possible channel for SWs

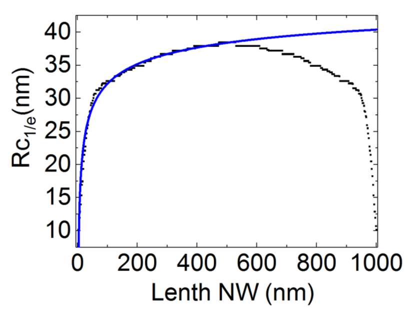

$$Rc(z) = a\left(\frac{1}{z}\right)^{1/n} + b$$

Critical radius is symmetric

The importance of the vortices rely on the fact that **exchange energy is accumulated** in these areas of the nanowire, so spin waves (SWs) could be generated by exciting one end and propagating along the nanowire using the radius of the vortices as a transmission channel.

Dynamic Simulations

Average modes of the system

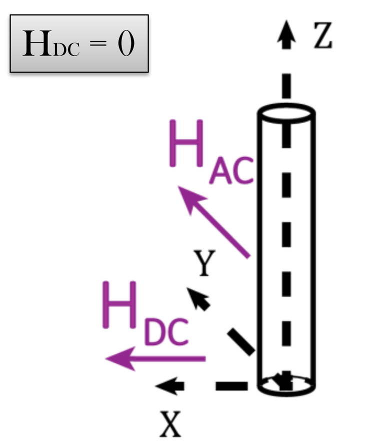

Gaussian pulse perpendicular to the system is applied to excite modes in the NW

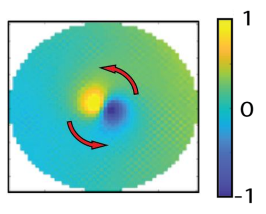

Very low frequency gyrotropic mode

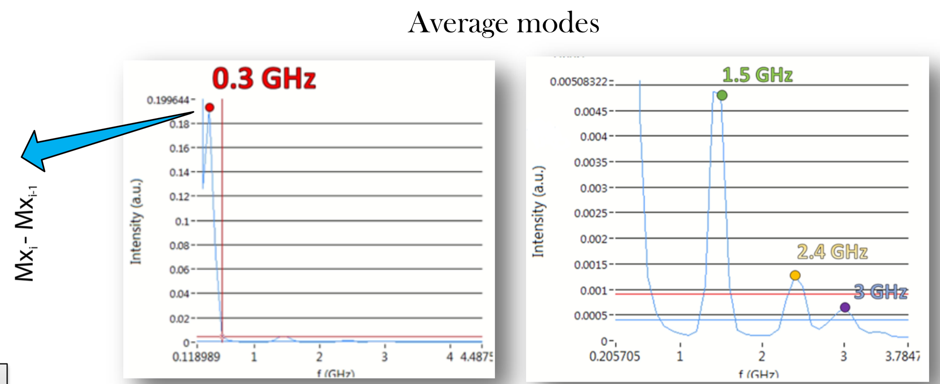

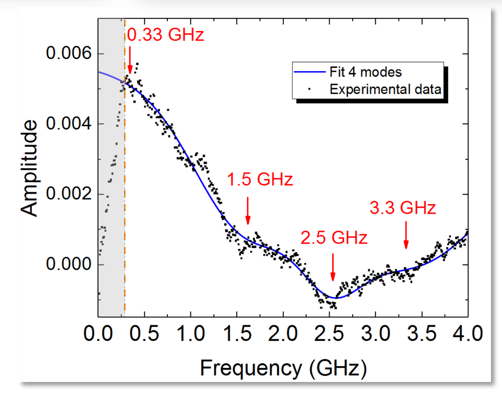

Experimental losses are located in agreement with where the simulations predict the average modes to be

In Depth Study of the System's Modes

Modes along the length of the NWs

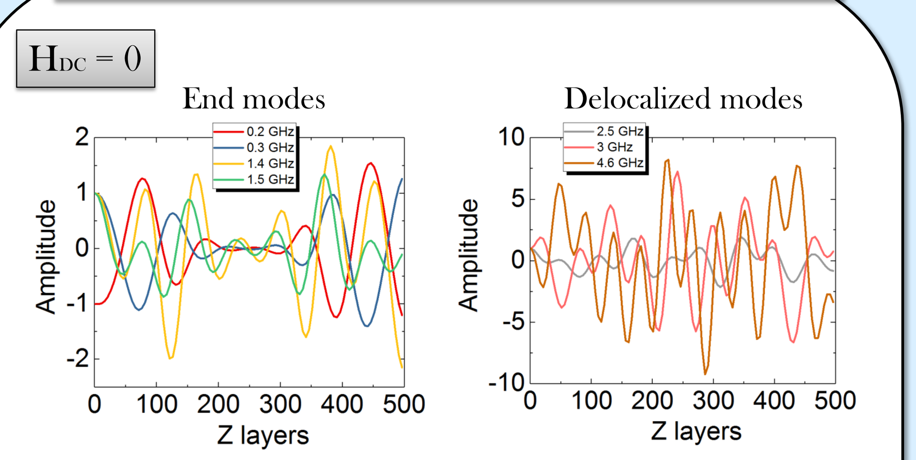

Low frequency modes correspond with modes with more amplitude at the end of the NWs (end modes) while high frequency modes are more present inside of the NWs (delocalized modes)

End modes could be combined with the fact that there is an excess of exchange energy in the ends to propagate spin waves along the NWs

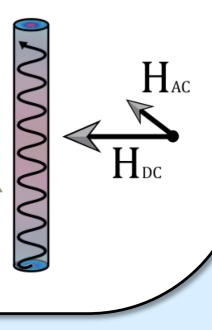

Mode variation with polarity and chirality

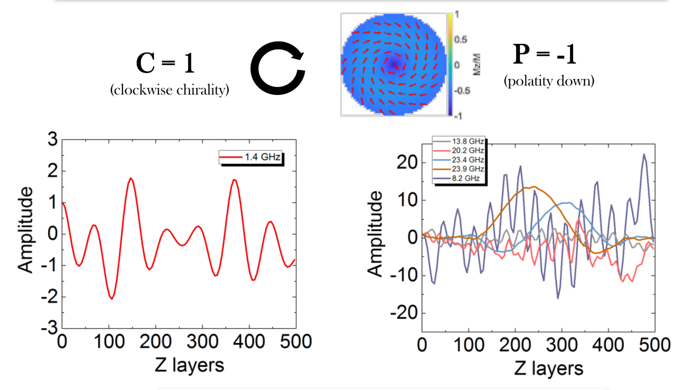

The original state with P = 1 presents much more end modes

Difference between pc=1 and pc=-1

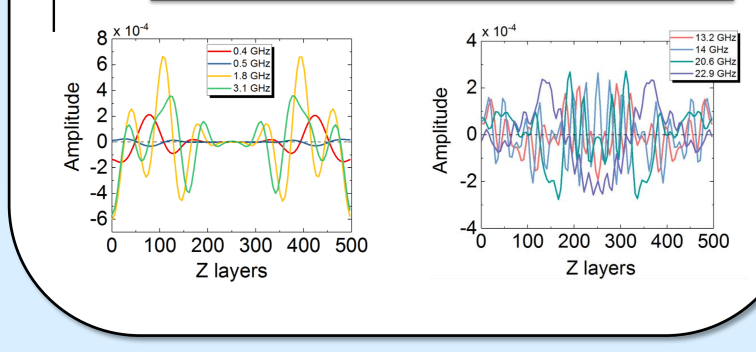

Longer NWs and Modeling

Longer NWs

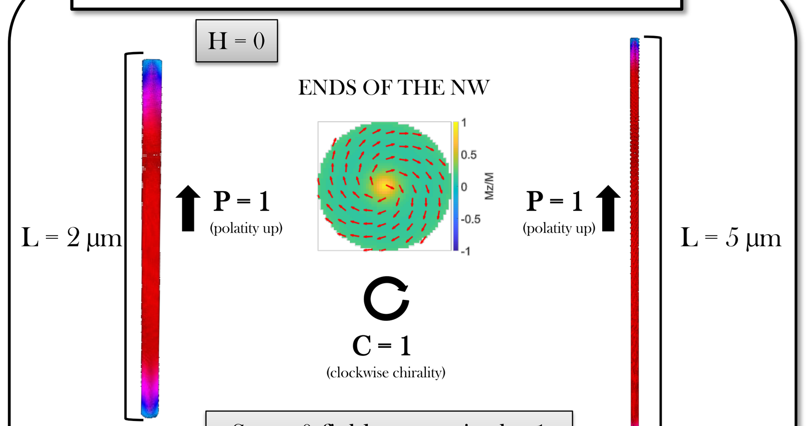

Same 0 field state as in the 1 micron case

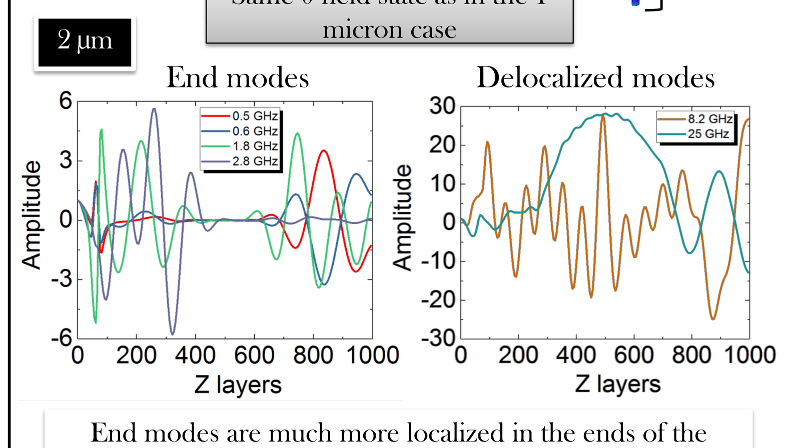

End modes are much more localized in the ends of the NWs when the length is increased, meaning that the propagation of the SWs along the NWs is harder

Theoretical modeling

The vortex gyrotropic non-uniform oscillations along the nanowire length are calculated. We use a **Thiele equation** to describe the vortex core motion including magnetostatic and exchange forces assuming that magnetization as a function of the cylindrical coordinates **r** = (**ρ**,z) and time can be written in the form **M**(**r**,t) = **M**(**ρ**,**X**(z,t)) , where **X**(z,t) is the vortex core displacement. If a local vortex mass term is accounted, the equation of motion is:

Thiele Equation

$$M_v\ddot{\boldsymbol{s}} + \boldsymbol{g}\times\dot{\boldsymbol{s}} = -\frac{\partial w}{\partial \boldsymbol{s}} + \frac{\partial}{\partial z}\frac{\partial w}{\partial(\partial \boldsymbol{s}/\partial z)}$$

M_v : vortex mass per unit of NW length ; s = X/r : dimensionless vortex core position ; R : nanowire radius
g = $g_z\hat{z}$; |g| = $2\pi M_s/\gamma$: gyrovector density per unit length ; w : energy density defined by the expression W = V∫dz w/π
W[s(z)] = W_m[s(z)] + W_{ex}[s(z)] : NW energy consisting of the exchange and non-local magnetostatic contributions

Making a Fourier transform **s**(z,t) = **s**(z,ω)exp(iωt)), the Thiele equation can be written as 2-component differential-integral equation. Its solution yields the eigenfunctions $s_n(z)$ and eigenfrequencies ω_n of the vortex string oscillations in the nanowire.

The low-frequency modes are localized near the nanowire ends. The higher frequency mode dispersion relations are not reciprocal (contain a term linear in wave vector depending on the vortex core polarization and chirality).

References

[1] Cristina Bran et al. *Magnetization Ratchet in Cylindrical Nanowires.* ACS Nano 2018, 12, 5932–5939

[2] J.A. Fernandez-Roldan et al. *Magnetization pinning in modulated nanowires: from topological protection to the "corkscrew" mechanism.* Nanoscale, 2018, 10, 5923

The work has been supported by Spanish MINECO (RTI2018-095303-B-C55; EUIN2017-87474) and the Comunidad de Madrid through NANOMAGCOST-CM (P2018/NMT-4321). DC acknowledges contract PEJ-2018-AI/IND-10364 from Comunidad de Madrid.

Modelling of magneto-thermoelectric response from a domain Wall

E. Saugar,[1] R. Puttock[2], C. Barton[2], P. Klapetek[3], T. Ostler[4], O. Kazakova[2], O. Chubykalo-Fesenko[1]
[1]Instituto de Ciencia de Materiales de Madrid, ICMM – CSIC, Spain
[2]National Physical Laboratory, Hampton Road, Teddington TW11 0LW, UK
[3]Czech Metrology Institute, Okruzni 772/31, Brno 10135, Czech Republic
[4]Sheffield Hallam University, Howard Street, Sheffield, S1 1WB, UK

Motivation

The motivation of this work is the understanding **scanning thermoelectric microscopy**, which is a powerful tool to make images of spins textures.
It is related with magneto-thermoelectric effects, which are non-equilibrium phenomena related to spin, charge and energy transport.
In this work, we have found that the experimental observations can be well understood by considering the Anomalous Nernst effect (ANE) in combination with Spin Seebeck effect (SSE).

The probe produces higly localized heat

↓

Spin transport & Thermoelectric phenomena

↓

Mapping the thermoelectric response in 2D

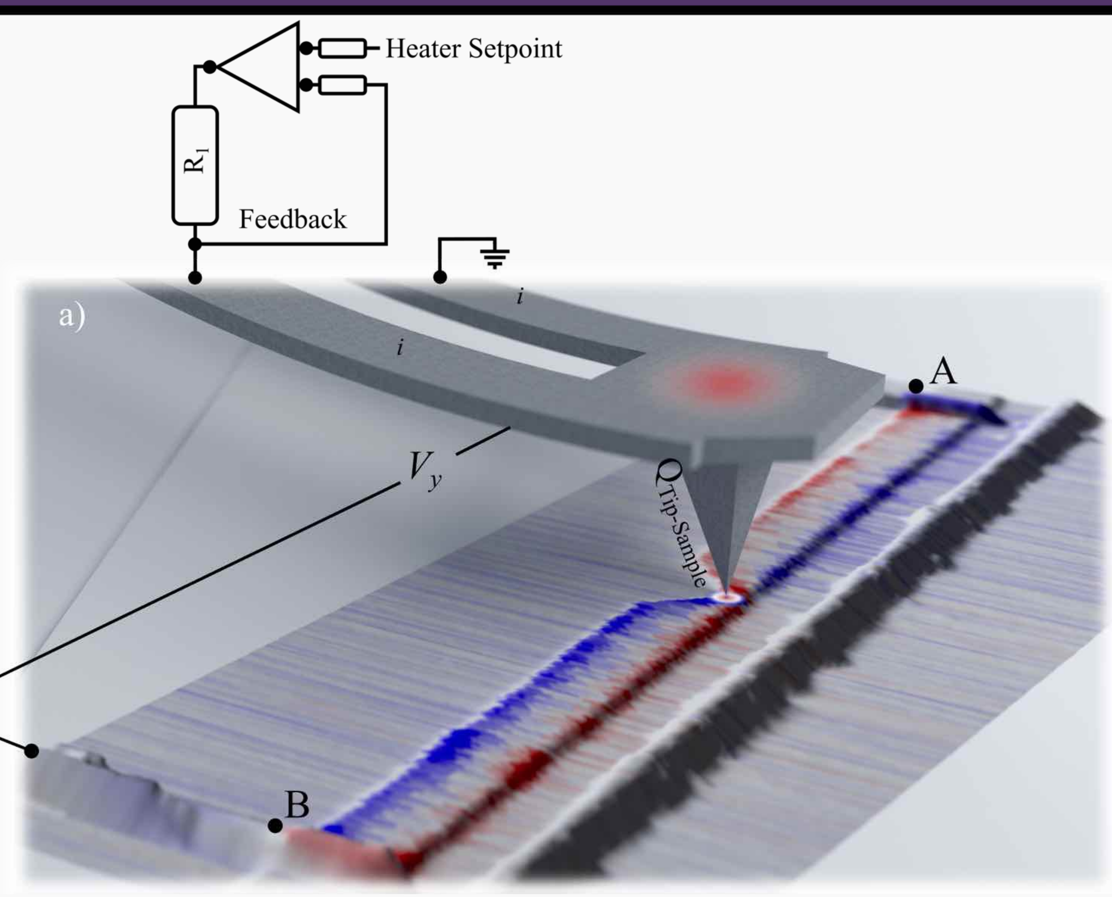

Modelling

Numerical integration of LLB equation [1]:

$$\frac{d\mathbf{m}_i}{dt} = -\gamma\left[\mathbf{m}_i \times \mathbf{H}^i_{\text{eff}}\right] + \frac{\gamma\alpha_\parallel}{m_i^2}\left(\mathbf{m}_i \cdot \mathbf{H}^i_{\text{eff}}\right)\mathbf{m}_i - \frac{\gamma\alpha_\perp}{m_i^2}\left[\mathbf{m}_i \times \left[\mathbf{m}_i \times \mathbf{H}^i_{\text{eff}}\right]\right]$$

Thermal diffusion model as a function of probe position:

$-k\nabla^2 T = Q$ Ultra-thin layer → $\nabla_z T = 0$

Magneto-thermoelectric effects:

$$\begin{pmatrix} E_x \\ E_y \\ E_z \end{pmatrix} = -\begin{pmatrix} \nabla V_x \\ \nabla V_y \\ \nabla V_z \end{pmatrix} = \begin{pmatrix} S_\perp & -S_N & 0 \\ S_N & S_\perp & 0 \\ 0 & 0 & S_\parallel \end{pmatrix} \begin{pmatrix} \nabla T_x \\ \nabla T_y \\ \nabla T_z \end{pmatrix}$$

Diagonal: Spin Seebeck coefficients
Off diagonal: Anomalous Nernst coefficient

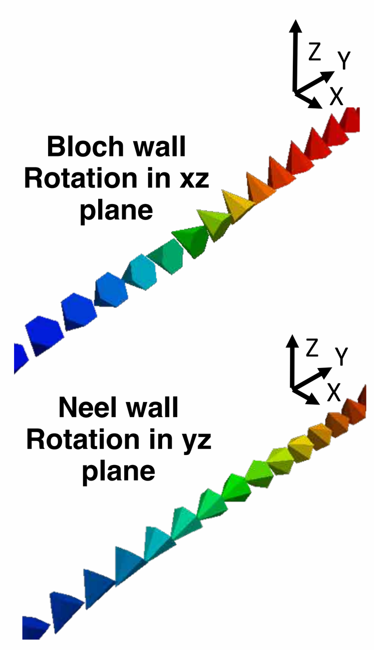

Model
- Ultra-thin trilayer Pt/FeCoB/Pt
- T_C = 433K (Fitted from exp.)
- High PMA ($K_{ani} = 9{\cdot}10^5$ J/m^3)
- Thickness = 5nm

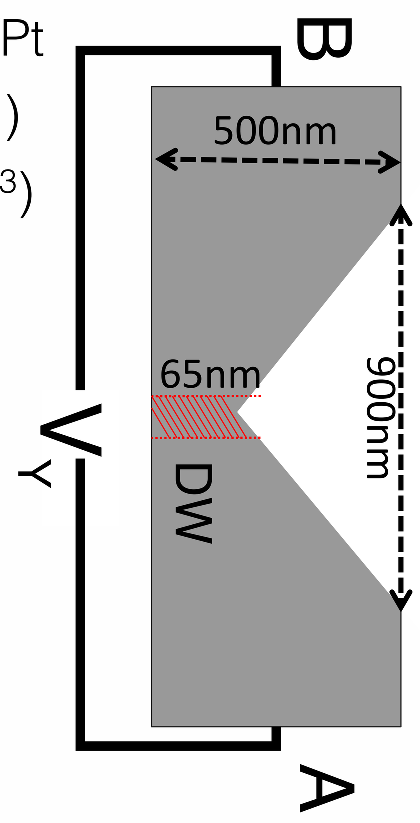

ANE – Neel/Bloch wall

$$V(x_0,y_0) = -\int \frac{dx}{w(x)} \int S_N \frac{m_z}{|m|} \nabla_x T(x_0,x,y_0,y)dy$$

SSE – Neel wall

$$V(x_0,y_0) = -\int \frac{dx}{w(x)} \int \left[S_\perp \left(\frac{m_z}{|m|}\right)^2 + S_\parallel \left(\frac{m_y}{|m|}\right)^2\right] \nabla_y T(x_0,x,y_0,y)dy$$

SSE – Bloch wall

$$V(x_0,y_0) = -\int \frac{dx}{w(x)} \int S_\perp \nabla_y T(x_0,x,y_0,y)dy$$

Magnetic configurations

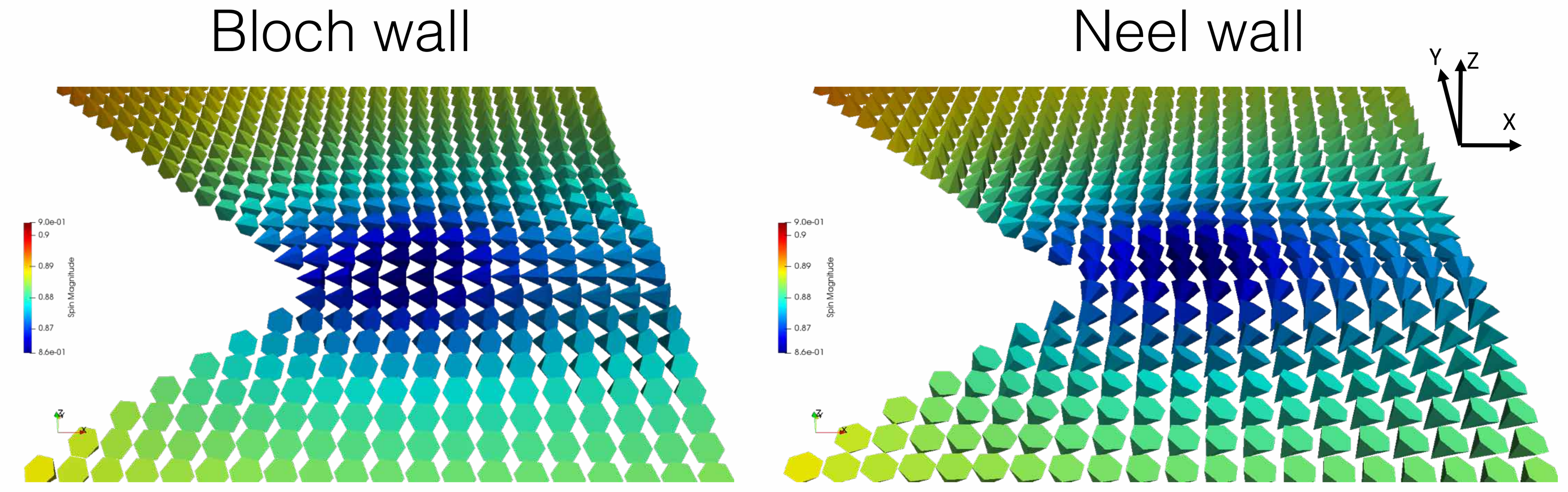

Heat spot & Domain Wall

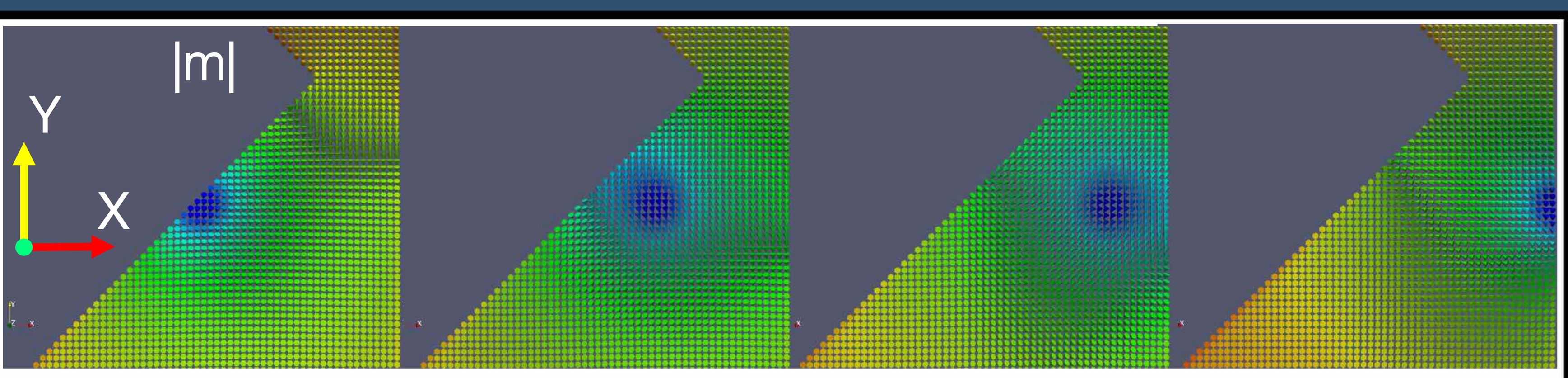

Domain Wall is deformed and can be depinned from the notch and attracted by the spot

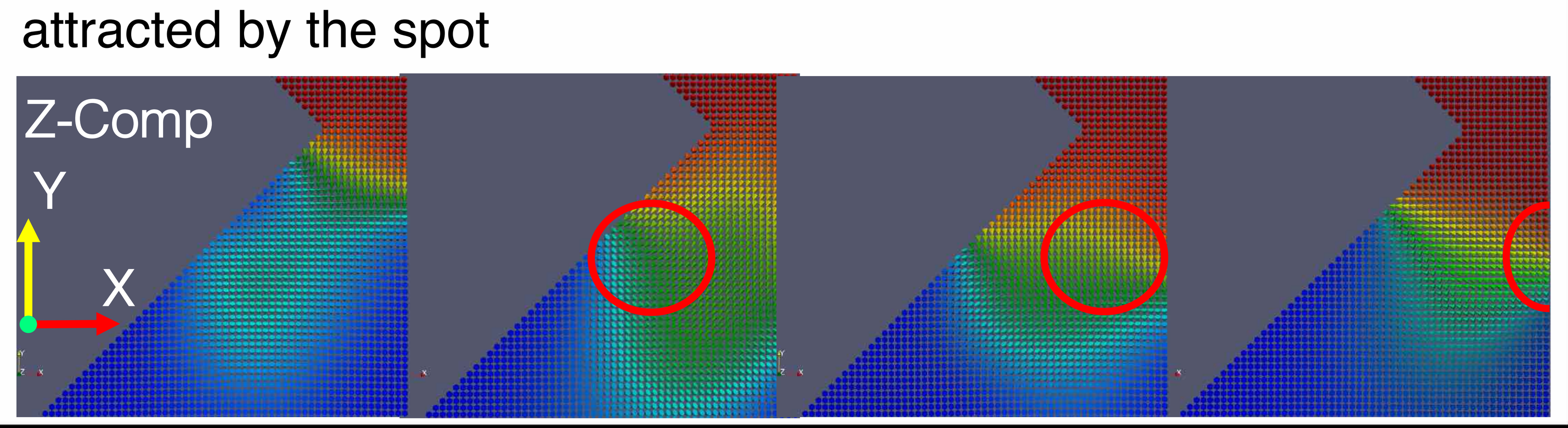

Bibliography

[1] O. Chubykalo-Fesenko et al., Phys. Rev. B 74, 094436 (2006)
[2] P. Krzysteczko et al., Phys. Rev. B 95, 220410 (R) (2017)

Experiment & Simulation

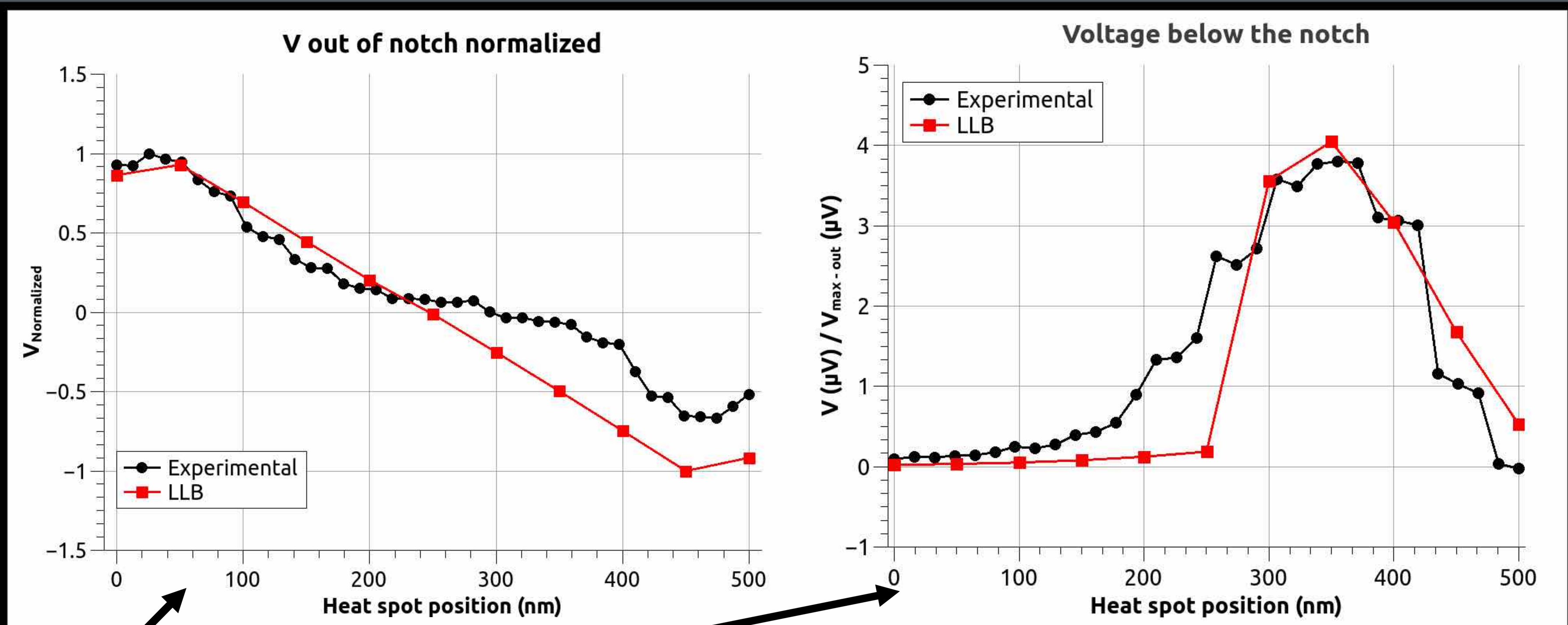

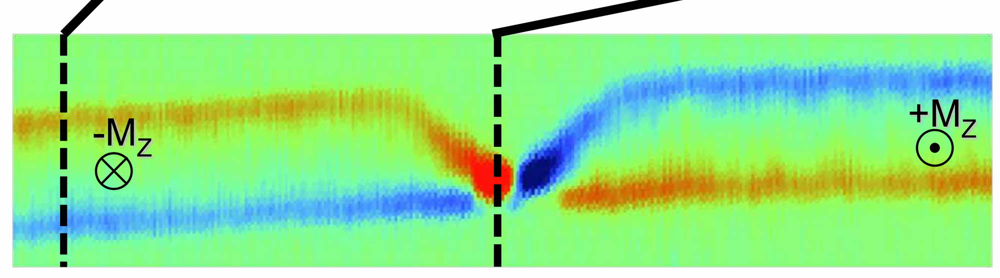

N_{ANE}	$-0.37\mu V/KT$	[2]
$S_\perp$	$-0.30\mu V/K$	Fitted
$S_\parallel$	$-0.95\mu V/K$	Fitted

Conclusions

- Scanning thermal microscopy is a powerful tool for mapping magnetic structures via thermo-magnetic effects: anomalous Nernst and spin-Seebeck.
- The ANE response is the same for Bloch and Neel domain walls.
- The Neel and Bloch domain walls can be distinguished via the asymmetry of the spin-Seebeck effect. (Fitted from experiment)
- Using the LLB micromagnetics and temperature distribution we modelled the induced voltage in FeCoB stripe with PMA and geometrical notch in agreement with experiment.
- Domain wall is deformed and can be depinned from the notch and attracted by the heat spot.

Mild Electro-mechanical Processing of Water-quenched Amorphous Microwires for Property Improvements

A. V. Inchausti[1], X. Zhang[2], A. Jacas[1], R.P. del Real[1], M. Butta[1,3], L.H. Lewis[1,2] and M. Vázquez[1]

[1] Instituto de Ciencia de Materiales de Madrid, CSIC. 28049 Madrid. Spain
[2] College of Engineering ,Northeastern University,. Boston, MA,02115 USA
[3] Faculty of Electrical Engineering, Czech Technical University in Prague. 16627 Prague. Czech Republic

Abstract

Rapidly solidification techniques like the in-rotating-water-quenching technique used to fabricate amorphous microwires generate strong mechanical stresses which coupled to magnetostriction, determine their magnetic properties in competition with exchange interaction plus shape anisotropy energy terms [1]. Amorphous microwires with zero-magnetostriction composition were prepared exhibiting an initial undulating shape due to quench instabilities [2]. However, most technological applications employing amorphous microwires rely on the quality of their geometrical and compositional homogeneity. Hence, here we report a novel mild electromechanical processing of the as-quenched wires that is demonstrated to improve their morphology without damaging their structural and magnetic properties to optimize their technological applicability.

I. SAMPLE PREPARATION AND ELECTROMECHANICAL TREATMENT

- Amorphous non-magnetostrictive microwires were prepared (d~130µm)
  - Using the In-rotating-water-quenching technique.
  - With alloy composition of $(Co_{94}Fe_6)_{72.5}Si_{12.5}B_{15}$ with vanishing magnetostriction, $\lambda_s \approx -1x10^{-7}$

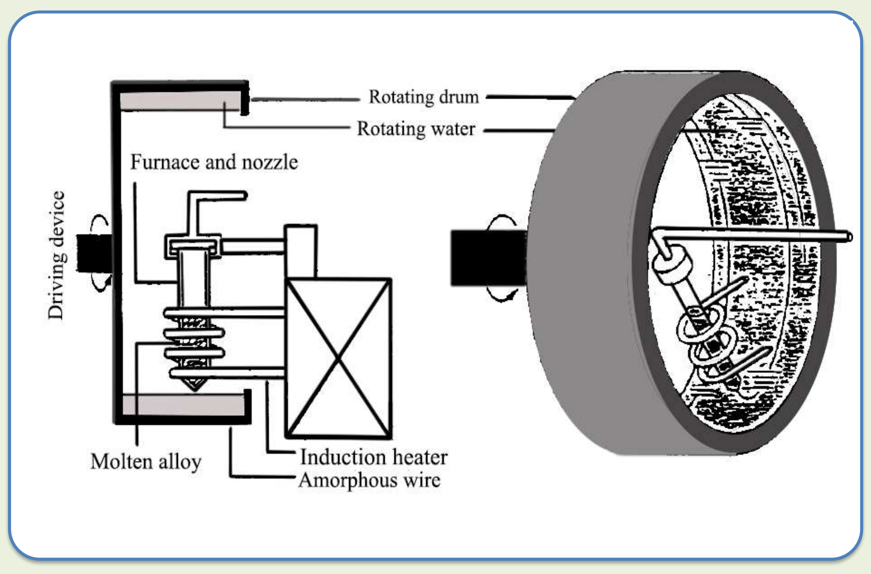

The magnetic behavior of amorphous microwires is significantly determined by their magnetoelastic anisotropy, E_{mel}, which depends on the magnetostriction constant, λ_s, and the frozen-in mechanical stresses, σ, as: $E_{mel.} = (3/2)\, \lambda_s\, \sigma$

Mild Electro-mechanical Treatment

Through **electromechanical annealing** (in as-quenched wires ~8 cm length)

1. Passing a maximum current density of 50 MA/m^2 for 140 sec
2. The load supplied a maximum 157g (≈ 170 Mpa tensile stress)

- **The samples end up showing a perfectly straight morphology after the treatment**

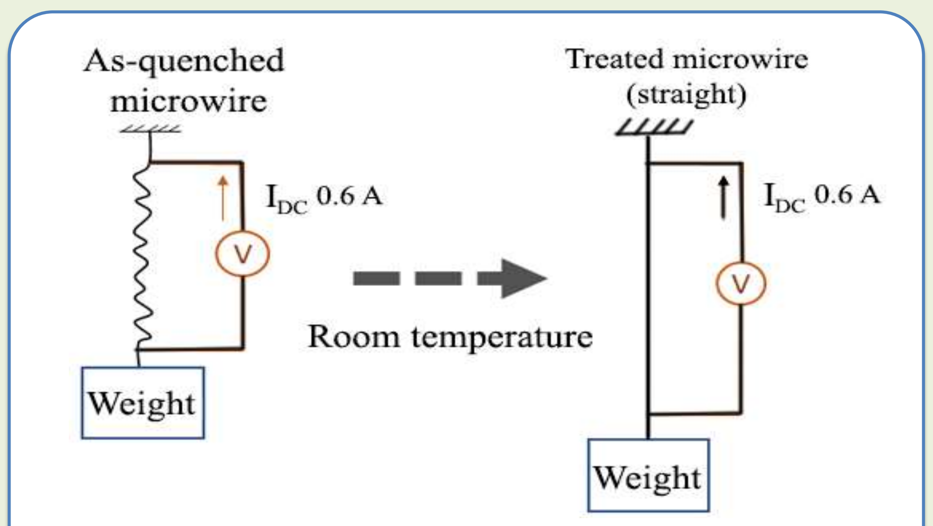

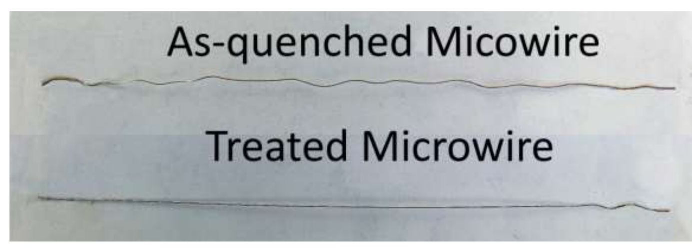

II. STRUCTURE ANALYSIS BY DIFFERENTIAL SCANNING CALORIMETRY, DSC, AND THERMOGRAVIMETRY, TGA.

- **DSC** and **TGA Analysis** performed for:

1. **As-quenched microwire** (curved)
2. **Treated microwire**(~45MA/m^2, 140s.)

The TGA curve is induced by a pair of magnets placed outside the DSC chamber, exerting a magnetic force on the magnetic sample

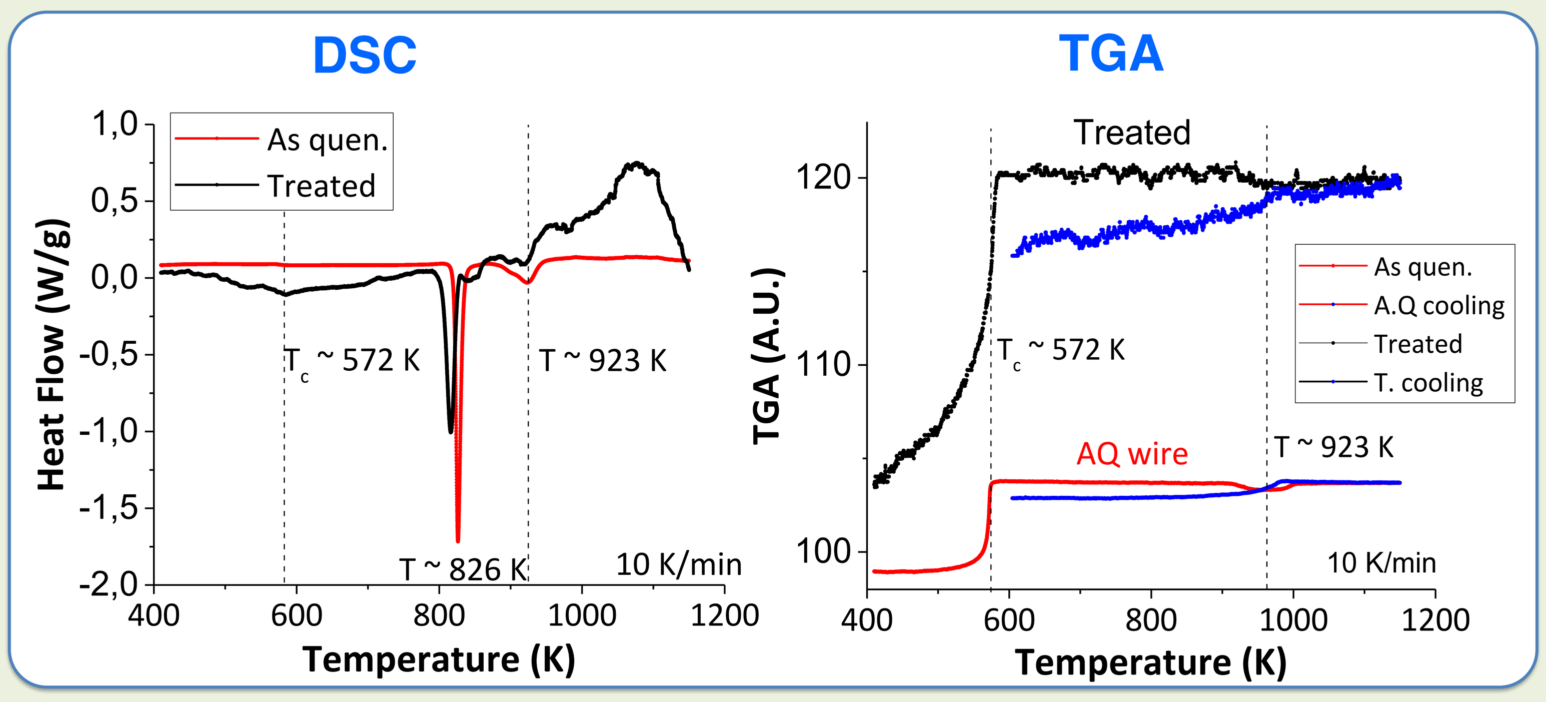

i. **DSC traces reveal a 2-stage devitrification process for temperatures above 800K observed for both, as-quenched and treated, samples (despite the low signal-to-noise ratio due to the small mass of the treated sample)**

ii. **TGA traces reveal the presence of magnetic transitions associated to discontinuities around ~ 923K**

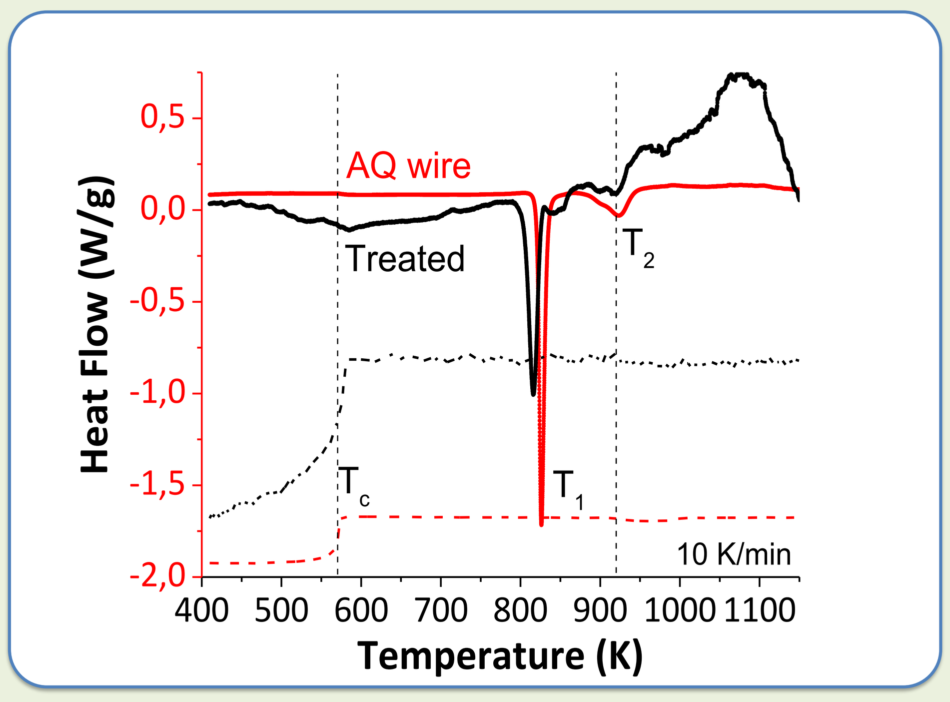

The differences between as-quenched and treated samples (particularly in the first devitrification peak) can be ascribed to slight structural relaxation, within amorphous state

III. MAGNETIC ANALYSIS BY VIBRATING SAMPLE MAGNETOMETER, VSM

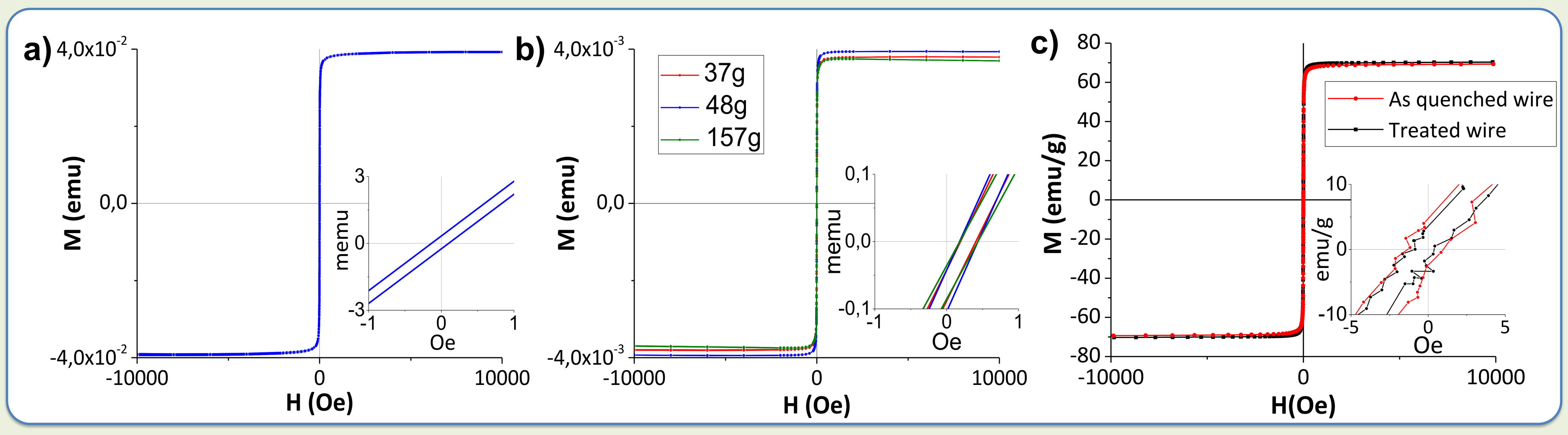

a) High and low field hysteresis loops of as-quenched microwire

- Typical of non-magnetostrictive wire:
- Lack of magnetic bistability
- Very low coercivity, ~0.2 Oe
- Very high susceptibility

b) Hysteresis Loops of treated microwires under various weights:

- The magnetic behavior is not modified significantly owing to the reduced magnetostriction

c) Comparison between hysteresis loops of as-quenched and treated microwires

- Small variation of magnetic properties

CONCLUSIONS

- Non-magnetostrictive amorphous microwires show simple domain structure and magnetization reversal making them ideal for micromagnetic studies as well as unique magnetic sensing applications.
- The novel mild electromechanical treatments described here :
  - Create small local structural rearrangement
  - Induce reduced changes in the magnetic behavior
  - Optimize the microwire morphology while maintaining the overall amorphous structure and soft magnetic stability.

References:

[1] Vázquez, M. (2007). Advanced Magnetic Microwires. *Handbook of Magnetism and Advanced Magnetic Materials* (2007), Ed. Kronmüller & Parkin (JWiley Vol 4, pp. 2192)
[2] Butta, M., *et al* .(2020). Dependence of the noise of an orthogonal fluxgate on the composition of its amorphous wire-core. *AIP Advances*, *10*, 025114.

Acknowledgments: This work has been supported by "Fulbright España" Program and the Regional Government of Madrid (Spain) .

Tuning Microwave Absorption Property of Few-layered Graphene/ Magnetic Microwires Composite Materials for Electromagnetic Interference Shielding

Álvaro Peña[1,2], Jesús López-Sánchez[1], Elena Navarro [1, 2], Pilar Marín [1, 2]
1 *Instituto de Magnetismo Aplicado, UCM-ADIF, 28230 Las Rozas, Spain*
2 *Departamento de Física de Materiales, Universidad Complutense de Madrid (UCM), 28040 Madrid, Spain*

Nowadays there's a huge number of technical applications that operates with electromagnetic waves at GHz frequencies, specially between 2-20 GHz, such as communications or radar systems. Microwave absorbing materials (MAMs) rise for the need of electromagnetic interference shielding in these applications.
For a material to be considered as an effective shield it should not only demonstrate strong absorbance in the desired range but also be thin, light, mechanical and environmentally resistant.
While magnetic microwires are well-know MAMs, they suffer from some drawbacks when used in composites like its high density and poor processability.
Graphene is used here not only for its high ε_r but for its outstanding properties as a reinforcer.

Absorbing mechanisms of these materials are due to:
- Conductive dissipations
- Polarization loss (interfacial, ionic, defects…)
- Resonance (related to wire geometry)
- Hysteresis loss

Few-layered graphene (FLG) is obtained by a ball milling method

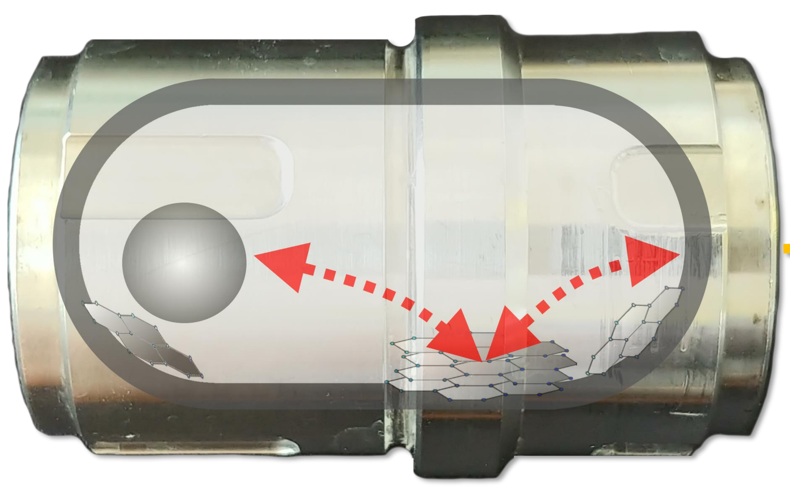

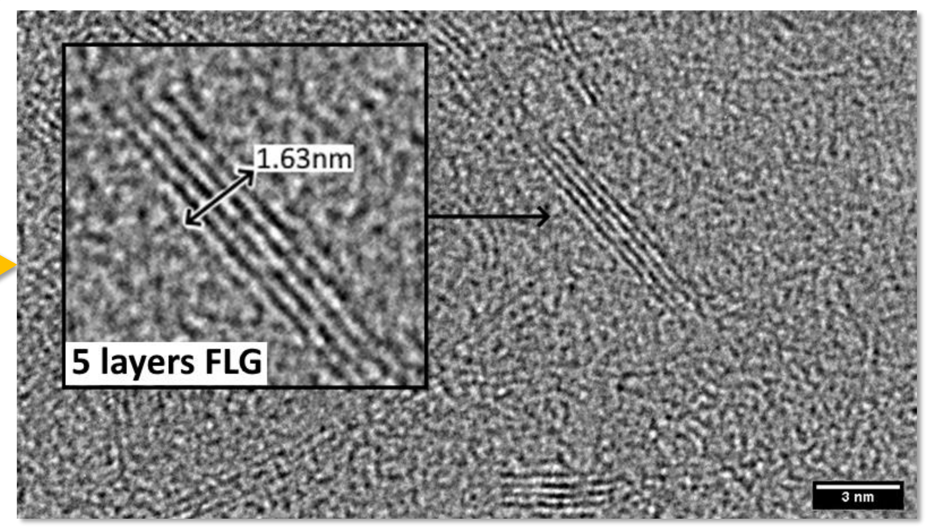

Microwires (MW) are cut to 4-6 cm lengths

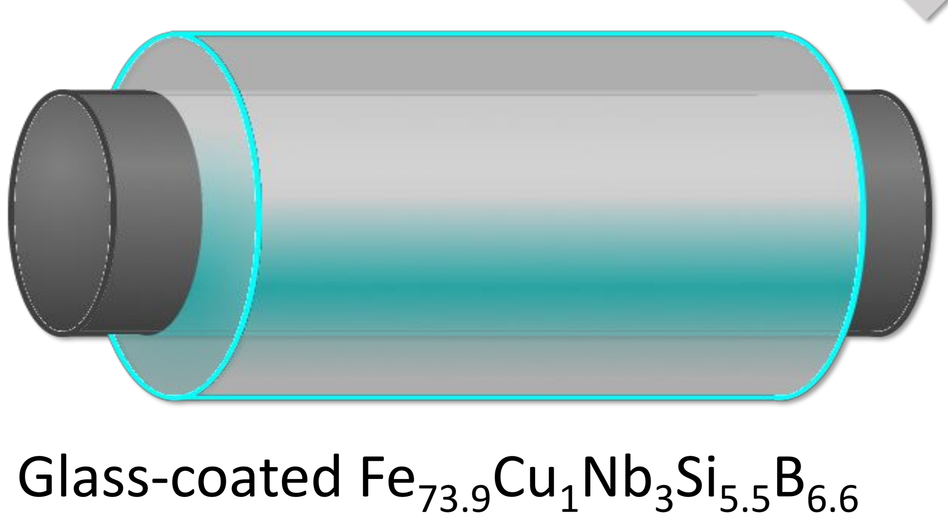

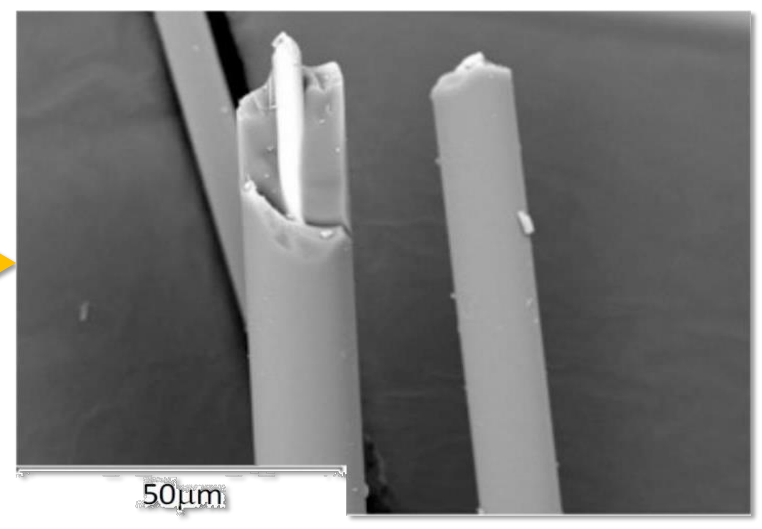

Preparation of the composite is achieved by mixing FLG and microwires with a commercial paint in different weight ratios and deposited over a dielectric material

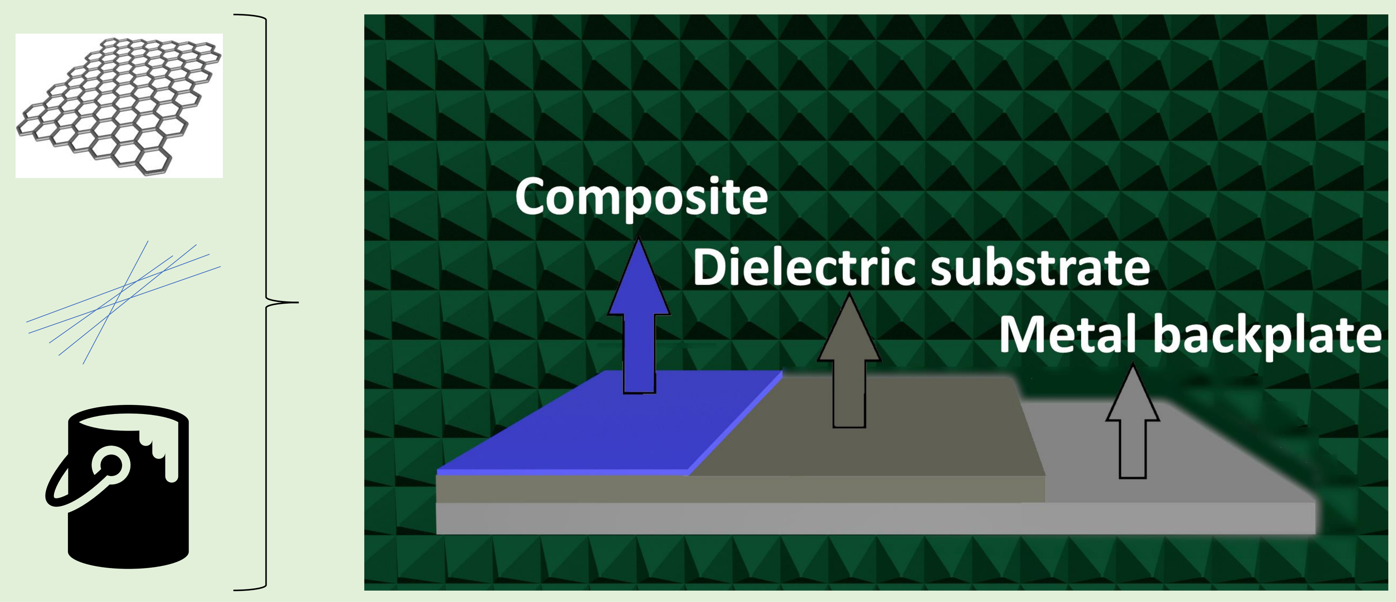

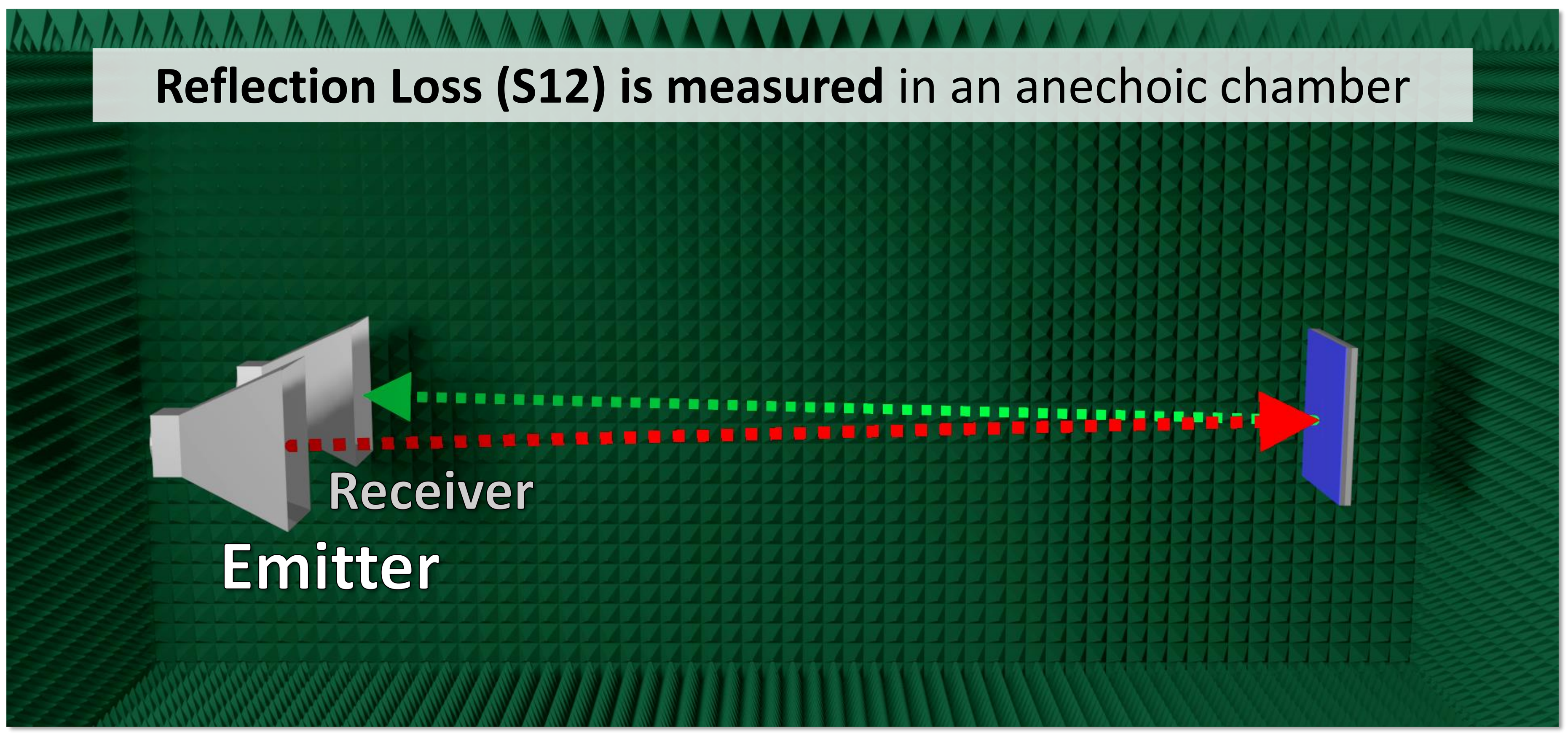

Reflection loss:

$$RL = 20\log\left[\frac{Z_{in}-1}{Z_{in}+1}\right]$$

Where Z_{in} is the impedance:

$$Z_{in} = \sqrt{\frac{\mu_r}{\varepsilon_r}}\, tanh\left[j\left(\frac{2f\pi d}{c}\right)\sqrt{\mu_r\varepsilon_r}\right]$$

μ_r is the complex permeability
ε_r is the complex permittivity
f is the frequency
d is the thickness of the paint

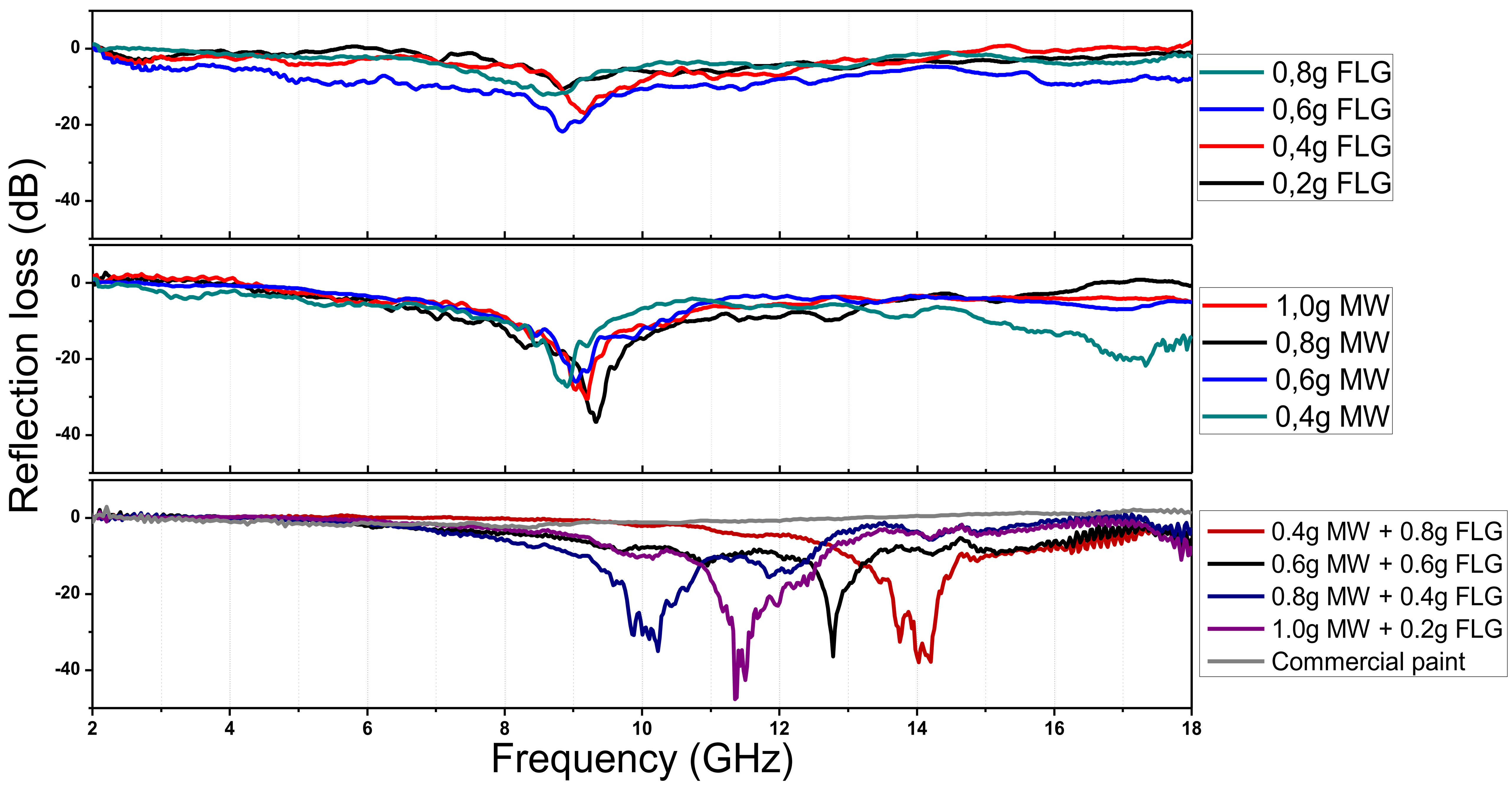

In summary, FLG modifies the permittivity of the composite affecting both the intensity and the frequency of the minimum reflection. Not only outperforming sole MW but allowing to tune the maximum shielding band.

Further work is required to fully understand the role of FLG on modifying the microwave absorbance behavior, including but not limited to ε_r characterization of FLG and preparation of different composites.

References
FLG synthesis: A. Peña, E. Navarro, J. López-Sánchez, P. Marín, D. Matatagui, M.C. Horrillo, *Patent nº* **ES 2779151 A1** (2020)
MW as MAM: P. Gueye, J. López-Sánchez, E. Navarro, A. Serrano, P. Marín, *ACS Appl. Mater. Interfaces.* **12** (2020) 15644-15656

Nucleation and current-induced bubble structures motion in PMA multilayers

J. Marqués-Marchán[1], M.C. Pérez-Carmona[1], J.L. Prieto[2], A. Asenjo[1]

[1] Instituto de Ciencia de Materiales de Madrid (CSIC), Madrid 28049, Spain

[2] Instituto de Sistemas Optoelectrónicos y Microtecnología, Universidad Politécnica de Madrid, Madrid 28040, Spain

jorge.marques@csic.es

Introduction

Perpendicular Magnetic Anisotropy (PMA) multilayers have been studied in the past for magnetic recording and information storage applications [1]. Since the discovery of Dzyaloshinskii-Moriya Interaction (DMI) [2, 3], the interest in PMA multilayers have been renewed. DMI promotes the development of magnetic bubbles and skyrmions, which are promising for spintronics applications due to their stability, small sizes, low-current densities for their motion, … [4]

CoPt samples growth

PMA multilayer grown by DC magnetron sputtering

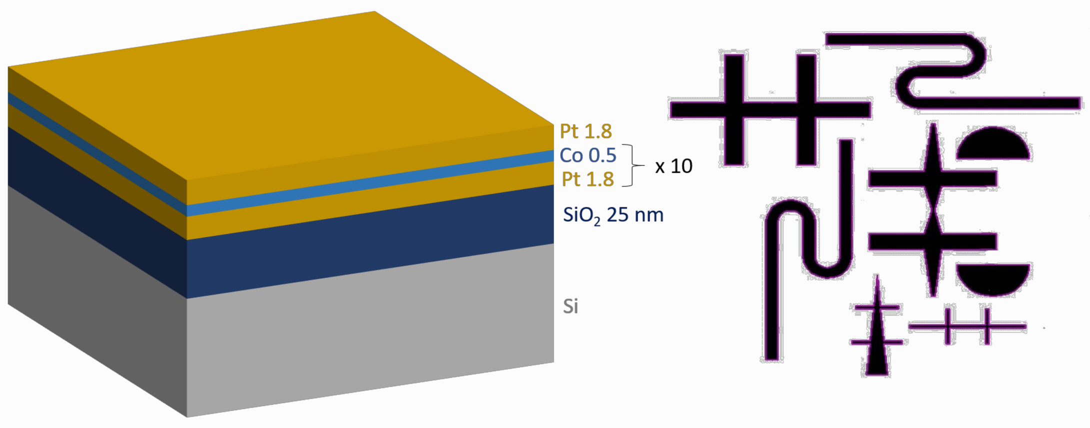

Apart from a thin film, some nanostructures by e-beam lithography were fabricated under the same conditions. These nanostructures present different lateral shapes and sizes.

Characterization: VF-MFM

Variable Field MFM

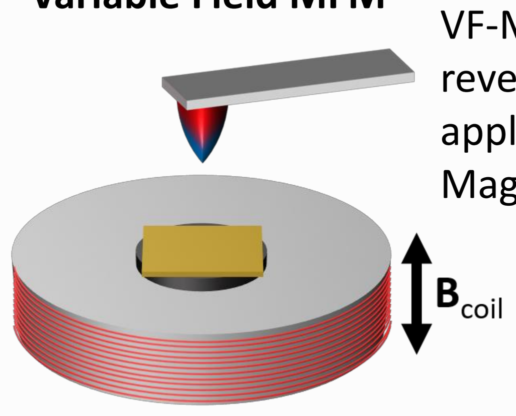

VF-MFM allows the study *in situ* of magnetization reversal processes of the sample by the application of an external magnetic field in the Magnetic Force Microscopy (MFM) system [5].

Tip-sample interaction

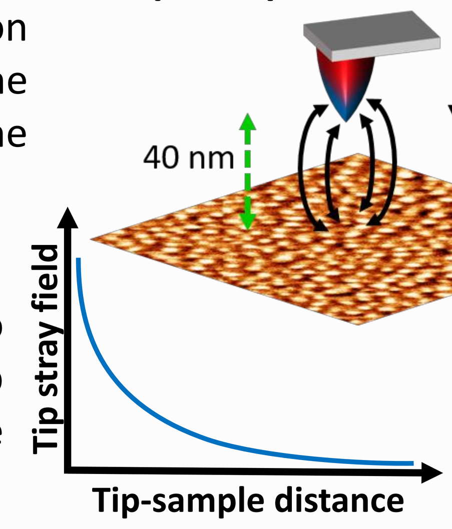

Tuning the tip-sample distance allows to change locally the magnetic field (tip stray field) on the sample, modifying the magnetization locally [6].

Stripe domains in thin film

MFM images in remanence state

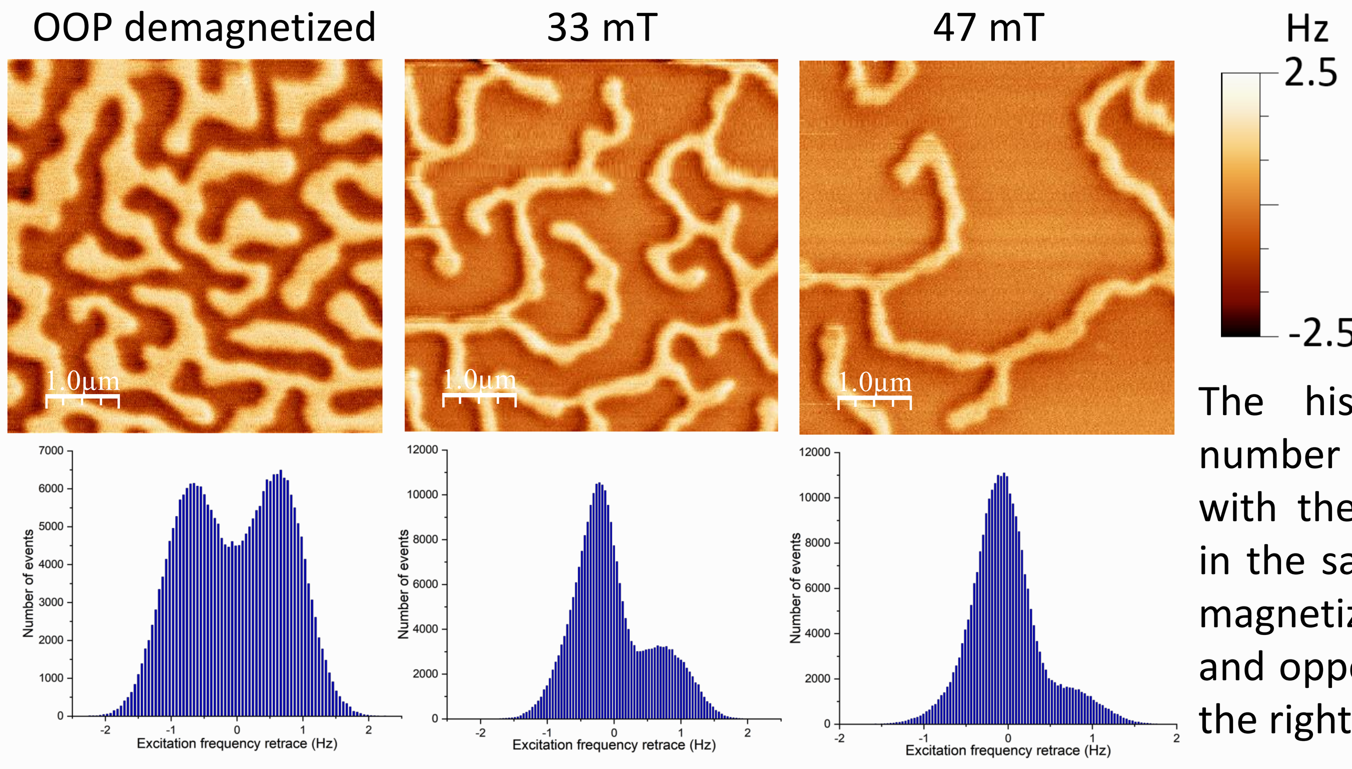

Applied field parallel to tip magnetization

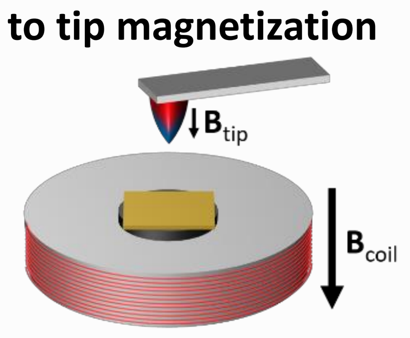

The histograms indicate the number of points in the image with the sample magnetization in the same direction of the tip magnetization (peak on the left) and opposite direction (peak on the right).

Applying a magnetic field in the same direction as the tip magnetization (dark contrast), stripes with an opposite magnetization of the one of the tip (bright contrast) get narrower and disappear progressively with the value of this field.

Bubble domains in thin film

Bubbles nucleation

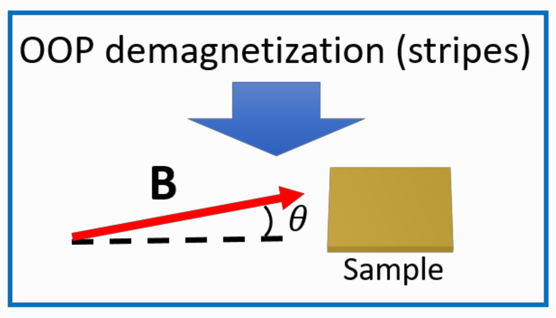

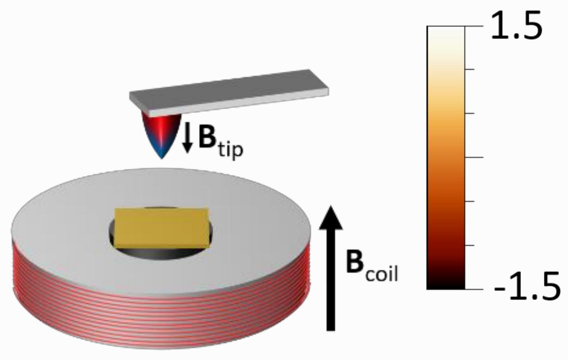

Applied field antiparallel to tip magnetization

Bubbles are nucleated applying a small perpendicular field to the multilayer, or equally, applying a parallel field with a small perpendicular component.

MFM images in remanence state

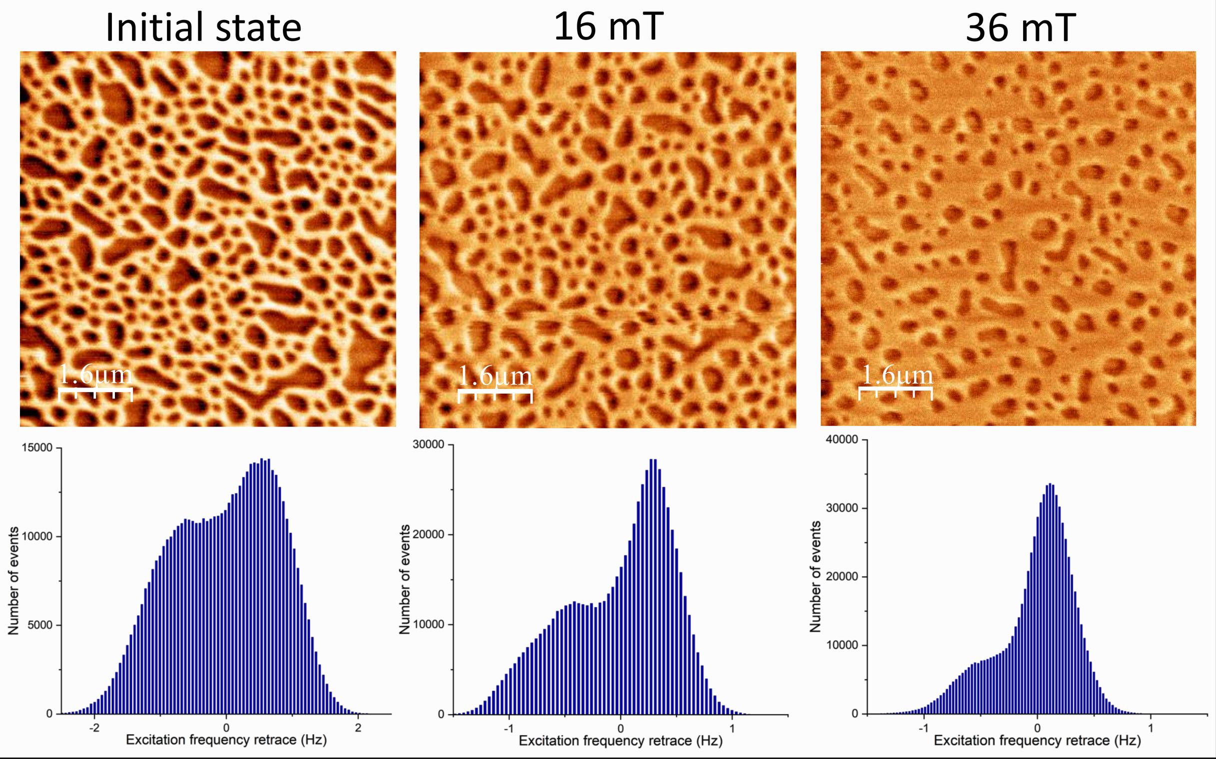

Size effects in nanostructures

MFM images taken in remanence after an out of plane demagnetization

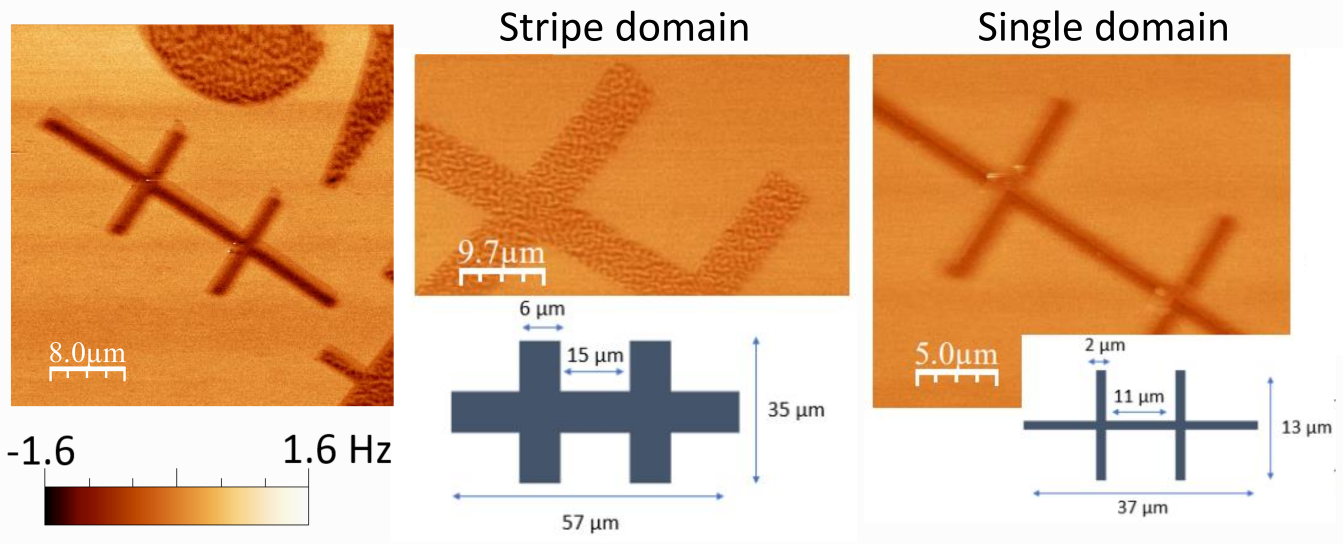

There is a dependence between the magnetic domains configuration and the size of nanostructures. There is a critical size for which a single domain configuration is more stable in sizes lower than this value, instead of a multiple domain configuration (stripe domains).

Bubble domains in nanostructures

Optical image

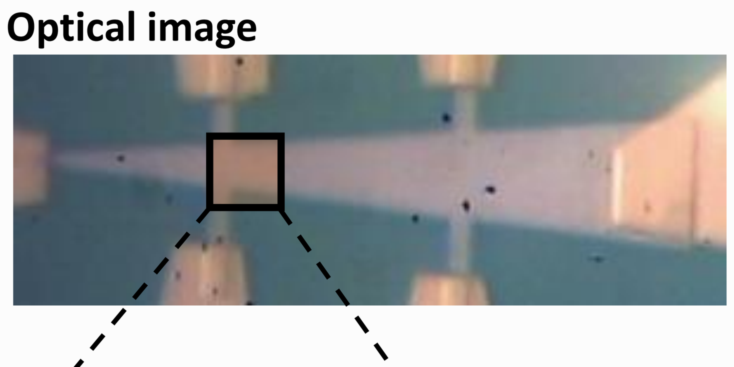

Applying a magnetic field in the opposite direction of the magnetization of the bubbles, the density of bubbles decreases. The remaining bubbles do not change their size nor their shape, i.e., their properties may be unchanged.

Applied field parallel to tip magnetization

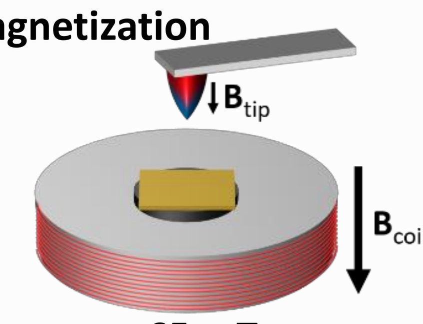

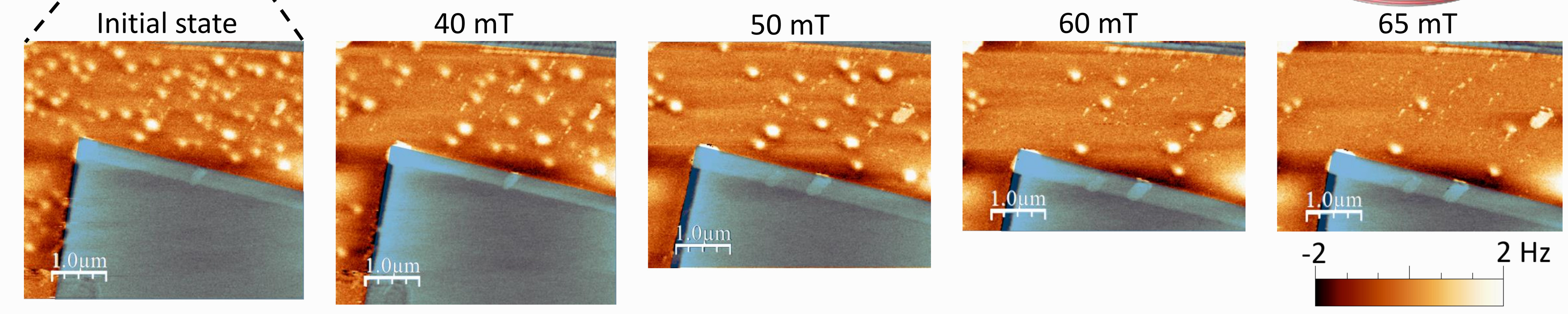

Bubbles nucleation by local magnetic field

Optical image

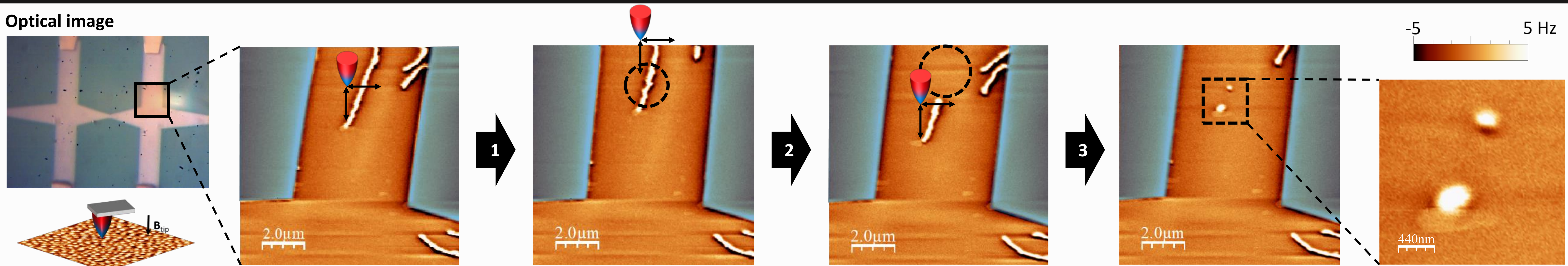

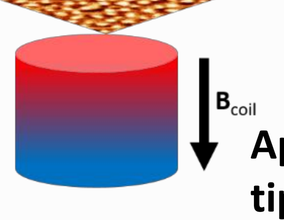

Applied field parallel to tip magnetization

Combining the VF-MFM and the field applied by the tip (tuning tip-sample distance), the magnetization of the sample is modified locally:

1. Without applying any external field and making several scans on the stripe, its shape is slightly distorted.
2. Applying 20 mT with the VF-MFM and with several scans, the upper part of the stripe is annihilated.
3. Without any external field and making several scans on the remaining part of the stripe, two magnetics bubbles are nucleated.

Summary

- Stripe and bubble domains can be nucleated in the CoPt multilayer (stable at room temperature and zero field).
- VF-MFM allows the tuning of the stripes and bubble sizes and densities once they are created.
- Combination of VF-MFM with the tip allows local changes in the magnetization and creation of bubbles.

References

[1] A. Kirilyuk et al., *J. Magn. Magn. Mater.*, **171**, 45-63 (1997)
[2] I. Dzyaloshinskii, *J. Phys. Chem. Solids*, **4**(4), 241-255 (1958)
[3] T. Moriya, *Phys. Rev. Lett.*, **4**(5), 228-230 (1960)
[4] J. Sampaio et al., *Nat. Nanotechnol.*, **8**, 839-844 (2013)
[5] M. Jaafar et al., *Ultramicroscopy*, **109**(6), 693-699 (2009)
[6] S. Zhang et al., *Appl. Phys. Lett.*, **112**, 132405 (2018)

Superferromagnetic Behaviour on Ordered Superlattices of Uniaxial Nanoparticles: A Micromagnetic Approach

Rafael Delgado-Garcia[1], Gabriel Rodriguez-Rodriguez[1], Jose M. Colino[1]
[1] INAMOL - UCLM, Av. Carlos III, s/n, 45071 Toledo (Toledo) Spain,
e-mail: gabriel.rrodriguez@uclm.es

We have studied lattice anisotropy effects in nanostructured superlattice arrangements of Co(hcp) randomly oriented magnetic nanoparticles (MNPs) via micromagnetic simulations. Remanent state and hysteresis loops have been calculated for a variety of superlattices, including simple cubic (SC), body-centered cubic (BCC) and face-centered cubic (FCC) orderings with major testing of parameters such as lattice parameter and layer growth.

Results show modulated coercivity and remanence from Stoner-Wohlfarth behaviour (valid for non-interacting uniaxial nanoparticles), evidencing the contribution of multipolar interactions due to the high ordering of the MNPs in the superlattice structure. This magnetostatic contribution gives rise to a lattice anisotropy that orients the NP's magnetic moments into the plane and hence reduces the total magnetic energy of the system.

Superlattice orderings

Arrangements of randomly-oriented Co(hcp) MNPs with uniaxial anisotropy in Simple Cubic (SC), Body-Centered Cubic (BCC) and Face-Centered Cubic (FCC) 2D monolayer and growth-layered distributions [Figure 1] have been modelled with periodic boundary conditions on XY, extending supercells of 20x20xt (where t is thickness) MNPs to quasi-infinite thin-films. For 8nm Co(hcp) MNPs, Lattice Parameter ($a = b = c$) has ranged from 14 to 20 nm.

In such systems, we have calculated remanent state from saturation from X to Y axes (in-plane φ study) and from X to Z coordinates (out-of-plane θ study) [Figure 2]. Additionally, hysteresis loops in X direction have been simulated.

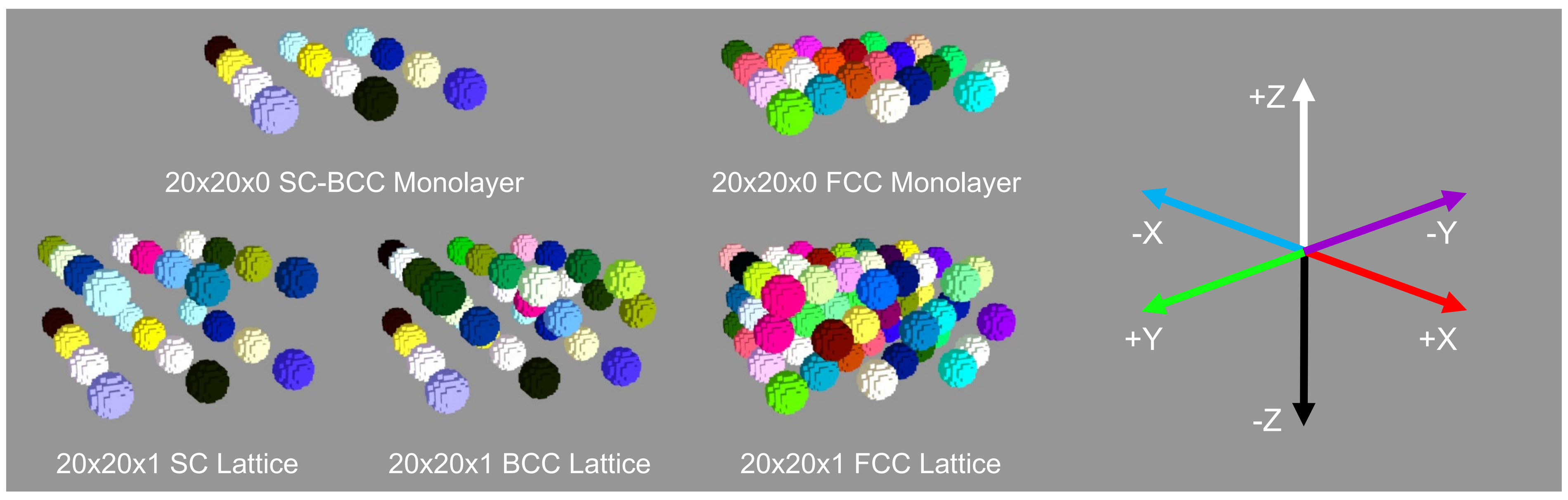

Figure 1. Schematic view of monolayers and lattices designed in simulations of MNP superlattices. Each colour represents a direction for uniaxial anisotropy according to HSL code.

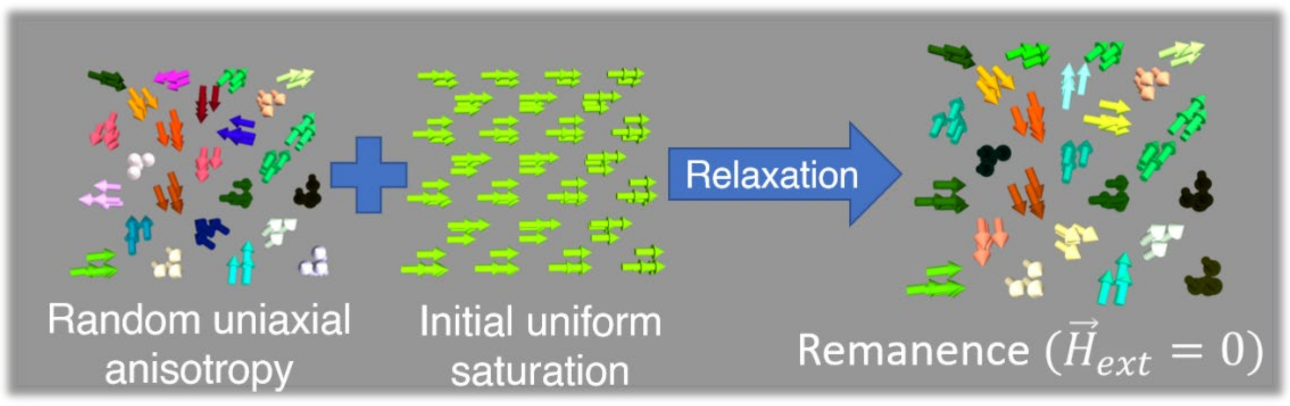

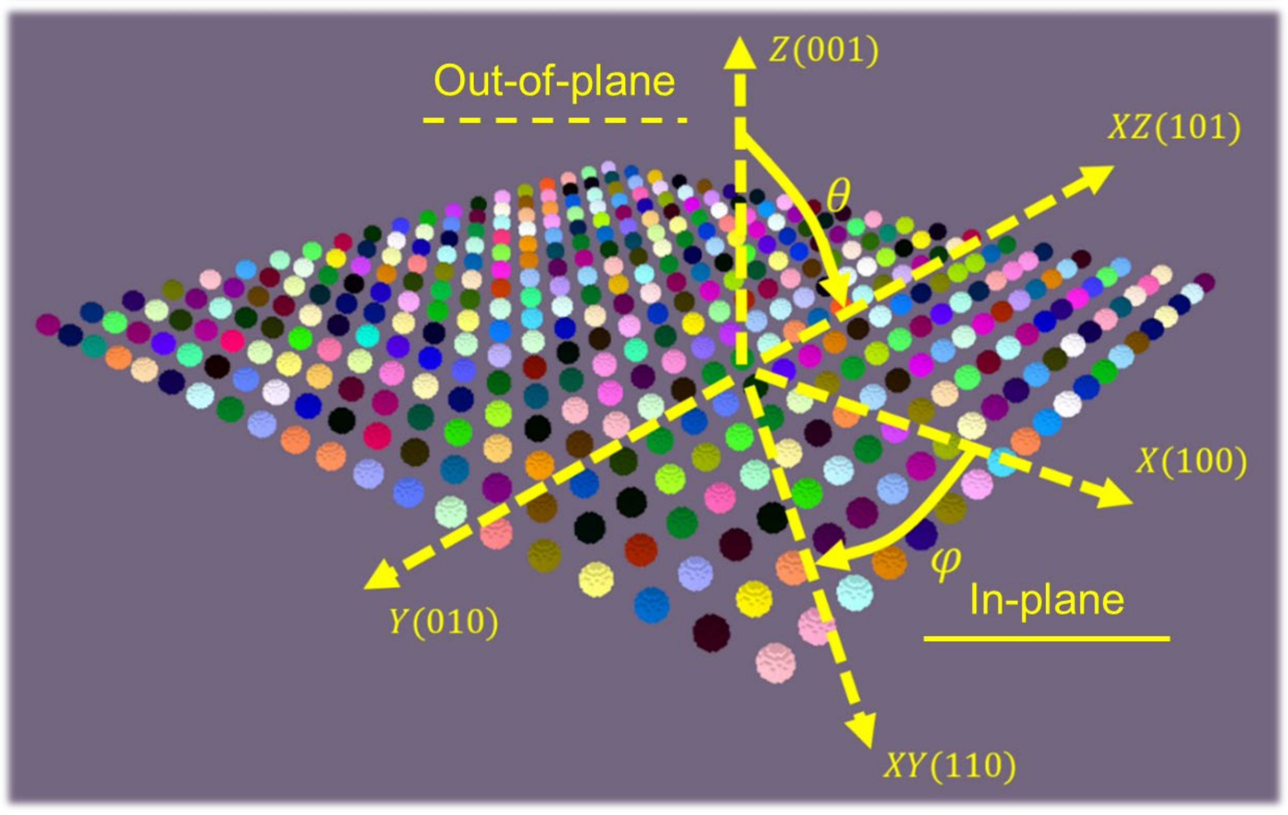

Figure 2. Scheme of angular scans of remanent state calculations in superlattice orderings of MNPs.

Multipolar effects on magnetic properties

Hysteresis loop of FCC Co(hcp) superlattices (1 super cell thickness) in (100) direction show a decrease of 22.5% in coercivity for a lattice parameter of 14 nm [Figure 3], as compared to predicted Stoner-Wohlfarth (SW) behaviour of non-interacting uniaxial systems.

Remanence polar plots for superlattices of different thicknesses [Figure 4] show a surge of multipolar effects manifested in lowering of M_r in out-of-plane component as width of the superlattice increases [Figure 5]. This way, it has been found in FCC superlattices a lowering of the out-of-plane remanence ($\theta = 0°$) of 29, 33 and 35% for thicknesses of 0, 1 and 5 supercells as compared to the expected value of $M_r/M_s = 0.5$ from SW.

Control of the lattice parameter from 14 to 20 nm has yield a much lower remanence reduction in the out of plane distribution [Figure 6], as multipolar effects decrease with the distance.

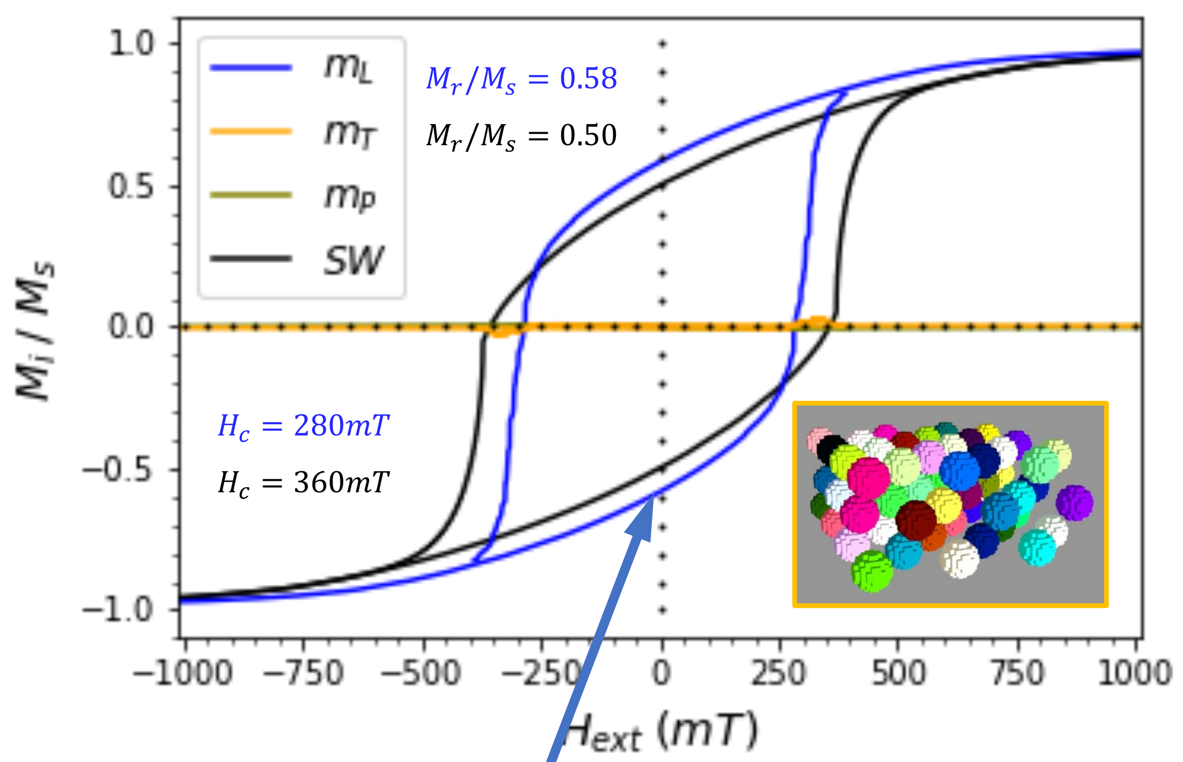

Figure 3. Hysteresis loop of t=1 FCC Co(hcp) superlattice with lattice parameter of 14 nm in 100 direction compared with SW

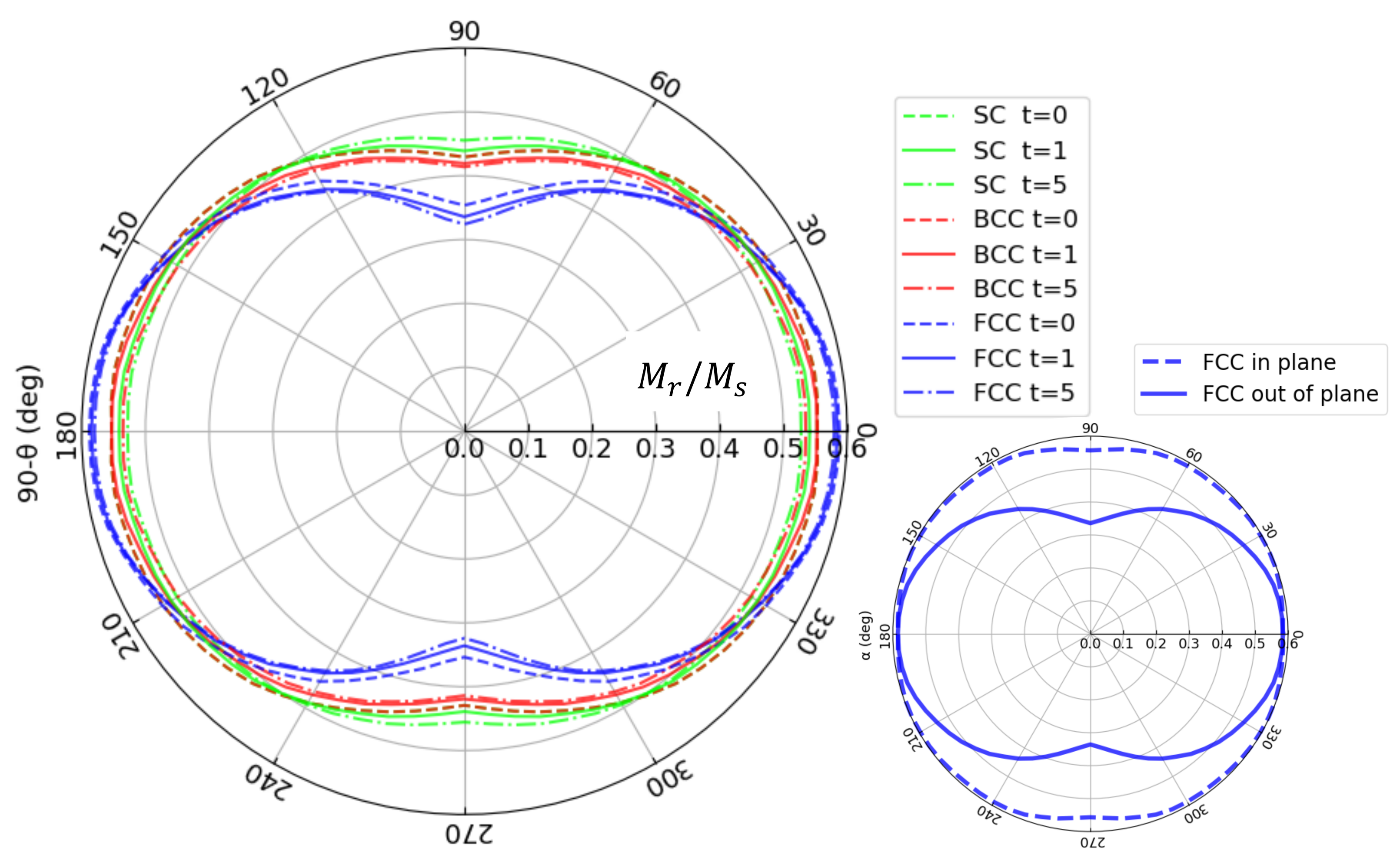

Figure 4. Remanence polar plot in out-of-plane distributions of SC, BCC and FCC Co(hcp) superlattices of 14nm lattice parameter and 0, 1 and 5 supercells thickness. In-plane and out-of-plane distributions for FCC t=1 are shown as insert.

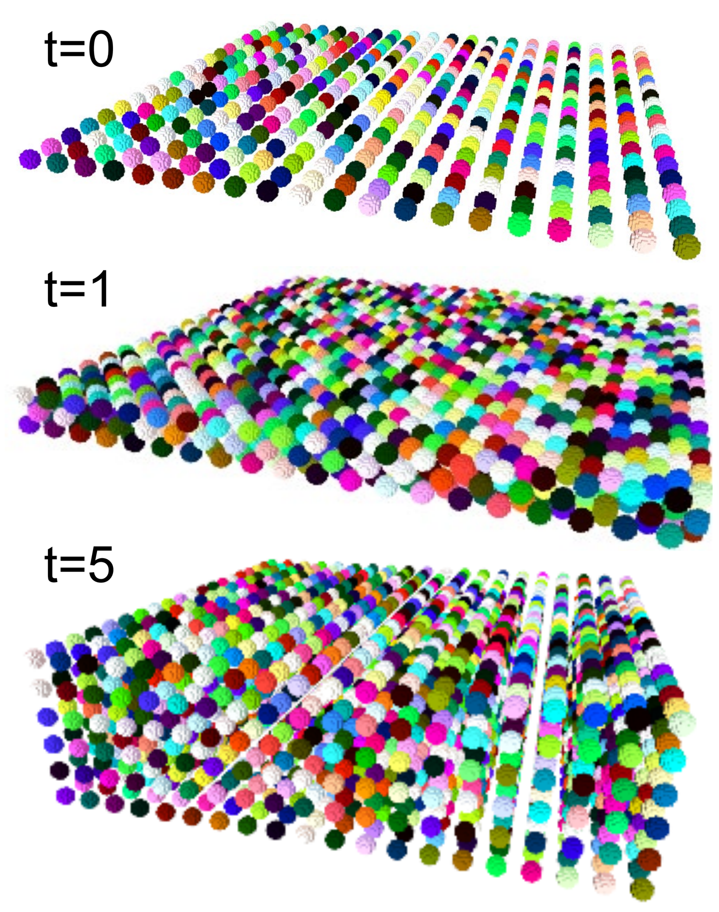

Figure 5. From top to bottom: SC superlattices of 0, 1 and 5 supercells thicknesses.

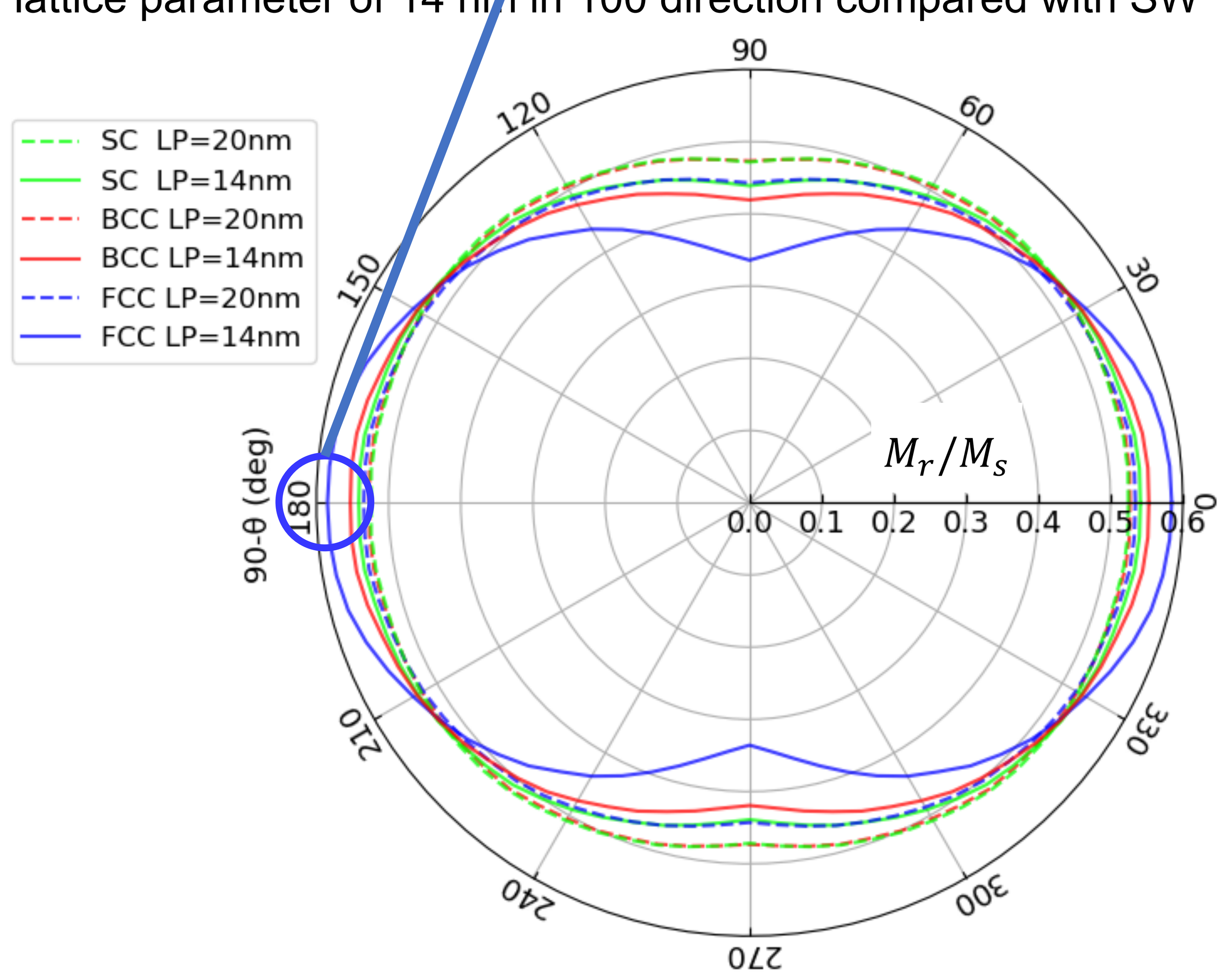

Figure 6. Remanence polar plot in out-of-plane distributions of Co(hcp) t=1 SC, BCC and FCC superlattices with lattice parameters of 20 and 14 nm.

Conclusions

- FCC superlattice arrangement of Co MNPs (LP=14 nm, t=1) at (100) direction presents lowered coercivity (~ 22.5% less) as compared to Stoner-Wohlfarth prediction for uniaxial, non-interacting and randomly-oriented ensembles.
- Increasing thickness of superlattices (LP=14nm) enhances deviation of remanence from quasi-isotropic in favour of in-plane superlattice-induced anisotropy.
- FCC shows major multipolar induced lattice anisotropy compared to SC and BCC orderings, achieving reduced remanences in out-of-plane direction ($\theta = 0°$) of up to 35% less than Stoner-Wohlfarth prediction.
- Shrinking the lattice parameter (20→14nm) increases multipolar effects in the network, lowering remanence in out-of-plane distributions.

Acknowledgements

This work has been possible thanks to the MICINN, as a part of the Project MAT2015-65295-R: "Nanocomposites magnéticos para aplicaciones en energía y sensores". Rafael Delgado-Garcia thanks UCLM and Banco Santander for the scholarship for research initiation during his Master studies.

GOBIERNO DE ESPAÑA
MINISTERIO DE ECONOMÍA Y COMPETITIVIDAD
Santander

References

E. H. Sánchez et al., Chemistry of Materials, Vol. 32, p.969-981 (2020)
D. Kim et al., Journal of Magnetism and Magnetic Materials, Vol. 320(19), p.2390-2396 (2008)
Q. Li et al., Scientific Reports, Vol. 7, p.9894 (2017)
D. Peddis et al., Chemistry of Materials, Vol. 25(10), p.2005-2013 (2013)
A. Vansteenkiste et al., AIP Advances, Vol. 4, p.107133 (2014)
J. A. Osborn, Physical Reviews, Vol. 67, p.351 (1945)
D. Farrell et al., Journal of Physical Chemistry B, Vol. 109(28), p.13409-13419 (2005)
C. Tannous and J. Gleraltowski, European Journal of Physics, Vol. 29, p. 475-487 (2008)

Universidad del País Vasco / Euskal Herriko Unibertsitatea
ZIENTZIA ETA TEKNOLOGIA FAKULTATEA / FACULTAD DE CIENCIA Y TECNOLOGÍA
BCMATERIALS BASQUE CENTER FOR MATERIALS, APPLICATIONS & NANOSTRUCTURES
Contact: *virginia.vadillo@bcmaterials.net*

Magnetic Nanoparticles: Synthesis, Characterization and Applications

Virginia Vadillo [1], Jon Gutiérrez[1,2] Maite Insausti [1,2], Roberto Fernández[1], Joseba S. Garitaonandia[1,2], Izaskun Gil de Muro[1,2], Mounir Bouali[3], Joanes Berasategui[3], Ainara Gómez[3] and Jose Manuel Barandiaran[1,2]

[1]BC Materials (Basque Center for Materials, Applications and Nanostructures), Bld. Martina Casiano 3rd. Floor, Barrio Sarriena s/n, 48940, Leioa, Spain
[2]Faculty of Science and Technology, University of Basque Country, UPV/EHU, Barrio Sarriena s/n, 48940, Leioa, Spain
[3]Fluid Mechanics, University of Mondragon, Loramendi 4, 23 – 20500, Arrasate – Mondragón, Spain

INTRODUCTION

Interest in magnetic nanoparticles has grown in the last years because their versatility to be used in several applications including industrial[1], environmental and biomedical applications[2]. This work is focused on the synthesis of Fe_3O_4 to be employed as magnetic adsorbents combined with metal organic frameworks (MOFs) to remove contaminants from water and the synthesis of Fe_xCo_{1-x}[3] to be used as magnetic fillers in magnetorheological fluids applications.

NANOPARTICLES

Fe_3O_4 NPs COPRECIPITATION

Iron (III) chloride hexahydrated water solution + Iron (II) chloride water solution + Ammonia water solution → sodium citrate → Fe_3O_4 CPS1; → Fe_3O_4 CP1

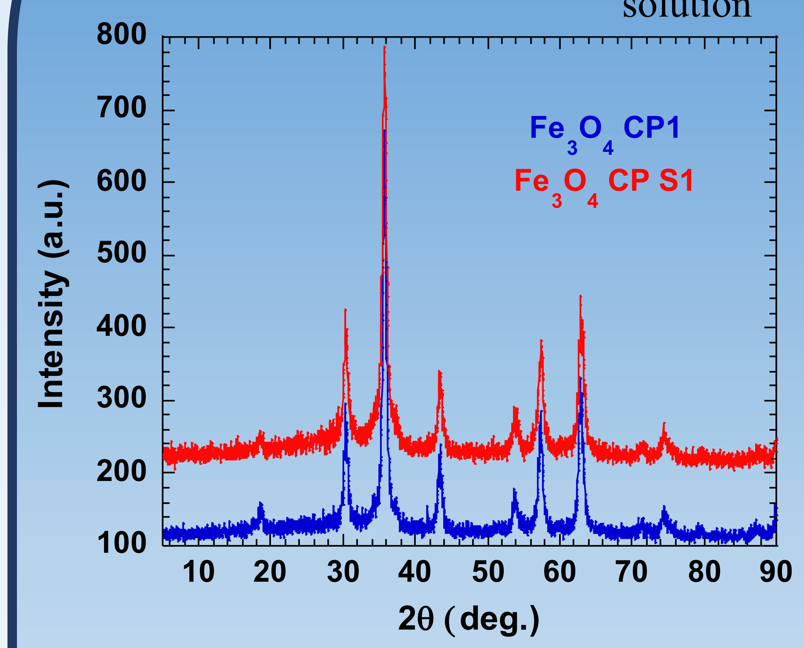

Fe_3O_4 CP1

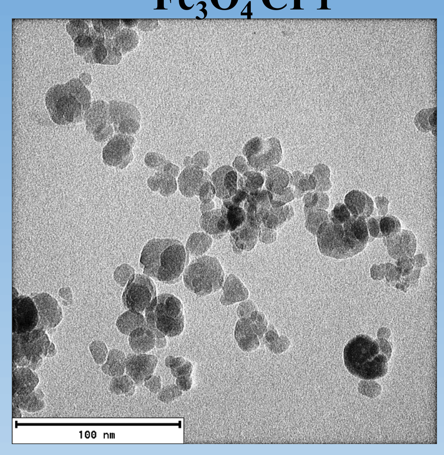

Fe_3O_4 CP S1

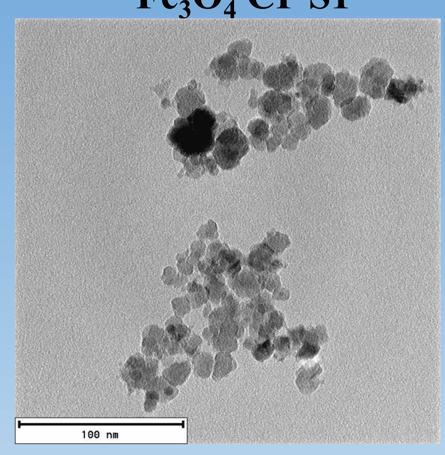

The typical peaks of magnetite are observed in both diffraction patterns.

Sample	TEM Size (nm)
Fe_3O_4 CP1	5-25 (13±4)
Fe_3O_4 CP S1	5-20 (13±3)

Sample	ZP (mV)
Fe_3O_4 CP1	4.0 ± 3.5
Fe_3O_4 CP S1	-35.7 ± 6.4

The stability of NPs was studied trough the zeta potential measured by Dinamic Light Scattering.

The use of surfactant allows to achieve a stable dispersion of these nanoparticles without modify the size of the NPs.
The magnetic properties shows a M_s about 77 Am²/kg for magnetite CPS1 and 83 Am²/kg for CP1. In both cases, a low H_C is achieved.

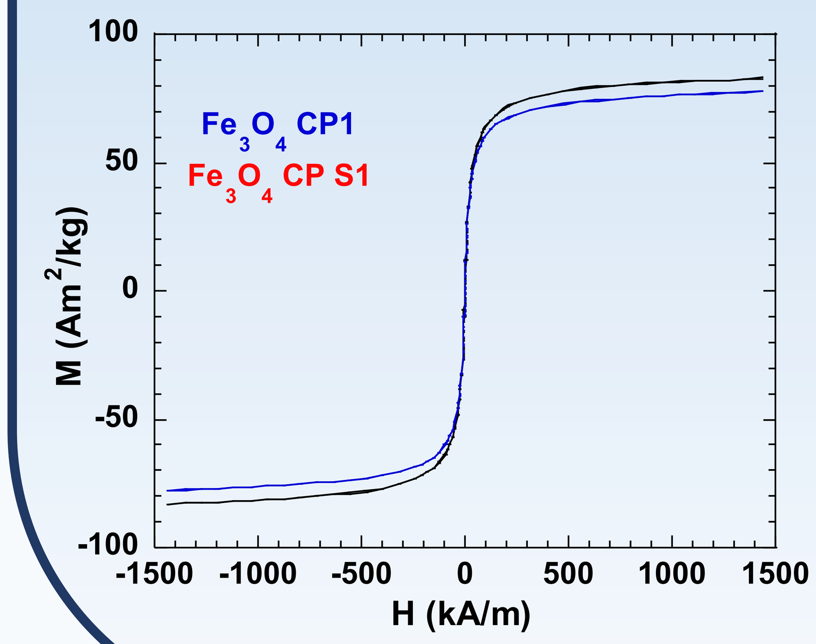

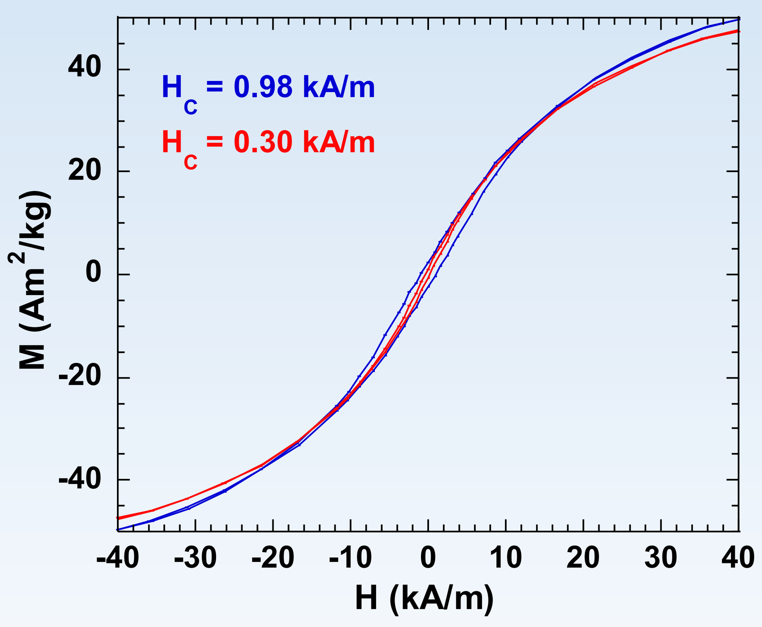

Fe_xCo_{1-x} NPs CHEMICAL REDUCTION

$$Fe^{3+} + Al + 6F^- \rightarrow Fe + AlF_6^{3-} \qquad E^0_{Fe^{3+}/Fe} = -0.037V$$
$$3Co^{2+} + 2Al + 12F^- \rightarrow 3Co + 2AlF_6^{3-} \qquad E^0_{Co^{2+}/Co} = -0.28V$$
$$E^0_{AlF_6^{3-}/Al} = -2.069V$$

By employing this method nanoparticles of Fe, Co and FeCo with different Fe/Co ratio have been synthesized .

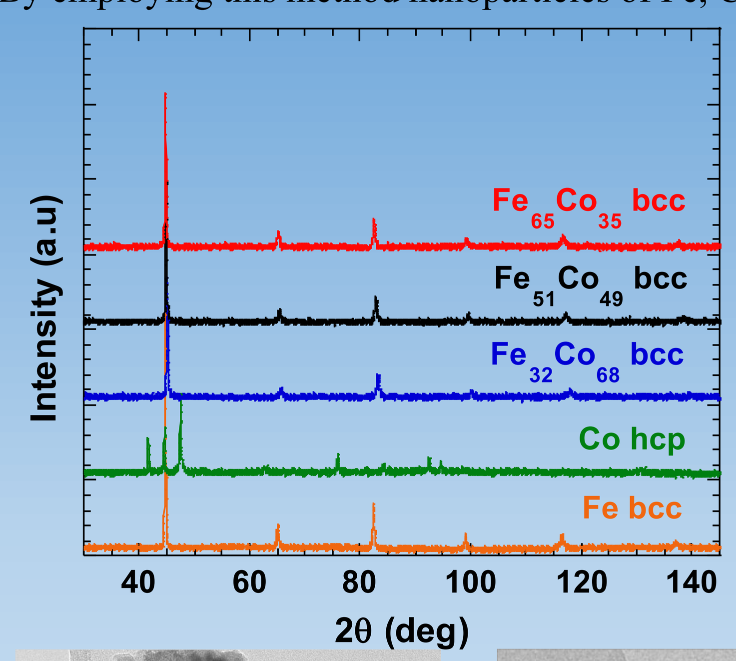

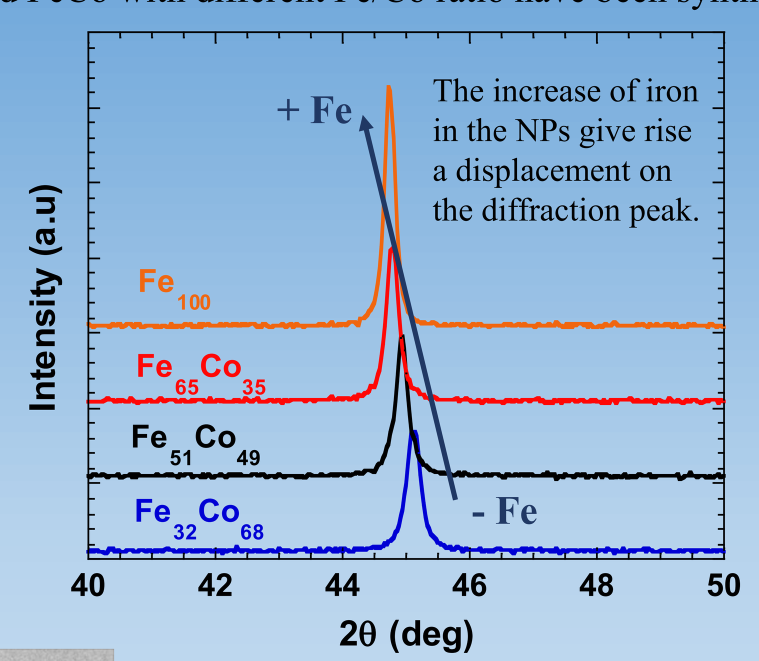

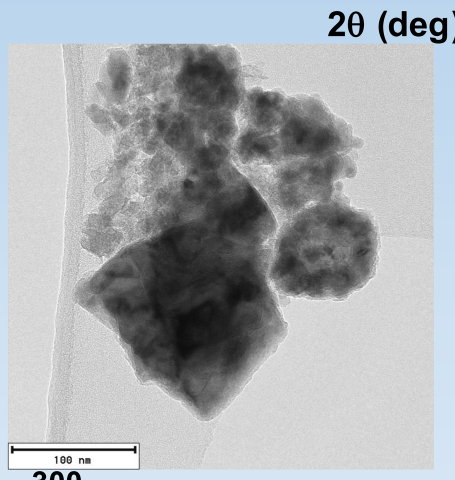

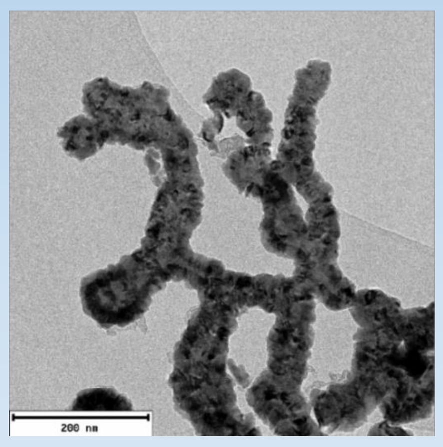

As example, these TEM images show the size and morphology of $Fe_{51}Co_{49}$. The most of the single NPs have a size ranging between 30-50 nm, together with a few plate sized NPs as big as 100 nm. Due to high magnetization value of the nanoparticles, this TEM images confirms the tendency to the aggregate state in the form of a dendritic structure as big as 200-500 nm

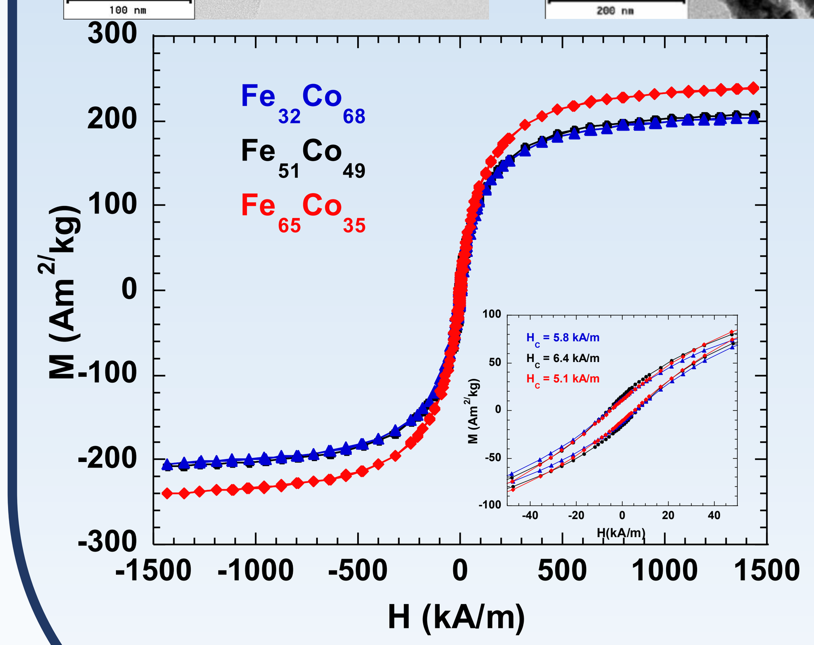

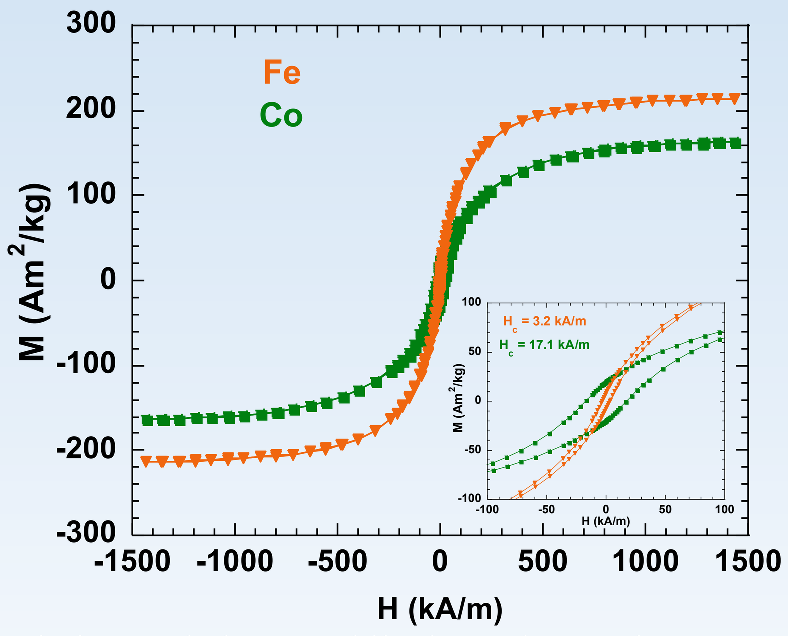

The highest quantity of iron increases the M_s in iron-cobalt NPs while the H_c keeps almost constant. While for Fe and Co, as expected, the M_s is higher for Fe NPs and The H_c is lower.

APPLICATIONS

MOF@MNPs

Functionalized Fe_3O_4 NPs + Iron (III) chloride ethanol solution + Trimesic acid ethanol solution → 2h at 70º, 5 cycles → Fe_3O_4 CPS1@MIL100

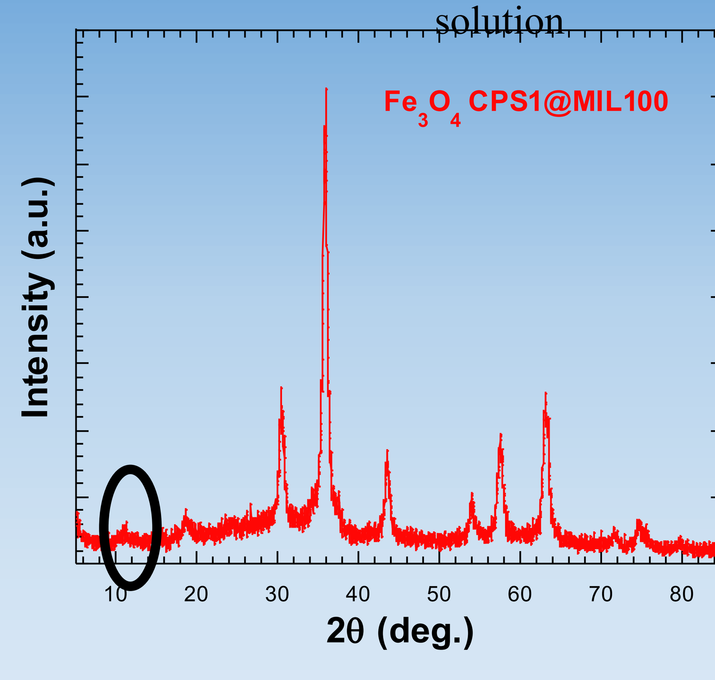

A new peak in the diffraction pattern appears in the Fe_3O_4CPS1@MIL100 composite, indicating the MOF growth in NPs surface. This fact is also observed in the TEM image of the Fe_3O_4CPS1@MIL100 material.

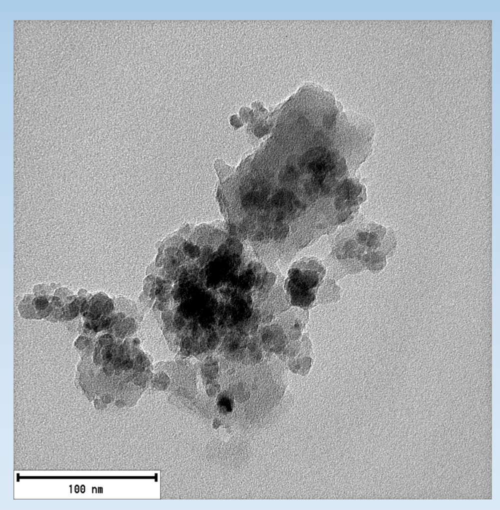

Environmental Applications

This material will be employed to remove contaminants from water such as arsenic. The interest to employ magnetic nanoparticles with the metal organic frameworks is the easy recovery of material after the adsorption process trough a permanent magnet.

MAGNETORHEOLOGICAL FLUIDS

Carrier fluid: Mineral oil
Nanofillers: $Fe_{51}Co_{49}$NPs
Additive: Aerosil
Surfactant: Oleic acid

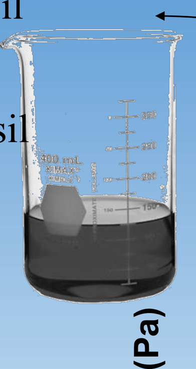

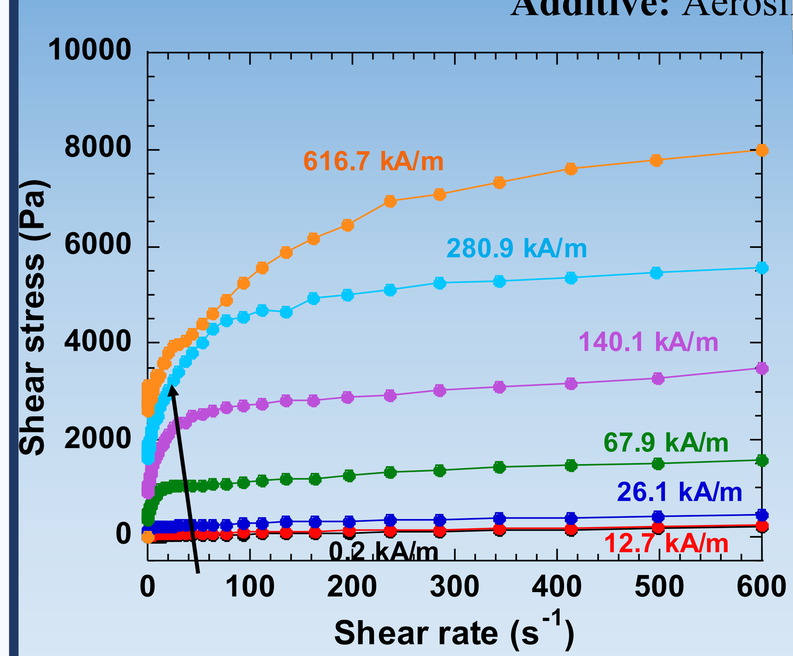

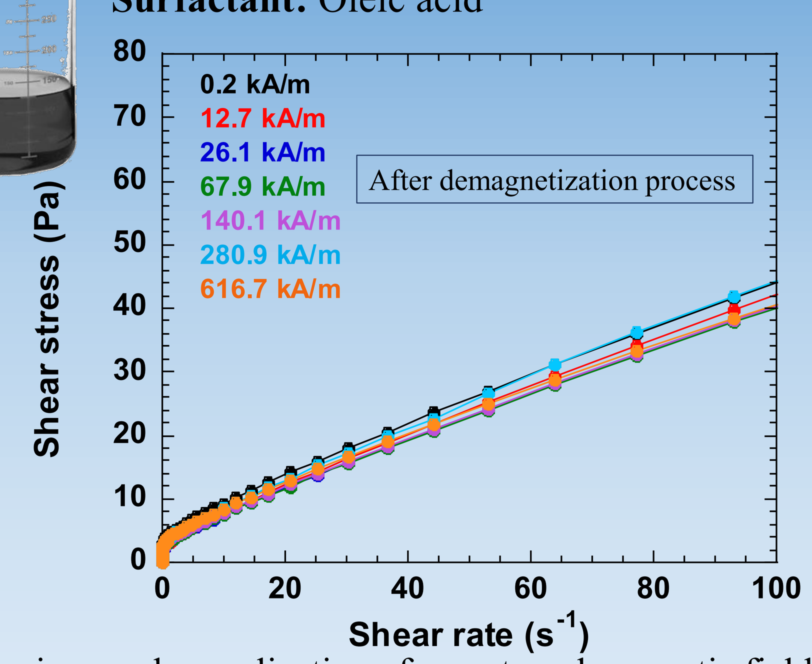

- The synthesized fluids showed a non-Newtonian behaviour under application of an external magnetic field.
- The shear stress increases with the magnetic field intensity showing a strong magnetorheological response.
- These rheological curves were characterized by the corresponding yield stress value. The magnitude of this yield stress increases as the magnetic field intensity does (see black arrow). The work range of the fluid can be determined by the yield stress. So, greater difference between yield stress at 0.2kA/m and 617kA/m higher work range.
- After demagnetization process the FeCo magnetorheological fluid goes back to its initial state keeping almost constant its yield stress value.

CONCLUSIONS

- The specific application of NPs depends on the kind of NPs and their chemical, structural and magnetic properties.
- By employing coprecipitation method, magnetite nanoparticles are achieved. The use of surfactant improve the dispersion stability. These stable NPs have a mean size about 13±3 nm and a M_s 77 Am²/kg.
- The growth of MOF MIL100 is NPs surface is achieved after 5 cycles. The value of M_s is enough to recover the NPs after adsorption process by employing a permanent magnet.
- By employing chemical reduction method, Fe_xCo_{1-x} NPs are obtained with good crystallinity and good magnetic properties.
- The $Fe_{51}Co_{49}$ NPs were employed as magnetic fillers for magnetorheological fluid synthesis. This synthesized fluid shows a strong magnetorheological response and a good reversibility after demagnetization process.

REFERENCES

[1] S. Genc and B. Derin, "Synthesis and rheology of ferrofluids: a review," *Curr. Opin. Chem. Eng.*, vol. 3, pp. 118–124, 2014.
[2] L. Mohammed, H. G. Gomaa, D. Ragab, and J. Zhu, "Magnetic nanoparticles for environmental and biomedical applications : A review," Particuology, pp. 1–14, 2016.
[3] Z. Klencsár, P. Németh, Z. Sándor, T. Horváth, I.E. Sajo, S. Mészáros, J. Mantilla, J.A.H. Coaquira, V.K. Garg, E. Kuzmann and Gy. Tolnai, J. Alloys Compd., 674, pp. 153–161 (2016).

ACKNOWLEDGEMENTS

This work was financially supported by the Basque Government through PI-2017-1-0043 (PIBA Program), ACTIMAT KK-2018/00099 (Elkartek Program), and IT 12126-19 projects. Technical and human support provided by SGIker (UPV/EHU) is also gratefully acknowledged.

Controlling Interfacial Phenomena in Hybrid V_2O_3/Co Bilayers

J.M. Díez[1,2], J.L.F. Cuñado[2], P. Perna[1], P.N. Lapa[3], R. Miranda[1,2], Ivan K. Schuller[3] and Julio Camarero[1,2]

[1] IMDEA Nanoscience, C/ Faraday, 9 Ciudad Universitaria de Cantoblanco 28049 Madrid, Spain
[2] Departamento de Física de la Materia Condensada, IFIMAC, & Instituto Nicolás Cabrera, Universidad Autónoma de Madrid (UAM), 28049 Madrid, Spain
[3] Department of Physics and Center of Advanced Nanoscience, University of California, San Diego (UCSD), La Jolla, California 92093, USA

INTRODUCTION

Interfacial exchange coupling and proximity effects in antiferromagnetic/ferromagnetic (AFM/FM) bilayers are the potential keys that control the exchange bias phenomena exploited in all spintronic devices. In both cases, the spin fluctuations in the AFM layer during the temperature-driven magnetic phase transition at Néel temperature (T_N) are commonly used to understand the magnitude of the exchange bias field (H_e), the inset of H_e , referred as Blocking temperature ($T_B <= T_N$), as well as the enhancement of the coercive field (H_C).

Here we show that the magnetization reversal of the FM layer, in particular, its magnetic domain structure during reversal, not only has a strong influence on the mentioned effects but also control them. Temperature dependent measurements performed in a V2O3/Co bilayer after different field cooling (FC) procedures reveal that these effects depend strongly on the FC angle and are associated with a different domain structure of the FM layer that has a well-defined uniaxial magnetic anisotropy.

Remarkably, a wide temperature window for T_B and up to a factor of two in H_e are found. All experimental observations cane be explained within the Random-Field Model for the interfacial exchange coupling in AFM/FM bilayers with a fixed ADM domain structure in contact with a variable (angle dependent) FM domain structure.

RT Magnetization

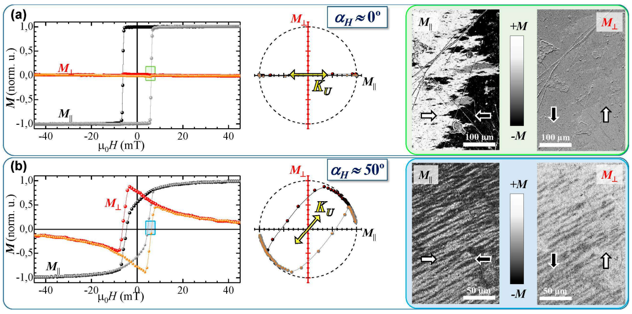

Figure 2. Room temperatura magnetization reversal of the V_2O_3/Co sample at the indicated field angles. **Left panel** Standard representation of the vectorial-resolved MOKE measurements. **Central panel** Corresponding vectorial representation. **Right panel** v-MOKE microscopy images acquired during the revsersal

At 300 K the V_2O_3 is paramagnetic and the data reflect the intrinsic uniaxial magnetic anisotropy of the Co layer.

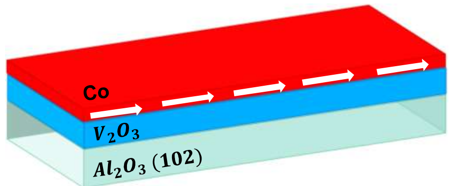

Figure 1. Sketch of the V_2O_3(100nm)/Co(15nm) bilayer.

FM and AFM domain textures across MIT

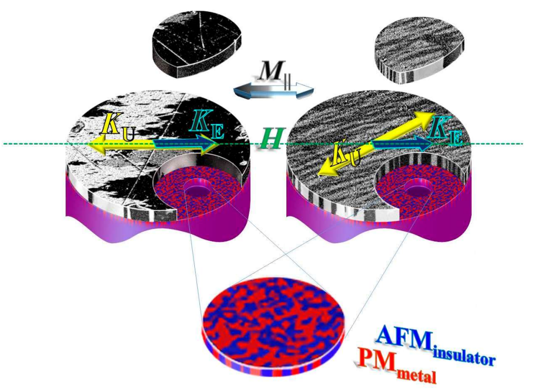

Figure 3. Scheme of the FM and AFM domain textures. The relevant directions are indicated: uniaxial anisotropy of the FM layer (K_U solid yellow line);interfacial unidirectional anisotropy (K_E, solid blue line); external in-plane magnetic field (H, dashed green line). The bottom image is a high-resolution co-localized near-field imagen showing the coexisting paramagnetic metallic (red) and antiferromagnetic insulating (blue) phases of the V_2O_3 layer during its phase transition

Temperature dependance

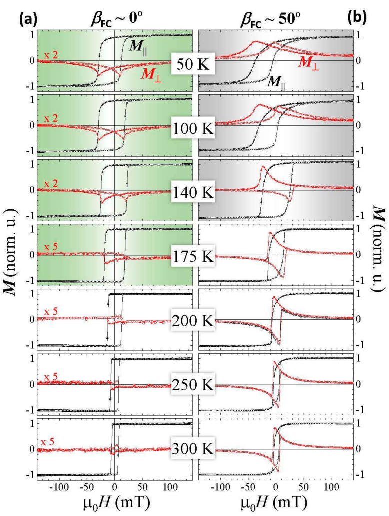

Figure 4. Temperature dependent v-MOKE hysteresis loops recorded after two selected positive-FC procedures on the same sample. (a) collinear ($\beta_{FC} \approx 0°$) anisotropy configuration; (b) non-collinear ($\beta_{FC} \approx 50°$) configuration.

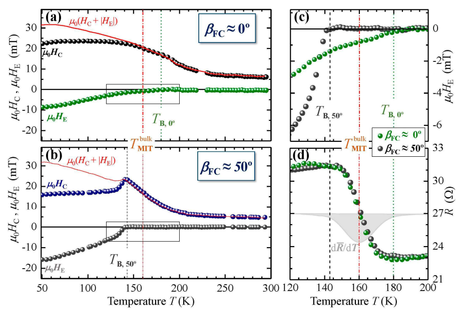

Figure 5. Temperature evolution of relevant magnetic and transport parameters after the two FC procedures: collinear (a) and non-collinear (b) anisotropy configuration. (c) Zoom of (a) and (b around the MIT transition. (d) Resistance (R) values for the two configurations.

Temperature Evolution

Random Field Model

$\sigma_{FM}/_{AFM} \sim 1/\sqrt{N}$

N being the number of AFM grains within one FM domain

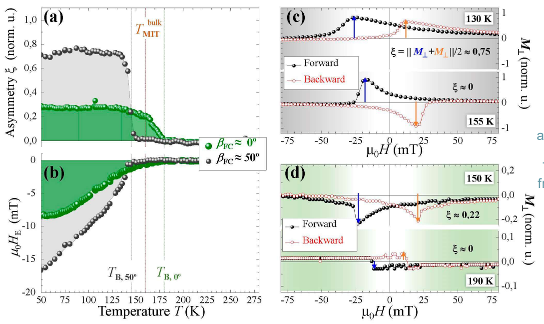

Figure 6. Comparison of the evolution of asymmetry (a) and Exchange bias (b) during the warming for the studied configuration. The asymmetry ξ value have been derived from the maximum values of the descending (forward) and ascending (backward) field branch of the $M_\perp$(H) loops-

Conclusions

- The magnetic domain texture of the FM layer during reversal has a strong influence in the interfacial exchange bias.
- Transport properties for the two anisotropy configurations do not differ.
- Our results provide a general microscopic view that can be extended to any AFM/FM system.
- The Key role of the FM texture during reversal could be used to design interfacial effects at will.

References

1. Rev. Mod. Phys. **70**, 1039-1263 (1998).
2. Phys.Rev. Lett. **122**, 057601 (2019).
3. Appl. Phys. Lett., **102**(12), 122404 (2013